

Fall 2011

# Plasma-activated fusion bonding for vacuum encapsulation of microdevices

Joel Soman  
*Louisiana Tech University*

Follow this and additional works at: <https://digitalcommons.latech.edu/dissertations>



Part of the [Engineering Commons](#)

---

## Recommended Citation

Soman, Joel, "" (2011). *Dissertation*. 365.  
<https://digitalcommons.latech.edu/dissertations/365>

This Dissertation is brought to you for free and open access by the Graduate School at Louisiana Tech Digital Commons. It has been accepted for inclusion in Doctoral Dissertations by an authorized administrator of Louisiana Tech Digital Commons. For more information, please contact [digitalcommons@latech.edu](mailto:digitalcommons@latech.edu).

**PLASMA-ACTIVATED FUSION BONDING FOR VACUUM  
ENCAPSULATION OF MICRODEVICES**

by

Joel Soman, M.S., B.E.

A Dissertation Presented in Partial Fulfillment  
of the Requirements For the Degree  
Doctor of Philosophy

COLLEGE OF ENGINEERING AND SCIENCE  
LOUISIANA TECH UNIVERSITY

November 2011

UMI Number: 3492486

All rights reserved

INFORMATION TO ALL USERS

The quality of this reproduction is dependent upon the quality of the copy submitted.

In the unlikely event that the author did not send a complete manuscript and there are missing pages, these will be noted. Also, if material had to be removed, a note will indicate the deletion.



UMI 3492486

Copyright 2012 by ProQuest LLC.

All rights reserved. This edition of the work is protected against unauthorized copying under Title 17, United States Code.



ProQuest LLC  
789 East Eisenhower Parkway  
P.O. Box 1346  
Ann Arbor, MI 48106-1346

LOUISIANA TECH UNIVERSITY

THE GRADUATE SCHOOL

09/15/2011

Date

We hereby recommend that the dissertation prepared under our supervision by JOEL SOMAN

entitled Plasma-Activated Fusion Bonding For Vacuum Encapsulation Of Microdevices

be accepted in partial fulfillment of the requirements for the Degree of Doctor of Philosophy


Supervisor of Dissertation Research

Head of Department

Engineering

Department

Recommendation concurred in:



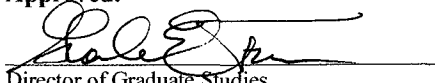
Sandra Zivanovic



Advisory Committee



Approved:

  
Director of Graduate Studies

Approved:

  
Dean of the Graduate School

  
Dean of the College

## ABSTRACT

A fabrication process for vacuum-encapsulating PZT microcantilevers was designed in this dissertation. Initially, a low temperature wafer-bonding recipe was optimized with the help of plasma-activation. Conventional direct fusion bonding temperature was reduced from 400 °C to 85 °C, and final thermal annealing temperature and time of 1000 °C for 4 hours (hr) were significantly reduced to 300 °C and 1 hr respectively. Tensile tests conducted on dies diced from the bonded wafer stack revealed bond strengths of 22.15 MPa, which was close to the bulk fracture strength of 24 MPa for silicon. Near infrared images of the wafer stack showed no debonded regions at the interface. Surface and interface chemistry of oxygen plasma-activated wafers before, during, and after bonding were investigated. Significance of wet chemical activation technique, like RCA (Radio Corporation of America) cleaning, was studied. The time interval between plasma-activation and fusion bonding was varied, and its effect on the bond quality and bond strength was investigated. Decrease in the bond-quality and strength was observed with an increase in storage time. However, an unexpected increase in the bond quality was observed after 48 hr, and was attributed to the increase in the interfacial oxide layer. Further investigations revealed that the interfacial oxide layer was capable of absorbing gas molecules released as a byproduct of ongoing reactions at the interface of the two wafers. Gettering capability of the interfacial oxide layer was

confirmed through the bonding of plasma-activated and 48 hr stored silicon (Si) and silicon dioxide (SiO<sub>2</sub>) wafers. Infrared images showed a good bond for the wafer stack.

Since designing a fabrication process flow for vacuum-encapsulation of microdevices was the primary objective, lead zirconate titanate microcantilevers were fabricated onto a silicon substrate. The microdevices were actuated in ambient air pressure as well as in a vacuum environment. Broadening of the resonance curve was observed with an increase in the magnitude of ambient pressure, and is a result of increased air-damping. Experimental results obtained were compared to theoretical results from finite element modeling analyses.

Vacuum cavities were fabricated between two Si wafers. Optical lid-deflection method of measuring internal cavity pressure was explored and employed with the help of high aspect ratio pressure diaphragms on a capping wafer. An investigation of seal integrity of the vacuum package revealed real/virtual leaks. The gettering capability of the SiO<sub>2</sub> layer was employed in order to preserve the vacuum-level in the cavities. Two types of gettering patterns were investigated. It was concluded that a SiO<sub>2</sub> getter layer at the interface increased the seal-integrity of the vacuum packages, while getter rings still showed signs of real leaks. In addition, it was observed that the internal vacuum-level was higher for cavities with getter rings as compared to cavities without getters. It was concluded that getter rings were capable of preventing virtual leaks but not real leaks. A thick interfacial getter layer, however, prevented both the real and virtual leaks.

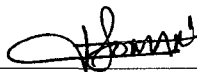
Finally, a vacuum-packaging fabrication method to encapsulate lead zirconate titanate microcantilevers was proposed. In addition, more accurate methods of measuring package vacuum pressure magnitudes were proposed.

## APPROVAL FOR SCHOLARLY DISSEMINATION

The author grants to the Prescott Memorial Library of Louisiana Tech University the right to reproduce, by appropriate methods, upon request, any or all portions of this Dissertation. It is understood that "proper request" consists of the agreement, on the part of the requesting party, that said reproduction is for his personal use and that subsequent reproduction will not occur without written approval of the author of this Dissertation. Further, any portions of the Dissertation used in books, papers, and other works must be appropriately referenced to this Dissertation.

Finally, the author of this Dissertation reserves the right to publish freely, in the literature, at any time, any or all portions of this Dissertation.

Author



Date

09/15/2011

## TABLE OF CONTENTS

ABSTRACT.....	iii
APPROVAL FOR SCHOLARLY DISSEMINATION .....	v
LIST OF TABLES.....	ix
LIST OF FIGURES .....	x
ACKNOWLEDGMENTS .....	xvi
CHAPTER 1 INTRODUCTION .....	1
1.1    Wafer Bonding.....	1
1.2    Micro Electro Mechanical Systems .....	2
1.2.1    Photolithography.....	3
1.2.2    Metal Deposition.....	3
1.2.3    Metal Wet/Dry Etching.....	3
1.2.4    Silicon Wet/Dry Etching.....	4
1.3    Project Overview .....	4
1.4    Research Motivation .....	5
1.5    References.....	6
CHAPTER 2 LITERATURE REVIEW .....	7
2.1    Direct Fusion-Bonding and Testing Methods.....	7
2.2    Investigation Techniques on Buried Oxide Layer .....	16
2.3    Vacuum Packaging and Testing Methods .....	22
2.4    Lead Zirconate Titanate .....	32
2.5    References.....	34

CHAPTER 3 ANALYTICAL AND THEORETICAL MODELING .....	39
3.1    Finite Element Modeling of Si Pressure Diaphragm .....	39
3.2    Optimization of PZT Composite Beam .....	46
3.3    Analytical Modeling of PZT Composite Beam .....	49
3.4    Theoretical Modeling of Composite Undamped PZT Beam .....	51
3.5    Frequency Analyses of Damped Composite PZT Beam .....	52
3.6    References.....	55
CHAPTER 4 EXPERIMENTAL PROCEDURES.....	56
4.1    Direct Fusion-Bonding of Si/Si .....	56
4.2    Plasma-Activated Wafer Bonding .....	58
4.3    Investigation on Interfacial Oxide Formation and Growth.....	59
4.4    Fabrication of Cavities and Pressure Diaphragms in Silicon .....	61
4.4.1    Fabrication of Cavities in Si Substrate.....	61
4.4.2    Fabrication of Pressure Diaphragms in Si Wafer .....	63
4.5    Experimental Procedure for Measuring Vacuum Pressure.....	67
4.6    PZT Thin-Film Deposition .....	69
4.7    Fabrication of PZT Microcantilevers.....	70
4.8    Experimental Setup and Results for Device Capacitance Measurements .....	76
4.9    Experimental Setup for Testing PZT Resonators in Vacuum and Air .....	77
CHAPTER 5 RESULTS AND DISCUSSION.....	80
5.1    Bond Integrity Results of Plasma-Activated Fusion-Bonded Wafers .....	80
5.2    Significance of RCA Cleaning .....	82
5.3    Sequential Plasma-Activation.....	83
5.4    Final Thermal Annealing Study.....	85

5.5	Evidence of Interfacial Oxide Layer in Plasma-Activated Si/Si Fusion-Bonding.....	87
5.6	Effect of Storage Time on Bond Strength .....	89
5.7	Plasma-Activated Si/SiO <sub>2</sub> Bonding .....	92
5.8	Plasma-Activation Before or After Storage.....	93
5.9	Modified Wafer Bonding Without Final Thermal Annealing .....	95
5.10	Bond Integrity vs. Storage of Plasma-Activated and Bonded Wafers.....	96
5.11	Vacuum-Cavity Seal-Integrity Measurements.....	98
5.12	Vacuum Cavities without Getter.....	101
5.13	Vacuum Cavities with Getter Layer .....	104
5.14	Vacuum Cavities with Getter Rings .....	108
5.15	High Film-Stress in Released Beams.....	111
5.16	Experimental Results of PZT Resonators in Vacuum and Air .....	112
CHAPTER 6 CONCLUSIONS AND FUTURE WORK.....		116
6.1	Conclusions.....	116
6.2	Future Work .....	118
APPENDIX A EQUIPMENT AND MATERIAL SPECIFICATIONS .....		120
APPENDIX B FABRICATION PROCESS RECIPES .....		122
B.1	HMDS & PT spin-coating .....	123
B.2	PZT spin-coating.....	123
B.3	SPR220 spin-coating.....	123
B.4	ICP Bosch Process .....	124
B.5	RIE Dry Etch Process .....	124
B.6	Pyrolysis recipe program for PT and PZT .....	124
B.7	PZT final annealing recipe program .....	125

## LIST OF TABLES

Table 5.1:	Table showing the bond strength measurements from tensile tests conducted on dies diced from wafers with 0 hr storage time.....	90
Table 5.2:	Tensile test results obtained from 24 hr stored, plasma-activated, and bonded wafers with respect to different shelf-lives.....	97
Table 5.3:	Results obtained from the pressure diaphragm-vacuum cavity wafer stack with no interfacial getter.....	101

## LIST OF FIGURES

Figure 2.1	(a-b). Illustration of the chemistry involved at the surface interface during wafer bonding of two silicon wafers (modified from [2]).	9
Figure 2.2.	Illustration of the covalent bond formed while pre-bonding the silicon wafers, with the release of water molecules (modified from [2]).	10
Figure 2.3.	Plot showing the increase in the surface energy between two wafers with increase in annealing time [6].	12
Figure 2.4.	Scanning acoustic microscopy images of Ar plasma-activated Si/Si and Si/SiO <sub>2</sub> wafers [5].	12
Figure 2.5.	Illustration showing the infrared light propagation through wafer-stack with trapped particulate at the interface [13].	13
Figure 2.6.	An NIR image showing the debonded regions as Newton rings at the interface.	13
Figure 2.7.	Illustration of the crack-opening method to measure surface energy between two bonded wafers [14].	14
Figure 2.8.	Dynamic NIR image of the crack-propagation method of measuring the surface energy between fusion bonded Si/Si wafer-stack [14].	15
Figure 2.9.	An illustration of the tensile test sample showing the device under test (DUT) placed in between an aluminum stud and a ceramic tile.	16
Figure 2.10.	HRTEM images of the changes in the interfacial oxide layer with increase in final annealing temperature (a) 400 °C (b) 800 °C (c) 1100 °C [17].	17
Figure 2.11.	An example of Raman intensity peak of H <sub>2</sub> at 4100 cm <sup>-1</sup> [27].	19
Figure 2.12.	Model showing water adsorption onto the SiO <sub>2</sub> surface. H-bonds are shown in bold lines [28].	20
Figure 2.13.	Specific model for the three-dimensional H-bonded network of H <sub>2</sub> O on a fully hydrated surface [28].	21

Figure 2.14. Presence of water molecules at the interface of two Si wafers, with hydrogen bridges between opposing silanol groups [28].	22
Figure 2.15. X-Ray Inspection image of voids in tape automated bonding solder joints [44].	27
Figure 2.16. Illustration of the experimental setup for measuring the deflection magnitude of the diaphragm (glass lid) under a pressure load, on an optical leak detector [46].	31
Figure 2.17. Illustration of the crystal lattice structure of PZT showing face-centered and body-centered arrangements of atoms.	33
Figure 3.1. Meshed Si diaphragm model in Comsol that employed quadrilateral mesh type elements.	40
Figure 3.2. Finite element solutions for the displacement of the diaphragm for applied load pressure in the negative z-axis.	44
Figure 3.3. Plot showing the finite element diaphragm deflection solutions obtained for diaphragm with varying thicknesses and for various pressure magnitudes.	45
Figure 3.4. Plot showing the average difference in deflection of diaphragm for various pressure magnitudes against various diaphragm thicknesses.	45
Figure 3.5. Illustration of the layers of the composite beam.	46
Figure 3.6. Plot showing the maximum tip displacement of the beam for varying beam length. $W_b = 350 \mu\text{m}$ .	48
Figure 3.7. Plot showing the maximum tip displacement of the beam for varying beam width. $L_b = 1000 \mu\text{m}$ .	49
Figure 3.8. Frequency vs. maximum tip deflection magnitude of undamped PZT composite beam with an actuating voltage $V_a = 50 \text{ mV}$ .	52
Figure 3.9. Modeled damped composite PZT beam with air-columns on the top and bottom surfaces of the cantilever beam.	54
Figure 3.10. Plot showing the results obtained from damped PZT beam analyses.	54
Figure 4.1. Picture of the wafer-stack clamped onto the fixture. Spacers are shown inserted between the wafers keeping the stack $100 \mu\text{m}$ apart.	57
Figure 4.2. Illustration of plasma-activation of Si wafers in an RIE chamber.	59
Figure 4.3. SEM micrograph of the interface of a cleaved die from a Si/Si wafer stack. Inset shows a close-up revealing the hairline interface.	60

Figure 4.4.	Illustration of KOH etching of die-stacks to obtain true interface for SEM imagery. ....	60
Figure 4.5.	Illustration of the cavity fabrication process. (a) Si wafer with 1 $\mu\text{m}$ oxide, (b) Photoresist spin-coating, (c) Exposure to UV light, (d) Developing, (e) BOE etching of oxide, (f) KOH etching of Si, and (g) Oxide stripping.....	62
Figure 4.6.	Picture of the dark-field mask used to pattern cavities into the Si wafer. ...	63
Figure 4.7.	Illustration of the fabrication process-flow for the pressure diaphragms and trace-guides on Si substrate. (a) Si wafer with top and bottom Al layer, (b) Photoresist spin-coated on both sides, (c) UV irradiation, (d) Resist development, (e) Al etching, (f) ICP etching, and (g) Al stripping. .	64
Figure 4.8.	Picture of the dark-field trace-guide mask used to pattern trace guides on the center of the pressure diaphragm (on the other side of wafer).....	65
Figure 4.9.	Dark-field pressure diaphragm mask showing circular patterns that would be ICP etched. ....	65
Figure 4.10.	Contour plot created in Excel from the etch-depth profile of ICP etched pressure diaphragms.....	67
Figure 4.11.	Illustration of the pressure diaphragm-vacuum cavity stack. ....	68
Figure 4.12.	NIR image of the pressure diaphragm-vacuum cavity wafer-stack showing a good bond quality with no debonded regions at the interface....	68
Figure 4.13.	Illustration of the trace followed by the stylus tip profilometer to measure the maximum deflection magnitude of the pressure diaphragm. (a) side-view (b) top-view.....	69
Figure 4.14.	Illustration of patterning and etching of Au bond-pads on the top Pt surface of the Si wafer. ....	72
Figure 4.15.	Illustration of the patterning and etching of top Pt and PZT layer using the top Pt light-field mask.....	72
Figure 4.16.	Illustration of the bottom Pt electrode and Ti adhesion layer etching using a light-field bottom Pt mask. ....	73
Figure 4.17.	Illustration of the $\text{XeF}_2$ patterning and etching of $\text{SiO}_2$ layer with a dark-field mask.....	74
Figure 4.18.	Picture of the device wafer showing the fabricated PZT cantilever beams. ....	74

Figure 4.19. Illustration of the device die containing four PZT beams on a Si substrate. ....	75
Figure 4.20. Picture of a packaged device die onto ceramic package. ....	76
Figure 4.21. Picture of the experimental setup of capacitance measurement of the devices using a Keithley test bench. ....	76
Figure 4.22. Picture of the experimental setup of PZT beam actuation in atmospheric air pressure. ....	78
Figure 4.23. Picture of the experimental setup for actuating PZT beam in vacuum. ....	79
Figure 5.1. Microscope image of the top surface of fusion-bonded Si wafer-stack showing stacking faults. ....	81
Figure 5.2. NIR images of fusion-bonded Si-Si wafers showing (a) a good bond (b) debonded regions at the interface revealed by Newton rings. ....	81
Figure 5.3. SEM micrograph of the interface region of a cleaved die diced from plasma-activated Si wafer stack. Inset: Close-up of the edge of the cleaved die showing a hairline of what was the interface between the two wafers. ....	82
Figure 5.4. NIR image of (a) wafers bonded with RCA treatment (b) wafers bonded without RCA treatment. ....	83
Figure 5.5. NIR images of the wafer-stack bonded after sequential plasma-activation in O <sub>2</sub> and N <sub>2</sub> plasma. ....	84
Figure 5.6. NIR image of plasma-activated and bonded wafer-stack annealed in an external tube furnace at 300 °C. ....	86
Figure 5.7. NIR image of wafer-stack annealed at 300 °C <i>in-situ</i> the substrate bonder immediately following pre-bonding. ....	86
Figure 5.8. Comparison of the NIR images of plasma-activated, 3 hr stored, and pre-bonded wafers annealed (a) in an external furnace (b) <i>in-situ</i> substrate bonder. ....	87
Figure 5.9. SEM micrograph showing the interface of a KOH etched die that was diced from a plasma-activated and fusion bonded wafer-stack. Inset shows a closer look at the inverted V-shaped feature at the interface. ....	88
Figure 5.10. An illustration of the etch profile followed by KOH etching on two opposing Si wafers, which was the primary reason for the inverted V-shaped etch feature at the interface. ....	88

Figure 5.11. Plot showing the bond strength magnitudes of wafers stored for varying time intervals before being pre-bonded. ....	90
Figure 5.12. Pictures of the NIR images of wafers stored for (a) 0 hr, (b) 3 hr, (c) 6 hr, (d) 12 hr, (e) 24 hr, (f) 48 hr, (g) 72 hr, and (h) 168 hr after plasma-activation and before bonding.....	91
Figure 5.13. Plot showing the increase in the oxide thickness with increase in storage time of plasma-activated wafers. ....	92
Figure 5.14. Comparison of NIR images of (a) Si-SiO <sub>2</sub> and (b) Si-Si plasma-activated wafers both stored for 48 hr. ....	93
Figure 5.15. NIR images of Si-SiO <sub>2</sub> where (a) both wafers were plasma-activated (b) only the Si wafer was plasma-activated. ....	93
Figure 5.16. NIR images of bonded wafer-stack comparing the wafer-pairs that were plasma-activated (a) before 48 hr storage time (b) after 48 hr storage time. ....	95
Figure 5.17. NIR images of wafer-stacks at (a) 0 hr (b) 24 hr (c) 48 hr (d) 120 hr (e) 144 hr (f) 168 hr (g) 312 hr (h) 336 hr after being plasma-activated and fusion bonded.....	97
Figure 5.18. Illustration of the basic geometrical shapes that make up the diaphragm-cavity enclosure. ....	98
Figure 5.19. A drawing of (a) spherical cap (b) spherical cap with segment plane (in the middle) parallel to the spherical segments (top and bottom). ....	99
Figure 5.20. Plot showing the average change in the volume of vacuum cavities over one month period. ....	102
Figure 5.21. Plot showing the cavity enclosure volume, for cavities without any getter, across wafer before and after introducing wafer into vacuum chamber.....	104
Figure 5.22. Illustration of oxide gettering layer around vacuum cavity. ....	105
Figure 5.23. Plot showing the average change in the volume of the vacuum cavities with oxide getter over a one month period. ....	107
Figure 5.24. Plot showing the cavity enclosure volume, for cavities with oxide getter, across the wafer before and after introducing the wafer into the vacuum chamber.....	107
Figure 5.25. Comparison of the pictures of (a) Dark-field vacuum-cavity mask and (b) Light-field oxide getter-ring mask. ....	109

Figure 5.26. An illustration of the oxide getter rings around a vacuum cavity in a Si substrate. ....	109
Figure 5.27. Plot showing the average change in the volume of vacuum cavities with oxide getter rings over a one month period. ....	110
Figure 5.28. Plot showing the cavity enclosure volume of cavities, with oxide getter rings, across wafer before and after introducing wafer into vacuum chamber. ....	111
Figure 5.29. SEM micrograph of a curled PZT composite beam as a result of high film-stress. ....	112
Figure 5.30. SEM micrograph showing the released PZT composite beam. No significant film stress was evident. ....	113
Figure 5.31. Comparison of the FEA and experimental results obtained for maximum tip deflection magnitude of the PZT beam at a resonant frequency of 1080 Hz. ....	114
Figure 5.32. Plot showing a comparison of theoretical and experimental results obtained for an air-damped PZT beam at different ambient pressures. ....	115
Figure 6.1. Illustration of vacuum-packaged PZT microcantilevers with buried feed-through interconnects and bond-pad interconnects. ....	119

## **ACKNOWLEDGMENTS**

I would like to extend my sincerest gratitude to the following people who played an integral role in the successful completion of my doctoral research at Louisiana Tech University. First and foremost, I thank my doctoral advisor Dr. Chad B. O’Neal for mentoring me throughout my stay at Louisiana Tech. I thank him for all the guidance and support he has given me. While focusing on my own research, he gave me the freedom to collaborate with many other research groups at Louisiana Tech. This molded me into a better researcher and engineer. I express my gratitude for all the financial support he rendered to me during the course of my research. I also want to thank the faculty and staff members of the Institute for Micromanufacturing for helping me with the different areas of my research. I thank Mr. Dee Tatum and Dr. Alfred Gunasekaran for helping me with various physical layer deposition techniques. Dr. Gunasekaran has trained me on several metrological equipments, like the scanning electron microscopy, surface profiler, atomic force microscope, etc. I thank Mr. John McDonald for helping me with reactive ion etching techniques. I extend my special thanks to Mr. Ji Fang for all his help with inductive coupled plasma etching and mask pattern generations. Futhermore, I thank my friends Dr. Tom John and Dr. Bobby Mathew, and all my research group members for their timely help during the different stages of my research. Finally, I thank my parents for their prayers and support in times when everything seems to fall apart. Also, I thank God for his blessings and strength.

# **CHAPTER 1**

## **INTRODUCTION**

This dissertation documents the research conducted at Louisiana Tech University in developing and fabricating a design-process flow for the purpose of vacuum-packaging MEMS devices, particularly PZT microcantilevers. The fabrication processes detailed in this work was designed to be able to be integrated into an industrial fabrication process flow. This chapter provides the readers with an introduction to the topic by defining some fundamental concepts like wafer-level bonding, plasma-activation, vacuum-packaging, microfabrication, etc.

### **1.1 Wafer Bonding**

Driven by the ever-shrinking size and increased functionality of electronic devices three-dimensional stacking of electronic components/circuits have been extensively investigated and implemented. Some examples of the multi-level stacking of components are multi-level memory stacking, three-dimensional integrated circuits, vacuum packaging of micro resonators and actuators, multi-junction solar cells etc [1-4]. Wafer-level bonding is one of the techniques employed to stack multiple layers of electronic devices on top of each other. Apart from a reduced electronic footprint, wafer-level bonding increases yield and reduces production cost.

Wafer bonding refers to the permanent joining of two wafer substrates with or without using an intermediate layer. Some of the commonly used wafer-bonding techniques are direct fusion bonding, anodic bonding, eutectic bonding, and thermo-compression bonding. Anodic bonding involves ionic exchange between the bonding substrates under the influence of temperature, pressure, and electric potential. A common example is the anodic bonding of Pyrex glass and Si commonly used in microfluidic applications. Sodium oxide ( $\text{Na}_2\text{O}$ ) present in Pyrex glass provides  $\text{Na}^+$  ions for exchange with  $\text{OH}^-$  ions from the Si substrate. The migration of  $\text{Na}^+$  ions into the Si substrate and the  $\text{OH}^-$  into the glass substrate creates strong electrostatic attraction forces at the interface of the two substrates thereby hermetically sealing them in the process. Increased temperature and electric potential facilitates the migration of ions across the interface. Eutectic bonding involves the bonding of substrates with low melting point eutectic alloys applied at the interface, while thermo-compression bonding is commonly used in bonding substrates with a metallic layer like gold, where temperature and pressure fuses the two opposing gold surfaces together.

## 1.2 Micro Electro Mechanical Systems

Micro electro mechanical systems (MEMS) are devices/systems in the micro-scale. The idea of MEMS technology was proposed initially by Richard Feynman's famous lecture of 1959 entitled "There's plenty of room at the bottom". Microfabrication technology or processes did not exist when such an innovative idea was proposed. However, with the advancement in science and technology, several innovative fabrication methods were studied, developed, and implemented. MEMS became popular with advancements in silicon fabrication, metal deposition and etching techniques, wet/dry

substrate etching techniques, like inductively coupled plasma, reactive ion etch, etc. Silicon was the primary substrate of choice when MEMS devices were first fabricated. Hence, several processes and procedures were developed exclusively for silicon microfabrication. Some of the basic MEMS processes are photolithography, metal deposition, metal wet/dry etching, silicon wet/dry etching, etc.

#### 1.2.1 Photolithography

As the name suggests, this process is used in microfabrication by utilizing light, specifically ultra-violet radiation, to pattern and develop a photo-sensitive layer, known as photoresist, to create a masking layer for the substrate underneath. This polymer mask would protect the underlying layer during etching of the exposed areas, thereby transferring the patterns on the photo-sensitive polymer onto the underlying substrate.

#### 1.2.2 Metal Deposition

This step involves depositing of metallic layers of specific thicknesses onto a substrate for specific processes. Several deposition methods were optimized in order to obtain consistent film properties, quality, thickness, etc.

#### 1.2.3 Metal Wet/Dry Etching

This step involves etching of a particular metallic surface using a wet chemical or dry plasma process. Some examples of wet chemical etchings are as follows: etching of aluminum using transene aluminum etchant (contains 80% phosphoric acid, 5% nitric acid, 5% acetic acid, and 10% deionized water), gold etching using aqua regia solution, etc. An example of dry etching techniques is chlorine etching of platinum using reactive ion etching.

#### 1.2.4 Silicon Wet/Dry Etching

Silicon substrates are wet etched using potassium hydroxide solution, TMAH, etc. Dry etching involves inductively coupled plasma etching using SF<sub>6</sub>.

MEMS devices are made up of individual components with dimensions ranging from 1 to 100 μm and overall device size range from 20 μm to 1 mm. Some applications where MEMS devices are employed are as accelerometers in automobile airbags, gyroscopes in cellphones, resonators in anti-tamper sensors, etc. Successful MEMS device fabrication depends on controlling environmental parameters like temperature, humidity, dust particulates in ambient air, etc. These parameters are controlled through carrying out the MEMS device fabrication processes in the controlled environment of a clean room.

### **1.3 Project Overview**

The main objective of this research was to create a fabrication process for vacuum encapsulating MEMS devices between two silicon substrates. With the reduction in the size of the footprint on which electronic devices can be placed and with the need for increased functionality, three-dimensional integration of electronic components was necessary. This was carried out through wafer-level bonding of substrates containing the MEMS devices. Chapter 2 discusses the optimization techniques carried out to develop a recipe for bonding wafer-level substrates in order to encapsulate microdevices in vacuum. Surface and interface chemistry before, during, and after bonding were studied in detail in Chapter 3. For the purpose of optimizing a fabrication process flow for vacuum-packaging MEMS devices, vacuum cavities that would contain the devices were fabricated. Methods to monitor and test the vacuum levels in the cavities were

investigated and implemented, and are detailed in Chapter 4. Finally, piezoelectric microcantilevers were fabricated on a silicon substrate. These devices were tested in ambient atmospheric pressure and vacuum pressure in order to compare the operating performance under each condition. These processes are detailed in Chapter 5 and the problems encountered during fabrication and testing are outlined in detail. The steps taken to solve these problems are also discussed.

#### **1.4 Research Motivation**

Wafer-level bonding has been used in the past for three-dimensional stacking of electronic components. However, the subjecting of the substrates to be bonded to the high temperature steps of the final thermal annealing stage could change the diffusion profile of dopants in the Si in addition to changing its material properties. High temperatures of 1000 °C could have detrimental effects on metals or polymer layers that makeup the electronic components. Hence, an alternative method to thermally anneal the pre-bonded wafer-stack was necessary. Plasma-activation is one such method that involves dry surface-activation of surfaces to be bonded. This way, the highly reactive bonding surfaces does not require high thermal annealing temperatures to obtain a permanent and strong covalent bond at the interface. Plasma-activation of Si substrates has been extensively studied in the past. However, the type of plasmas/gases used in plasma-activation was contingent upon their compatibility with polymers or passive layers on the substrate. Therefore, it was imperative to optimize a plasma-activation recipe to suit Si substrates with organic piezoelectric polymers, like lead zirconate titanate.

Vacuum-encapsulation of MEMS devices in Si using glass substrates has been studied in the past. Glass substrates have been employed as a reliable capping layer for

vacuum packages. However, this poses as a termination layer for three-dimensional stacking, as it would be challenging to integrate another substrate (with electronic components) atop the glass-capping layer. Replacing the glass capping substrate with a Si substrate facilitates the continuation of three-dimensional stacking, since Si is a commonly used substrate for manufacturing electronic components. Thus, it was necessary to investigate vacuum-encapsulation of MEMS devices in Si substrate using a capping Si substrate with other MEMS devices. Some of the challenges faced in maintaining the integrity of the vacuum level in packages are the prevention/minimization of real and virtual leaks. Real leaks are comprised of ambient air seeping into the packages and reducing the internal vacuum level of the packages. Virtual leaks are comprised of interfacial gaseous molecules propagating into the vacuum cavities and reducing the package vacuum level. Hence, it was necessary to find remedies to maintain the vacuum pressures in packages using suitable gettering agents.

## 1.5 References

- [1] S. S. Iyer and A. J. Auberton-Herve, in *Silicon Wafer Bonding Technology for VLSI and MEMS applications*, London, UK: INSPEC, 2002.
- [2] Q. Y. Tong, "Wafer bonding for integrated materials," *Materials Science and Engineering B: Solid-State Materials for Advanced Technology*, vol. 87, pp. 323-328, 2001.
- [3] J. M. Zahler, A. F. Morral, C.G. Ahn, H. A. Atwater, M. W. Wanlass, C. Chu, and P. A. Iles, "Wafer bonding and layer transfer processes for 4-junction high efficiency solar cells," in *Proc. IEEE Photovoltaic Specialists Conference*, 2002, pp. 1039-1042.
- [4] M. J. Keevers, "Fabrication and characterisation of parallel multijunction thin film silicon solar cells," *Solar Energy Materials and Solar Cells*, vol. 65, pp. 363-368, 2001.

## CHAPTER 2

### LITERATURE REVIEW

This chapter is dedicated to the various research work carried out in those areas that pertain to the research works documented in this dissertation. Readers are made aware of recent developments in the field of wafer-level bonding and packaging, and the different techniques employed to evaluate seal integrity of vacuum packages.

#### 2.1 Direct Fusion-Bonding and Testing Methods

Direct fusion bonding involves the bonding of like-substrates, such as two Si wafers, using only temperature and pressure (no adhesive layer) and producing nearly perfect hermetic seals. This method requires the mating surfaces to be highly polished (average roughness less than 2 nm). In addition, the pre-bonded substrates need to be annealed at high temperatures ranging from 800-1000 °C for several minutes. Other factors that affect the bond quality and strength are wafer bow and etch patterns on the surface of the wafers [1]. The chemistry involved in fusion bonding is illustrated in Figure 2.1. Si wafer surfaces have silanol groups (OH) that are ready to bond with opposing silanol groups from other Si wafer surfaces, as illustrated in Figure. 2.1(a). When the two Si wafer surfaces are brought in contact, the silanol group of one surface forms weak bonds with the silanol groups of the opposing wafer surface through hydrogen bridging, as illustrated in Figure 2.1(b). During the pre-bonding process, Si

atoms form permanent covalent bonds with oxygen atoms (O) forming Si-O-Si with the release of water molecules, as illustrated in Figure 2.2. It should be noted that the Si-O-Si covalent bond is formed after pre-bonding the wafers for a particular time period. It is crucial for the quality of the bond process that the released water molecules diffuse through the interface of the bonded wafers. However, these molecules have a tendency to cluster and form tetramer rings around a Si-OH:OH-Si bond during the pre-bonding process [2]. These tetramer rings are usually 0.4 nm in diameter and therefore have great difficulty in diffusing through the interface of the wafer stack, which is separated by an interfacial gap of 0.32 nm [1]. A. Berthold, et al. concluded that no appreciable Si-O-Si formation takes place at the interface so long as there is a presence of water tetramer rings at the interface [2]. Strong Si-O-Si covalent bonds exist at a distance of 0.16 nm. Therefore, strained Si-O-Si has a higher tendency to be rehydrated by water tetramer rings at the interface. The final thermal annealing step is responsible for breaking up these rings, thereby preventing the rehydration of Si-O-Si bonds. The typical final thermal annealing temperatures range from 1000 to 1100 °C. Such high temperatures can cause irreparable damage to doped SOI wafers by changing the doping profile within the substrate and precluding the use of most metals. This limits the application of direct-fusion bonding of Si-Si to scenarios where such high annealing temperatures would not be critical. A high density of OH<sup>-</sup> groups at the interface is known to prevent the formation of tetramers [2-4]. Plasma-activation is a method commonly used to increase the density of OH<sup>-</sup> groups at the interface. Some of the commonly used plasmas are oxygen (O<sub>2</sub>), nitrogen, and argon [5-7]. Researchers have used several methods to plasma

activate wafer surfaces using  $O_2$  [8, 9]. A reactive ion etch (RIE) chamber was employed in this work in order to plasma activate Si wafers before pre-bonding.

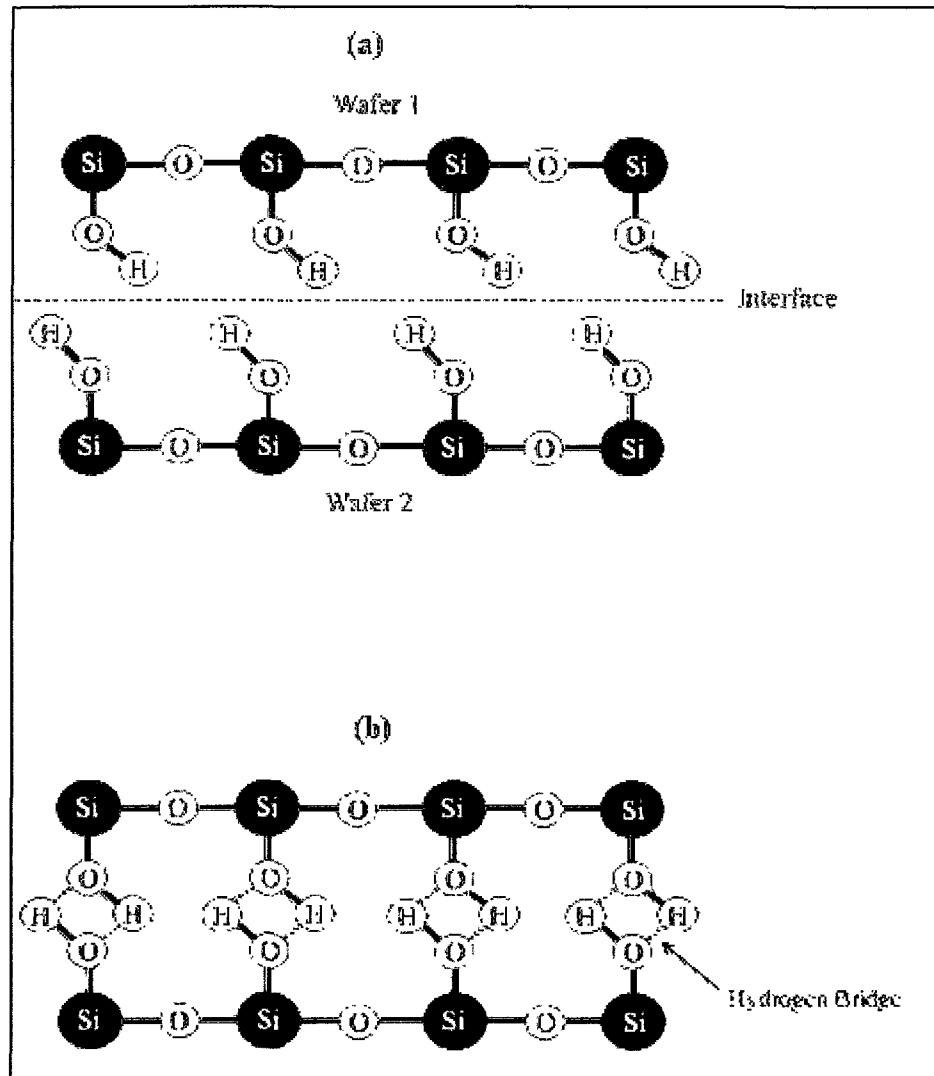


Figure 2.1 (a-b). Illustration of the chemistry involved at the surface interface during wafer bonding of two silicon wafers (modified from [2]).

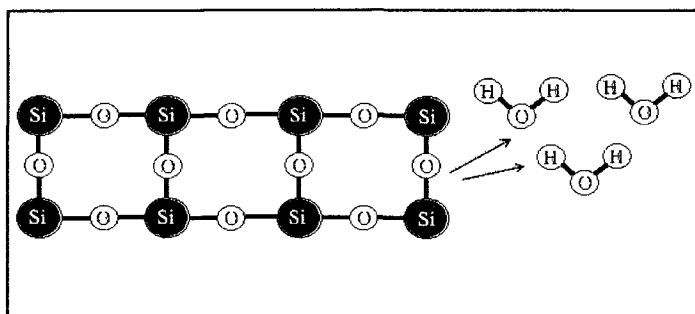


Figure 2.2. Illustration of the covalent bond formed while pre-bonding the silicon wafers, with the release of water molecules (modified from [2]).

Investigations on the various surface reaction effects of plasma-activated wafers were carried out [6, 10]. Increased density of OH<sup>-</sup> groups prevents the formation of tetramer rings, which prevents the rehydration of Si-O-Si covalent bonds. In addition, plasma-activation creates pores on the wafer surfaces that further aids in the diffusion of water molecules from the sides of the interface. The exact chemistry of plasma-activation cannot not be explained, as its mechanism has not been completely studied. However, it is known that plasma-activation using oxygen gives a hydrophilic and contamination-free wafer surface [11]. In addition, the surface energy of the wafers is increased with the ion bombardment in the RIE chamber. Figure 2.3 shows the results obtained by V. Dragoi, et al. where the effect of different types of plasma-activation was investigated for surface energy between the two wafers for corresponding annealing times [6]. As evident from the figure, an increase in the annealing time increases the surface energy. This effect can be attributed to the increased OH<sup>-</sup> group reactivity at the interface as a result of high annealing temperatures. In addition, an increase in the final annealing temperature can lead to a decrease in the probability of the formation of water tetramer rings at the interface, which in turn leads to increased surface reactivity. The bond quality can be determined qualitatively and quantitatively. Some of the qualitative methods employed to

determine the bond quality are with the help of transmission inspection techniques, such as near infrared (NIR) spectroscopy, acoustic microscopy, x-ray inspection, etc. [12]. Figure 2.4 shows the scanning acoustic microscope (SAM) images of plasma-activated and fusion bonded wafer pairs. Figure 2.4 (a) shows the trapped air-molecules at the interface of Si/Si wafers that were plasma-activated using Ar. These trapped air molecules create debonded regions at the interface thereby reducing the bond strength between the wafers. In contrast, Figure 2.4 (b) shows a clean bond with no trapped air molecules at the interface. While SAM images show trapped molecules at the interface directly, NIR imagery reveals the interfacial gas molecules as Newton rings thereby showing the debonded regions at the interface, as shown in Figure 2.5. NIR method of inspection was employed here in order to determine the quality of the bond. Debonded regions were revealed as Newton rings in the NIR image of the wafer stack. Most of the NIR inspection stations project IR rays on one side of the wafer-stack while recording the optical field at the other side by using a detector, such as an IR camera. Most of the incident IR light is transmitted through the stack, as Si is translucent to IR light. However, optical interference patterns are generated in areas with trapped gas molecules or dust particulates.

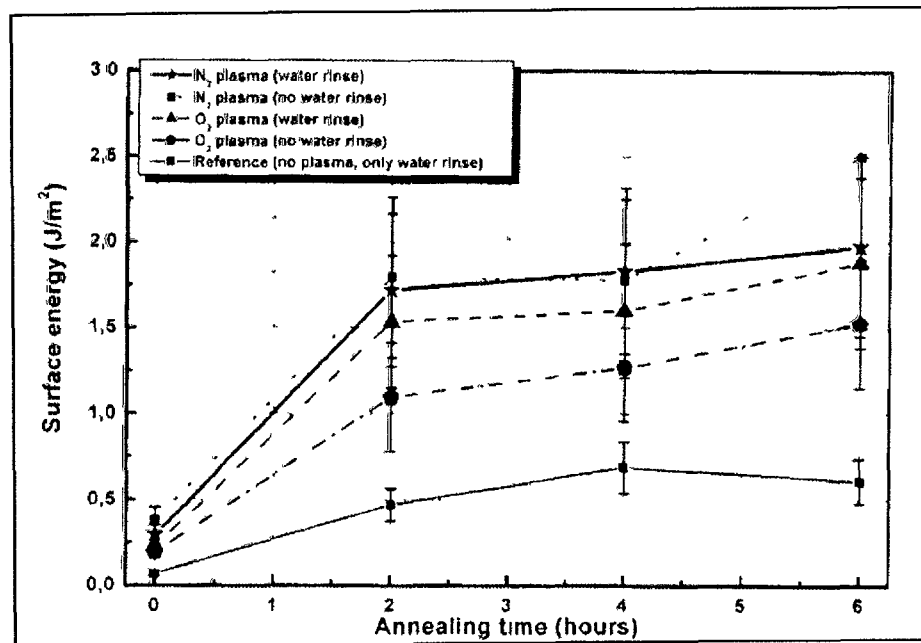


Figure 2.3. Plot showing the increase in the surface energy between two wafers with increase in annealing time [6].

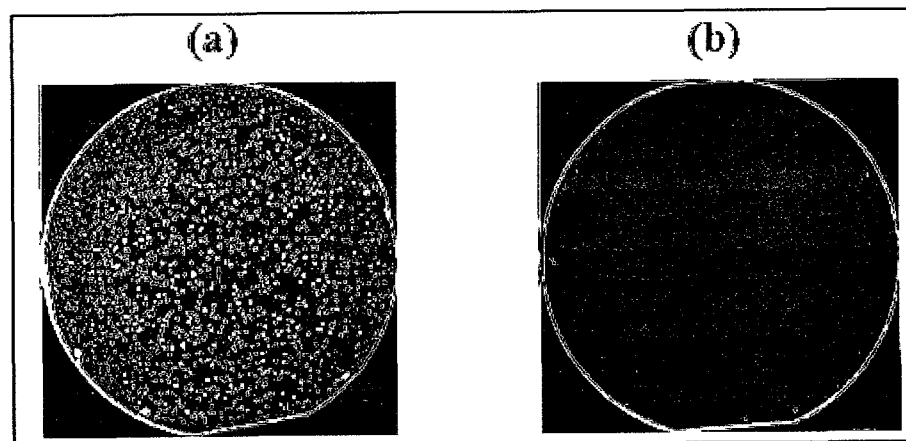


Figure 2.4. Scanning acoustic microscopy images of Ar plasma-activated Si/Si and Si/SiO<sub>2</sub> wafers [5].

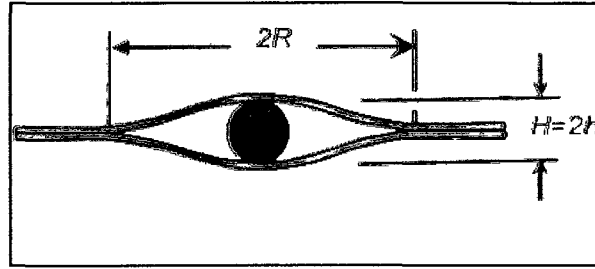


Figure 2.5. Illustration showing the infrared light propagation through wafer-stack with trapped particulate at the interface [13].

Debanded regions are evident as Newton rings through light reflected from the air-Si interface. The height  $H$  of the debanded region can be calculated from the following Equation (2.1).

$$H = N\lambda / 2 \quad (2.1)$$

$N$  is the number of fringes in the Newton ring and  $\lambda$  is the wavelength of the IR light. Figure 2.6 shows an example of an NIR image with debanded regions, shown as Newton rings, at the interface of the wafer-stack.

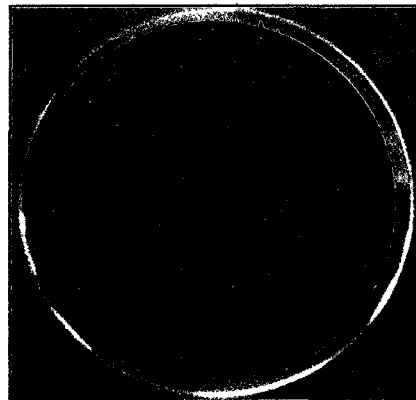


Figure 2.6. An NIR image showing the debanded regions as Newton rings at the interface.

The commonly used methods for quantitatively measuring the bond quality between two wafers in the form of bond strength are the crack propagation method and

tensile test method. In the former technique, a separating material, like a sharp razor blade, is inserted in between the interface of two wafers that causes the wafer pair to be debonded. NIR images of the wedged razor in the wafer-stack reveals the propagation of cracks away from the debonded region. Large debonded regions are evident as Newton rings, and the surface energy between the wafers is calculated from the length of the crack from the debonded region [14]. C. Liguio, et al. [14] used Equation (2.2) to calculate the surface energy  $\gamma$  between the bonded wafers using the parameters illustrated in Figure 2.7.

$$\gamma = \frac{(5R-2L)Eb^3t^2}{\lambda(64RL^4-32L^5)} \quad (2.2)$$

$R$  is the radius of the wafer,  $L$  is the length of the crack-propagation,  $E$  is the Young's modulus of the wafer material,  $t$  is the thickness of individual wafers (assuming the two wafers are of equal thicknesses), and  $\lambda$  is the wavelength of the IR light.

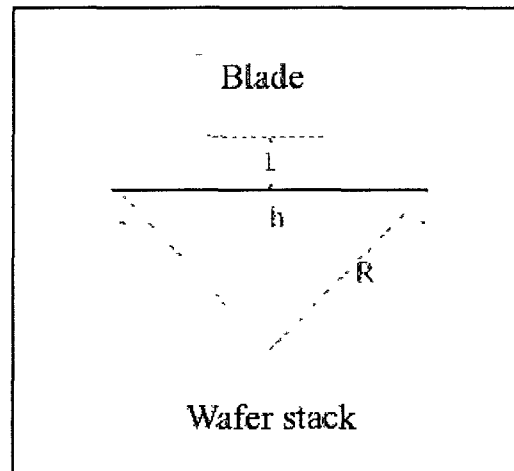


Figure 2.7. Illustration of the crack-opening method to measure surface energy between two bonded wafers [14].

Figure 2.8 shows the crack-opening line propagation while dynamically inspecting the wafer-stack using NIR imagery. In the latter technique, the wafer is diced into individual dies that are pulled apart. The bond strength between the wafers is measured using a tensile test station. An example of tensile tests conducted on a die stack diced from a bonded wafer pair can be found in [15]. Both techniques require a destructive method for measuring/calculating the bond energy between the wafers.

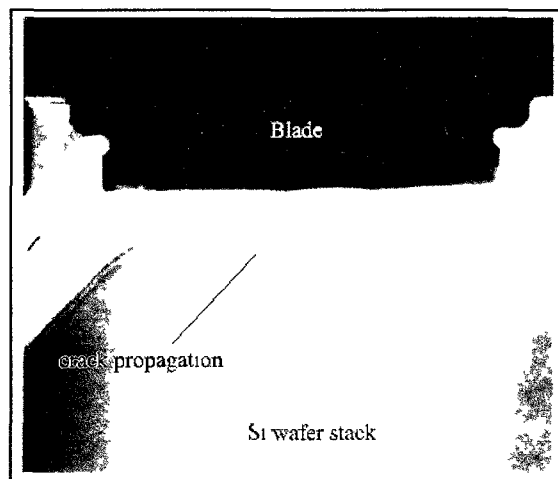


Figure 2.8. Dynamic NIR image of the crack-propagation method of measuring the surface energy between fusion bonded Si/Si wafer-stack [14].

Figure 2.9 shows an illustration of the sample setup for pull-testing a die stack in order to calculate the bond strength between the dies. The device under test (DUT) is placed in a ring that allows the Al stud to be pulled through while holding back the ceramic tile. In this way, the top and bottom substrates of the die are pulled apart. Bond strength between the substrates is determined as the pressure at which the interfacial bond fails.

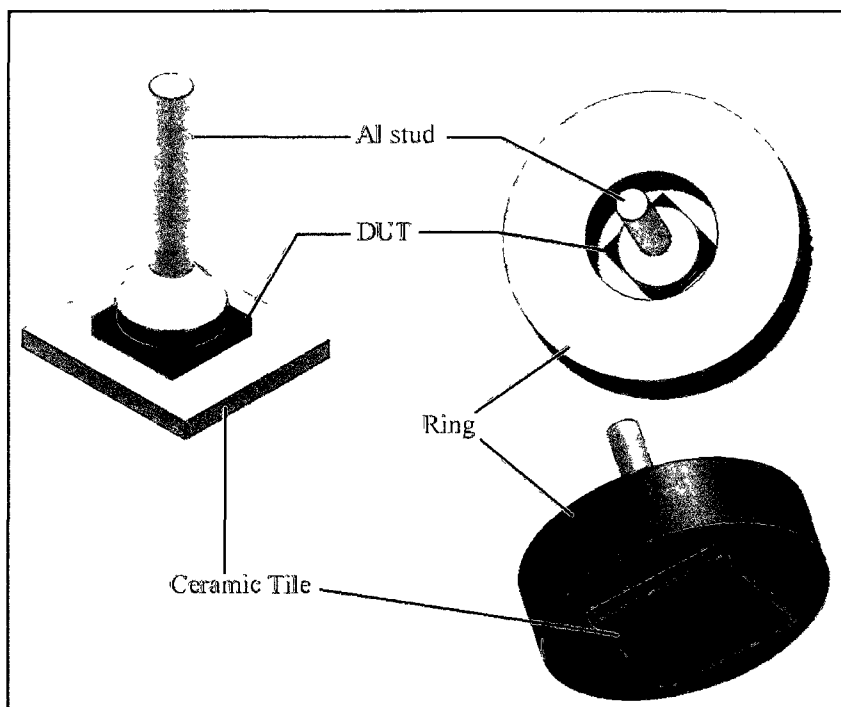


Figure 2.9. An illustration of the tensile test sample showing the device under test (DUT) placed in between an aluminum stud and a ceramic tile.

## 2.2 Investigation Techniques on Buried Oxide Layer

Much attention has been given to the bonding mechanism at the interface of two Si wafers. Special investigations have been conducted on the atomic arrangement at the buried interface [16]. The thickness of the interfacial oxide layer increases at the final thermal annealing stage [17]. Since the oxide layer is buried, non-destructive methods like infrared spectroscopy are usually used to measure the stoichiometry, thickness, structure, etc. Using multiple internal reflective ellipsometry, the chemical composition and orbital states of the oxide layer can be determined. Thicknesses of the interfacial oxide layer can be measured using high-resolution transmission electron microscopy (HRTEM) by measuring the cross-section of the bonded wafer-stack, as shown in Figure 2.10.

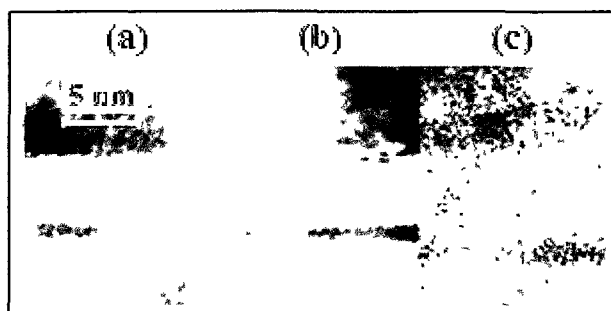


Figure 2.10. HRTEM images of the changes in the interfacial oxide layer with increase in final annealing temperature (a) 400 °C (b) 800 °C (c) 1100 °C [17].

Even though HRTEM provides detailed information, it is still a destructive method of analyzing the interfacial profile of bonded wafers. Up to now, IR spectroscopy is the only non-destructive method of inspecting the interface of pre-bonded wafer stacks. Changes in the interfacial oxide during final thermal annealing has been a topic of several studies [18, 19]. It was concluded that the interfacial oxide layer increases with an increase in the final thermal annealing temperature and time. However, a saturation of the oxide thickness was observed at about 1000 °C [20]. The internal structure of the interfacial oxide layer was studied and found to be the same as the surface oxide layer atop a Si substrate [17]. The increase in the buried interfacial oxide layer thickness is also influenced by decomposition of water molecules. This was found to occur at bonding temperatures less than 400 °C. At temperatures greater than 400 °C the silanol species decompose, which leads to the increase in the interface oxide thickness. At higher temperatures of 800-1100 °C, the oxygen from the bulk Si is known to diffuse into the SiO<sub>2</sub> layers further oxidizing the Si. Oxidation takes place at the Si-SiO<sub>2</sub> interface.

D. Feijoo, et al. studied three types of forces known to be involved during fusion bonding and annealing [21]: weak Van der Waals forces, moderately strong H-bonding, strong covalent Si-O-Si bonds in hydrophilic fusion bonds, and Si-Si bonds in

hydrophobic bonds. At bonding temperatures greater than 150 °C, water monolayers and Si-OH groups are found at the interface. At temperatures ranging from 300-600 °C, the orientation of water molecules is restricted. For temperatures greater than 800 °C, the Si-OH groups disappear. Apart from being a non-destructive means of profiling the chemistry of the interface, infrared spectroscopy is sensitive to the chemical and bonding nature of the interface of bonded wafers. For example, Van der Waals interactions are revealed as shifts in IR peaks (few  $\text{cm}^{-1}$ ), while the presence of hydrogen bonds produces large shifts (greater than 100  $\text{cm}^{-1}$ ) with strong peak-shifts. D. Feijoo, et al. studied the chemical changes at the interface of wafers before and after pre-bonding, and at short annealing intervals, using advanced IR spectroscopy [22]. Though short annealing times fail to produce a stable interfacial chemical state, these studies helped reveal the kinetically limited reactions taking place with the increase in final annealing temperature. Samples investigated for interfacial chemistry profile were beveled at two opposing edges and IR rays were radiated into one end. The multiple internal transmission infrared spectroscopy studies have revealed that RCA and plasma-activation before bonding attacks the Si-O-Si and water molecules from the atmosphere then hydrate to form Si-OH groups, as shown by the reaction below.



This equation is the reason for the increase in the density of silanol groups after RCA and plasma-activation. The increased silanol at the surfaces of activated wafers is known to also increase the adsorption of water molecules. During annealing most of the molecular water diffuses away from the bonded interface into the oxide layer reaching the Si crystal and oxidizing it [23]. A wafer that is RCA treated has isolated (no H-bond) Si-OH

groups. These groups do not contribute to the bonding mechanism. In  $O_2$  plasma treated wafers the Si-OH species are H-bonded and contribute to the bonding mechanism. As mentioned previously, water released as the byproduct of the covalent Si-O-Si gets reabsorbed and reoxidises the Si at the Si-SiO<sub>2</sub> interface releasing H<sub>2</sub> in the process. Some of the released H<sub>2</sub> is known to be absorbed in the oxide layer, but the remaining gets trapped in the interface. However, the absorption of the H<sub>2</sub> molecule is possible only by a thick oxide layer [24]. In the past, the presence of H<sub>2</sub> has been identified by Raman spectroscopy [25, 26]. Typical molecular H<sub>2</sub> wavelength peaks are found around 4000-4100 cm<sup>-1</sup>. An example of a Raman intensity peak with H<sub>2</sub> peaks is shown in Figure 2.11.

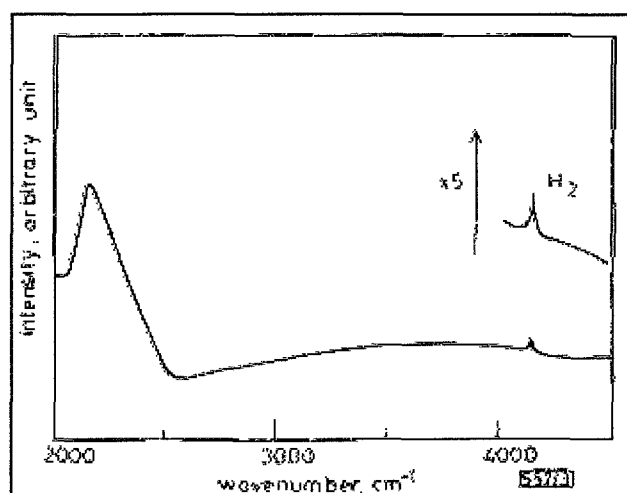


Figure 2.11. An example of Raman intensity peak of H<sub>2</sub> at 4100 cm<sup>-1</sup>[27].

The oxide layer on a Si wafer surface has been related to fused silica due to their similar properties [28]. Two opposing Si wafers behave like two conducting planes very close to each other. The absence of any alkaline impurity could change the binding energies of adsorbed molecules at the interface: quite opposite in the case of insulated silica. Residual valencies of a SiO<sub>2</sub> substrate surface is highly hydrophillic and react with

H<sub>2</sub>O. Therefore, there is an increased density of OH groups on the surface at room temperature. This is the same case for non-porous amorphous silica that is fully hydroxylated and contains four to six Si-OH groups per 100Å<sup>2</sup> [28]. Water is adsorbed onto the silica surface at atmospheric pressure and temperature, as shown in Figure 2.12. Subscripts “I” and “II” indicate the different stretching frequencies in the IR spectra. J.H Anderson and K.A Wickersheim investigated the presence of two types of H<sub>2</sub>O and OH groups on the silica surface with the help of IR spectroscopy [29].

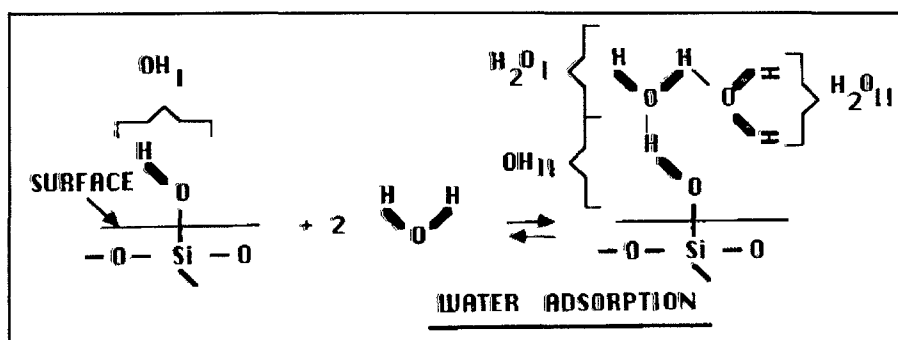
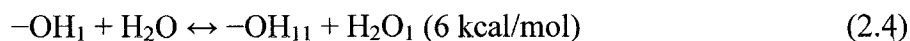
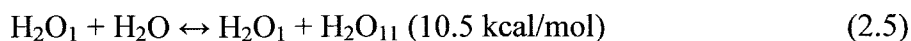


Figure 2.12. Model showing water adsorption onto the SiO<sub>2</sub> surface. H-bonds are shown in bold lines [28].

The adsorption of H<sub>2</sub>O was written into a reaction equation as shown below.



The subscripts “1” and “11” shows the different stretching frequencies in the IR spectra. It was also concluded that the probability of H<sub>2</sub>O adsorption on isolated SiOH groups was significantly low. Additional adsorption of H<sub>2</sub>O is shown by equation (2.5).



This H<sub>2</sub>O forms tetramer clusters at the SiO<sub>2</sub> interface before being adsorbed by all the Si-OH groups. W.K Thompson pointed out that a network of H-bonds are formed on a fully hydrated silica surface by the first monolayer of H<sub>2</sub>O [30]. The characteristics of

this arrangement of H-bonds involves oxygen pointing down ( $\text{H}_2\text{O}_1$ ) with hydrogen atoms pointing towards the surface, as shown in Figure 2.13. At temperatures greater than  $180\text{ }^\circ\text{C}$ , the adsorbed  $\text{H}_2\text{O}$  molecules detach from the network leaving behind a hydroxylated silica surface. Here, most of the Si-O groups are linked through hydrogen atoms. The surface chemistry of silica is similar to that of  $\text{SiO}_2$  on a Si wafer surface.

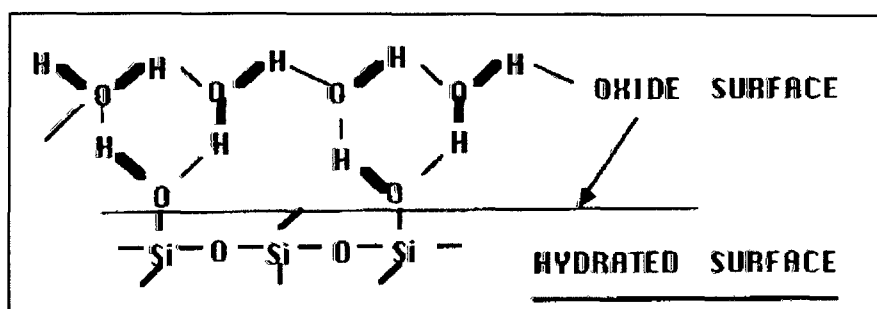


Figure 2.13. Specific model for the three-dimensional H-bonded network of  $\text{H}_2\text{O}$  on a fully hydrated surface [28].

As mentioned earlier, during the wafer bonding process hydrogen bridging develops between the oxygen and hydrogen atoms of the adsorbed  $\text{H}_2\text{O}$  molecules. These  $\text{H}_2\text{O}$  molecules, however, have a tendency to form tetramer rings with a diameter of  $4\text{ \AA}$  that makes it difficult to be diffused through the interface. In addition, the binding energy of the cyclic tetramer was calculated to be  $10\text{ kcal/mol}$ [31]. The tetramer binding energy is three times greater than the bonding energy of a single hydroxyl water bond, which was reported to be  $3\text{ kcal/mol}$ . Figure 2.14 shows the presence of water clusters at the interface with hydrogen bridges between the silanol groups. As discussed earlier, the high final annealing temperatures gives the  $\text{H}_2\text{O}$  clusters enough kinetic energy to breakup and diffuse through the interface, thereby preventing a rehydration of the Si-O-Si covalent bond formation at the interface.

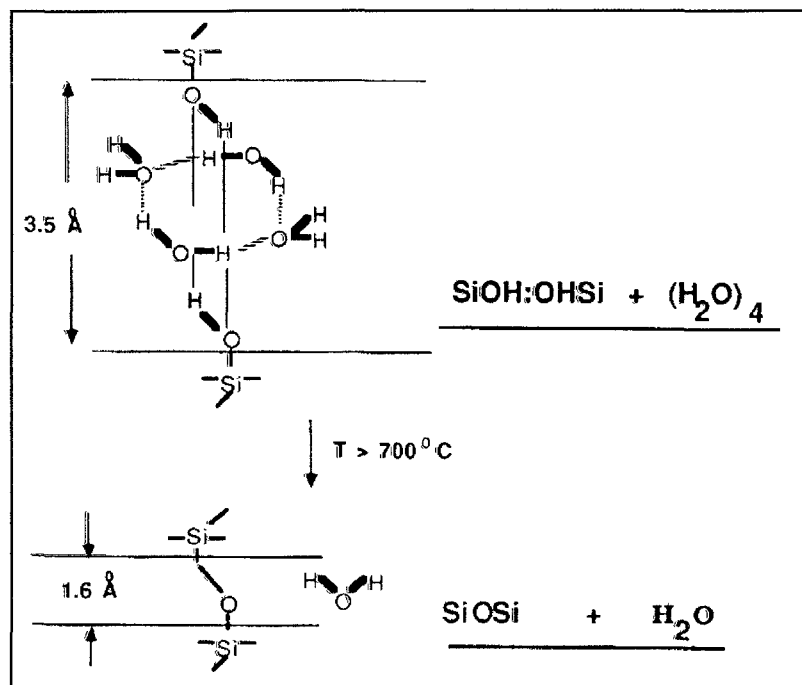


Figure 2.14. Presence of water molecules at the interface of two Si wafers, with hydrogen bridges between opposing silanol groups [28].

### 2.3 Vacuum Packaging and Testing Methods

Resonators have been extensively used for various applications ranging from biosensors and molecular sensors to resonators/actuators for high and low frequency applications [32, 33]. An extensive study has been conducted on operating microcantilever resonators in vacuum. The absence of an air-damping medium increases the quality factor (Q-factor), narrows the bandwidth, thereby increasing the accuracy of the device to operate at a particular frequency, etc. The Q-factor of a vibrating device has been modeled extensively in the past. L.D Landau and E.M Lifshitz have studied and analytically modeled the fluidic solution for a vibrating structure [34]. R.K Kapania, et al. modeled such a structure using the COMSOL Multiphysics™ tool where they studied the effect of Rayleigh damping on energy harvester devices and the impact on its

efficiency and accuracy [35]. Quality factor (Q-factor) is a parameter that characterizes the bandwidth of a resonator to its resonant frequency, as shown in Equation (2.6).

$$Q = \frac{f_r}{\Delta f} \quad (2.6)$$

$f_r$  is the resonant frequency and  $\Delta f$  is the bandwidth of the resonator. An increase in Q-factor is realized by the reduction in bandwidth. A low bandwidth resonator can be used in applications where the operating device needs to respond to a particular frequency. The reduction in the resonator bandwidth can be achieved by eliminating the damping factor in the device, which is accomplished by operating the device in vacuum. This is the reason for the increased interest in vacuum encapsulation of micro-resonators and actuators.

One of the major challenges in obtaining vacuum cavities between substrates is the maintenance of a hermetic seal. Several methods have been employed to achieve hermetic sealing of two substrates. One of the common ways to hermetically seal cavities in vacuum is to use an intermediate layer. The choice of hermetic sealants depends on the method of sealing as well as the equipment to be employed. General hermetic sealants are metals, polymers, inorganic glasses, etc. Most metal sealants are commonly used in applications where the expected lifetime of the device is greater than ten years with an operating temperature range of -55 °C-150 °C, and commonly used in military, space, and aviation applications. Commonly used inorganic glass sealants are used in applications where devices employing such materials are expected to last five to ten years under operating temperatures of -20 °C-65 °C. Commercial, consumer, and industrial applications are some of the areas where glass-frit hermetic sealants are commonly employed. Polymer materials are not commonly used as hermetic sealants due to their

outgassing probabilities. Nevertheless, they have been used as quasi-hermetic or near hermetic sealants for applications where devices are expected to last not more than five years [36, 37]. When using intermediate layers for sealants, intermediate layer bonding methods like eutectic bonding is used. Low melting point alloys are commonly used in eutectic bonding, like Au/Sn, Sn/Ag, etc [38, 39]. Other criteria for choosing an optimal solder for eutectic bonding are resistance to corrosion, compatibility with harsh environments, etc. AuSn solders have been used extensively in critical applications even though the solder melting point/eutectic point is 280 °C. Solder bonding involving materials containing Sn have been employed recently[40]. Welding is another method of hermetic bonding using an intermediate layer between bonding substrates. It is commonly carried out using laser or electron beam [41, 42]. In welding bonding, the application of energy is directed exclusively to the mating region. This reduces heating of adjacent components (that may be temperature-sensitive) through localized heating. Other types of intermediate adhesive layer bonding include glass-frit method (mentioned briefly earlier). One of the common methods used to dispense glass-frits (that are compatible with MEMS devices) onto the bonding substrates is screen-printing. Following a drying cycle, the temperature of the substrates is raised to greater than 400 °C in order to volatilize any binders. Once the bonding surfaces are mated, the temperature of the substrate-stack is raised above the melting point of glass-frit. Other methods of intermediate bonding involve the spin-coating of benzocyclobutene (BCB), SU8, and polyimide materials. However, the major disadvantage of using organic polymers at the interface is permeability of the sealant, as well as the increased probability of outgassing. Direct bonding is a hermetic sealing method used without any interfacial layer. Some examples

of direct bonding include fusion bonding, anodic bonding, friction stir bonding, diffusion bonding, etc. Anodic bonding is commonly used in hermetically sealing MEMS devices in Si using glass-capping substrate. Here, borosilicate glass (containing  $\text{Na}^+$  ions) is brought into contact with the Si substrate (containing  $\text{OH}^-$  ions) using temperature (typically  $300\text{ }^\circ\text{C}$ ) and pressure ( $2 \times 10^{-4}\text{ mBar}$ ) with an applied potential difference of 800 V. The migration of  $\text{Na}^+$  ions from the glass substrate to the Si interface and the  $\text{OH}^-$  ions from the Si substrate to the glass interface creates a strong electrostatic attraction force at the interface. This force of attraction is responsible for the hermetically sealing of glass to Si. Bonding in vacuum achieves vacuum pressure levels in cavities between the glass and Si. One of the major criteria for a successful bonding is that the mating surfaces should have an average surface-roughness of less than 20 nm. Diffusion bonding is a type of metal-to-metal bonding where physical pressure and temperature are applied. Sometimes interfacial layers are employed in order to enhance bonding, although these materials are not adhesives. The mating surfaces are kept in close contact during the bonding process. Another metal-to-metal bonding technique is friction stir bonding, commonly used with Al and Al alloys. Bond integrity for metal-to-metal bonding is determined through peel strength testing, lap shear testing, and burst testing.

Diffusion bonding is carried out using temperature and pressure, without any adhesive layer. The bonding mechanism was detailed in previous sections. Vacuum cavities in Si/Si substrates were fabricated and hermetically sealed using direct fusion bonding of two Si substrates. Fusion bonding produces an interfacial oxide layer during the final annealing process. The presence of an interfacial oxide layer, before mating and bonding, has been studied to increase the bond quality between the two Si substrates.

Bond/seal integrity for different bonding methods has been extensively studied in the past. Acoustic microscope (AM) inspection is a commonly used non-destructive method where the device under test is inspected for unintended gaps or debonded regions between the areas of interest. During AM inspection, the device under test is placed on an AM stage, and the resolution and scan size of the ultrasonic transducer is adequately adjusted in order to obtain a detailed image of the interface. The transducer, which was placed over the device under test, is repositioned based on the image from the system in order to obtain a reference for comparison with the area of interest. Any cracks/voids in the interface are visible in the AM image. X-ray inspection is another method used to detect and characterize debonded regions in the bond-interface. It has been extensively used in the past on packages that were not sensitive to the radiation energy [43, 44]. In the X-ray inspection method, the known transmitted radiation is compared with the reflected or refracted radiation and the variations in radiation density are analyzed. The X-ray inspection method is similar to the ultrasonic inspection technique; the only difference being the former is through transmission unlike the latter that uses the reflection technique. Figure 2.15 shows an example of X-Ray inspection image of voids in solder joints. Fourier transform infrared inspection (FTIR) is another non-destructive method of inspecting the seal-integrity of a particular bond area. This technique can be used to detect the presence of gaseous molecules inside a cavity. The reduction or absence of the characteristic FTIR peak would translate to a leak in the cavity. The major advantage of this technique is that it can be used on a singular die stack as well. However, time consumption (if not automated) is a major disadvantage of this technique. In addition, the capping substrate should allow the reflected IR rays from the cavity back

into the measurement system. Hence, this technique cannot be used if the capping substrate strongly absorbs that particular wavelength of light.

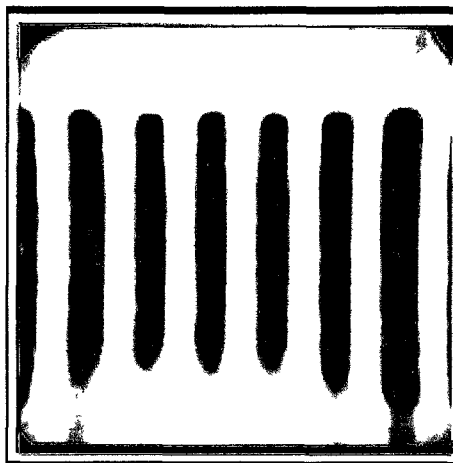


Figure 2.15. X-Ray Inspection image of voids in tape automated bonding solder joints [44].

Apart from imaging techniques, embedding of integrated sensors into vacuum cavities is a proven and widely used method of dynamically measuring the vacuum pressure inside the cavities of interest. Sensors integrated into the package can determine levels of hermeticity. Some examples of integrated sensors used for this purposes are pirani gauge, resonators, spark gap sensors, inter-digitated comb drives. A Pirani gauge works on the principle of thermal conductivity of certain materials. The difference in cavity pressure changes the thermal conductive properties of the materials employed in pirani gauges. The quality factor/damping coefficient of resonators is dependent on the ambient pressure conditions. Therefore, determination of the Q-factor of resonators reveals the vacuum pressure inside the cavities. Performances of resonators, one in a control chamber and the other in the cavity of a device under test, can be compared in order to accurately determine the internal cavity pressure of a device under test. Change

in internal pressure would result in a change in the magnitude of the dielectric breakdown of spark gaps, which in turn could be used to dynamically monitor internal cavity vacuum pressures. One of the major disadvantages of using the aforementioned devices in hermetic packages is the extensive and costly fabrication process associated with the already existing device fabrication process to integrate test-sensors with the devices under test.

Though measurement of internal cavity vacuum pressure is important, sometimes the detection of hermetic package leakage would suffice. The most commonly used method of detecting a leak in cavities under study is by using a tracer gas. The tracer gas method is usually carried out by forcing a particular gas (with known properties) into the volume of the package, known as bombing. The evolution of the tracer gas is detected and the leak rate is measured. In this way the leak-rate of a particular hermetic package can be calculated. Helium (He), known for its inert nature and small molecular size, is a commonly used tracer gas. The rate of diffusion of the gas out of the hermetic package is known to be proportional to the difference in the package and ambient pressure. One of the major limitations of the tracer gas bombing method is the integrity of the seal to hold the bombed He pressure. Another challenge faced is the detection of leaked He from the small sizes of MEMS packages. The minimum detectable volume of He depends on the measurement technique and instrumentation. R.C Kullberg and D.J Rossiter employed a micro-residual gas analyzer (micro-RGA) with a relatively new, time-of-flight technique to measure leaked tracer gas-concentration [45]. In this technique, the package containing the bombed tracer gas is ruptured in a spectrometer chamber, and real-time analyses are performed on the released tracer gas. This method solves the special problem of MEMS

devices with very small-enclosed cavity sizes with infinitesimal leak rates, by releasing the encapsulated tracer gas through cavity-rupture.

Optical lid-deflection is an inexpensive and accurate method of detecting and calculating the internal package vacuum pressure with respect to the ambient pressure. Here a lid is fabricated on top of the package cavity. According to this method, the lid is thin enough to deform due to the difference in the atmospheric pressure applied to the exterior and the internal cavity pressure. The deflection of the lid can be observed under a microscope or using an optical interferometer. Initial calibration of the lid deflection is carried out where the deflection magnitude of the lid for corresponding change in pressure load is measured. Typically packages under the lid are bombed with a tracer gas that would cause the lid to deflect. In this operation, the devices under test are placed in a basket, which is placed in a pressure chamber. The chamber pressure is then raised to a target pressure (typically 2-10 Bar) and is held for a specific time period (typically 2-10 hr). After a nitrogen purge of the chamber, the devices with the lid are transferred to an optical interferometer. Once the initial deflection magnitude of the lid is recorded, the leakage of the tracer gas that causes a change in the deflection magnitude of the lid is observed and recorded.

A typical package-bombing technique delivers a throughput of 20-200 parts per cycle. If vacuum pressures in packages are observed by the deflection of the lid (in the opposite direction as compared to the previous package-bombing case) then the permeation of ambient air into the vacuum cavities would be evident by the change in deflection magnitude of the lid. The dwell time between bombing and leak testing may vary. Mil-Std 883 standard recommends a dwell time less than 60 min. Consideration of

the dwell time of the devices under test is imperative for accurate measurements. The typical optical lid deflection technique leak detection system consists of only one bombing station and one leak detection chamber. Gross and fine leaks are detected using a single chamber. Accuracy is an issue when it comes to a very low difference between the ambient and package pressure. Increasing the aspect ratio of the optical lid can change its sensitivity. The lid employed in the optical lid deflection may be fabricated in many forms, like diaphragms, suspended plates, etc. A circular diaphragm was used in this study. The circular diaphragm lid was fabricated onto a capping wafer. Aligning the pressure diaphragm on the capping wafer over the cavities in the substrate wafer and bonding the stack in vacuum achieved diaphragm lids positioned exactly over the vacuum cavities. Difference in the ambient atmospheric pressure and the internal package pressure resulted in the deflection of the diaphragm lid.

Devices like resonators and gyroscopes depend on hermeticity of the enclosure package for sustained performance and functionality. Integrity of the hermeticity is determined by measuring the packaged device at separate times. Shift in the output can be attributed to the rate of degradation of the hermeticity of the package. The optical lid deflection method is preferred over other techniques in MEMS devices. G. Elger, et al. detailed the rule-of-thumb applied in determining if a particular MEMS package design supports optical lid deflection testing [46], as shown in Equation (2.7).

$$A \leq \frac{R^4}{ET^3} \quad (2.7)$$

$R$  is the minimum free width of the lid,  $E$  is the modulus of elasticity,  $T$  is the thickness of the lid, and  $A=3.9 \times 10^{-4}$  cc/N. Figure 2.16 shows the experimental setup by G. Elger, et al.

to measure the deflection magnitude of the optical lid under pressure load from the devices under test.

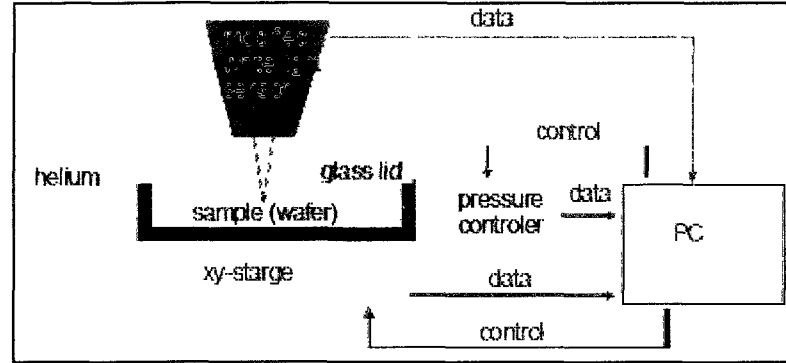


Figure 2.16. Illustration of the experimental setup for measuring the deflection magnitude of the diaphragm (glass lid) under a pressure load, on an optical leak detector [46].

An example of an optimized thickness for a silicon lid with  $R=1000 \mu\text{m}$  and  $E=1.5 \times 10^7 \text{ N/cm}^2$  would be  $26 \mu\text{m}$ . While designing the lid for fabrication, consideration should be given to the maximum pressure the lid would be exposed to. Leak-rate sensitivity  $L$  can be calculated using Equation (2.8).

$$L = \left( \frac{V_0}{k_2 t} \right) \ln \left( \frac{P_0 L_0}{P_0 L_0} \right) \quad (2.8)$$

$L$  is the leak rate sensitivity of the test in atm-cc/s,  $V_0$  is the volume of package in cc,  $k_2$  is the leak test gas constant,  $t$  is the test duration in seconds,  $D_{y,t}$  is the measured deformation of the package lid in cm,  $P_0$  is the chamber pressure during the test in  $\text{N/cm}^2$ , and  $L_0$  is the lid stiffness constant calculated from the package dimensions in  $\text{N/cm}$ . The stiffness constant,  $L_0$ , can be calculated from Equation (2.9).

$$L_0 = \alpha \frac{b^4}{ET^3} \quad (2.9)$$

$\alpha$  is the aspect ratio constant, and  $b$  is the lid width in cm. The aspect ratio constant depends on the design parameters of the deflecting media, which in this case is a circular

diaphragm. Typically, optical lids (to be used on devices under test) are coupled with calibration devices with known volumes and seal integrity and are tested for deflection by pressurizing and/or evacuating the packages while measuring the deflection of the diaphragm using an optical interferometer. This calibration is done in order to calculate the stiffness values of the optical lid design. The design parameters for the optical lid diaphragm should be chosen in such a way that the diaphragm deflect sufficiently to enable optical measurements. When a bombing step is involved, the diaphragm should be able to withstand the bombing pressure in addition to the target package vacuum pressure on devices under test.

## 2.4 Lead Zirconate Titanate

Lead zirconate titanate  $\text{Pb}(\text{Zr},\text{Ti})\text{O}_3$  is a perovskite piezoelectric ceramic that consists of a face-centered and body-centered crystal lattice structure. Commonly known as PZT, it has been widely used in the micromanufacturing of MEMS devices, like resonators and actuators, utilizing its piezoelectric properties of generating current when mechanically deformed or vice-versa. A high piezoelectric coefficient is one of the advantages of this piezoceramic over other existing piezoelectric materials. Figure 2.17 shows the crystal lattice structure of PZT. The two commonly used methods to create composites of PZT and Si are either by fabricating thin-film PZT onto crystalline Si or by bonding PZT ceramics to a Si substrate. Various other methods of depositing PZT are sputtering, chemical vapor deposition, and sol-gel deposition of thin film PZT. Sol-gel deposition technique involves the preparation of a sol-gel solution of PZT [48] and either spin coating or dip coating of the PZT sol-gel solution onto a substrate. This is followed by a series of high-temperature annealing processes that is required to obtain good

crystallinity and high piezoelectricity. On the other hand, bulk PZT ceramics have been anodically bonded to Si substrates using an intermediate glass layer [49]. This technique takes advantage of the excellent piezoelectricity of bulk PZT. However, low-temperature bonding methods had to be developed in order to stay within the curie point of PZT. Curie point is the critical temperature beyond which a PZT ceramic loses its piezoelectric properties. Poling is a technique employed to revive the piezoelectric properties of PZT ceramics. Applying a potential difference across the ceramic in order to re-orient the perovskite crystal structure of PZT achieves poling. Typical sol-gel deposited PZT layer-thickness range from 1-5  $\mu\text{m}$ . A unimorph design consists of PZT sandwiched between two metal layers that serve as electrodes for the piezoceramic layer.

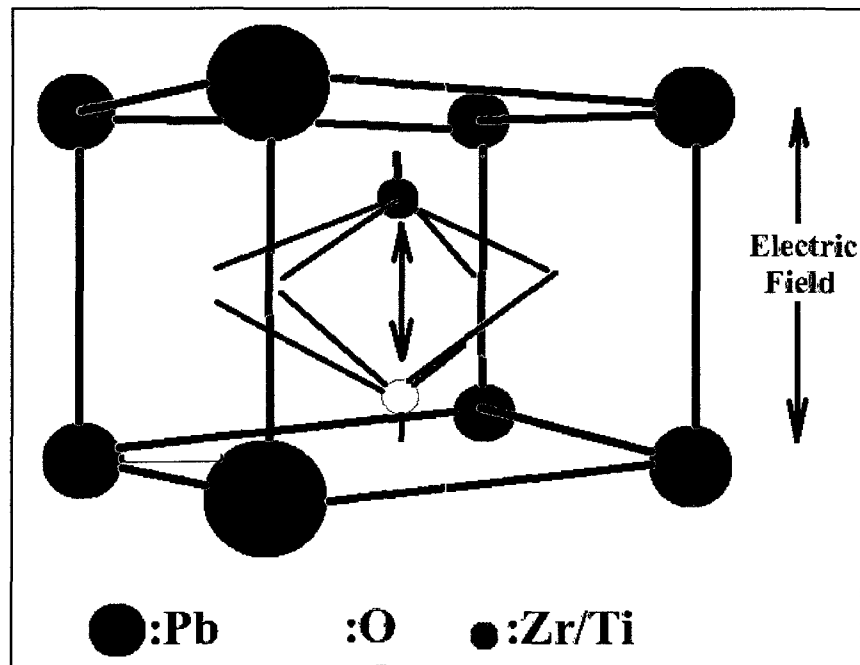


Figure 2.17. Illustration of the crystal lattice structure of PZT showing face-centered and body-centered arrangements of atoms.

## 2.5 References

- [1] S. S. Iyer and A. J. Auberton-Herve, *Silicon Wafer Bonding Technology for VLSI and MEMS applications*: INSPEC, The Institute of Electrical Engineers, London, United Kingdom, 2002.
- [2] A. Berthold, B. Jakoby, and M. J. Vellekoop, "Wafer-to-wafer fusion bonding of oxidized silicon to silicon at low temperatures," *Sensors and Actuators, A: Physical*, vol. 68, pp. 410-413, 1998.
- [3] K. Klier and A. C. Zettlemoyer, "Water at interfaces: Molecular structure and dynamics," *Journal of Colloidal and Interface Science*, pp. 216-299, 1977.
- [4] X. X. Zhang and J.-P. Raskin, "Low-temperature wafer bonding: A study of void formation and influence on bonding strength," *Journal of Microelectromechanical Systems*, vol. 14, pp. 368-382, 2005.
- [5] T. Suni, K. Henttinen, I. Suni, and J. Makinen, "Effects of plasma activation on hydrophilic bonding of Si and SiO<sub>2</sub>," *Journal of the Electrochemical Society*, vol. 149, pp. 348-351, 2002.
- [6] V. Dragoi, S. Farrens, and P. Lindner, "Plasma activated wafer bonding for MEMS," in *Proc. SPIE-The International Society for Optical Engineering*, vol. 5836, 2005, pp. 179-187.
- [7] M. M. R. Howlader, S. Suehara, H. Takagi, T. H. Kim, R. Maeda, and T. Suga, "Room-temperature microfluidics packaging using sequential plasma activation process," *IEEE Transactions on Advanced Packaging*, vol. 29, pp. 448-456, 2006.
- [8] R. E. Belford and S. Sood, "Surface activation using remote plasma for hydrophilic bonding at elevated temperature," *Electrochemical and Solid-State Letters*, vol. 10, pp. 145-148, 2007.
- [9] Y. Cho and N. W. Cheung, "Low temperature Si direct bonding by plasma activation," in *Proc. Materials Research Society Symposium*, vol. 657, 2001, pp. EE921-EE926.
- [10] W. B. Yu, C. M. Tan, J. Wei, S. S. Deng, and M. L. Nai, "Influence of Plasma Treatment and Cleaning on Vacuum Wafer Bonding," in *Proc. Electronics Packaging Technology Conference*, 2003, pp. 294-297.
- [11] T. Suga, T. H. Kim, and M. M. R. Howlader, "Combined process for wafer direct bonding by means of the surface activation method," in *Proc. Electronic Components and Technology Conference*, vol. 1, 2004, pp. 484-490.

- [12] C. Himcinschi, M. Friedrich, K. Hiller, T. Gessner, and D. R. T. Zahn, "Infrared spectroscopic investigations of the buried interface in silicon bonded wafers," *Semiconductor Science and Technology*, vol. 19, pp. 579-585, 2004.
- [13] G. Horn, T. J. Mackin, and J. Lesniak, "Trapped particle detection in bonded semiconductors using gray-field photoelastic imaging," *Experimental Mechanics*, vol. 45, pp. 457-466, 2005.
- [14] C. Ligu, C. Tao, and S. Lining, "Measurement method of bond Strength for silicon direct wafer bonding," in *Proc. IEEE International Conference on Information Acquisition*, 2006, pp. 1021-1025.
- [15] K. Tanaka, T. Konishi, M. Ide, and S. Sugiyama, "Wafer bonding of lead zirconate titanate to Si using an intermediate gold layer for microdevice application," *Journal of Micromechanics and Microengineering*, vol. 16, pp. 815-820, 2006.
- [16] C. Himcinschi, M. Friedrich, K. Hiller, T. Gessner, and D. R. T. Zahn, "Infrared spectroscopic investigations of the buried interface in silicon bonded wafers," *Semiconductor Science and Technology*, vol. 19, pp. 579-585, 2004.
- [17] C. Himcinschi, A. Milekhin, M. Friedrich, K. Hiller, M. Wiemer, T. Gessner, S. Schulze, and D. R. T. Zahn, "Growth of buried silicon oxide in Si-Si bonded wafers upon annealing," *Journal of Applied Physics*, vol. 89, pp. 1992-1994, 2001.
- [18] C. T. Kirk, "Quantitative analysis of the effect of disorder-induced mode coupling on infrared absorption in silica," *Physical Review B*, vol. 38, pp. 1255-1273, 1988.
- [19] K. T. Queeney, M. K. Weldon, J. P. Chang, Y. J. Chabal, A. B. Gurevich, J. Sapjeta, and R. L. Opila, "Infrared spectroscopic analysis of the Si/SiO<sub>2</sub> interface structure of thermally oxidized silicon," *Journal of Applied Physics*, vol. 87, pp. 1322-1330, 2000.
- [20] M. K. Weldon, V. E. Marsico, Y. J. Chabal, A. Agarwal, D. J. Eaglesham, J. Sapjeta, W. L. Brown, D. C. Jacobson, Y. Caudano, S. B. Christman, and E. E. Chaban, "On the mechanism of the hydrogen-induced exfoliation of silicon," *Journal of Vacuum Science and Technology B: Microelectronics and Nanometer Structures*, vol. 15, pp. 1065-1073, 1997.
- [21] D. Feijo, Y. J. Chabal, and S. B. Christman, "Silicon wafer bonding studied by infrared absorption spectroscopy," *Applied Physics Letters*, vol. 65, pp. 2548-2550, 1994.

- [22] D. Feijoo, Y. J. Chabal, and S. B. Christman, "Silicon wafer bonding studied by infrared absorption spectroscopy," *Applied Physics Letters*, vol. 65, pp. 2548-2548, 1994.
- [23] A. Milekhin, "Infrared study of Si surfaces and buried interfaces," *Journal of Vacuum Science and Technology B: Microelectronics and Nanometer Structures*, vol. 17, pp. 1733-1737, 1999.
- [24] U. Gosele, Y. Bluhm, G. Kastner, P. Kopperschmidt, G. Krauter, R. Scholz, A. Schumacher, S. Senz, Q. Y. Tong, L. J. Huang, Y. L. Chao, and T. H. Lee, "Fundamental issues in wafer bonding," *Journal of Vacuum Science and Technology A: Vacuum, Surfaces and Films*, vol. 17, pp. 1145-1152, 1999.
- [25] S. Hashimoto, T. Tsuda, K. Ogata, T. Sugahara, Y. Inoue, and K. Ohgaki, "Thermodynamic Properties of Hydrogen + Tetra-n-Butyl Ammonium Bromide Semi-Clathrate Hydrate," *Journal of Thermodynamics*, vol. 2010, pp. 1-5, 2010.
- [26] C. Peng, M. Stavola, W. B. Fowler, and M. Lockwood, "Ortho-para transition of interstitial H<sub>2</sub> and D<sub>2</sub> in Si," *Physical Review B*, vol. 80, p. 125207, 2009.
- [27] H. Itoh, Y. Ohmori, and M. Nakahara, "Chemical change from diffused hydrogen gas to hydroxyl ion in silica glass optical fibres," *Electronics Letters*, vol. 20, pp. 140-142, 1984.
- [28] R. Stengl, T. Tan, and U. Gosele, "Model for the silicon wafer bonding process," *Japanese Journal of Applied Physics, Part 1: Regular Papers and Short Notes and Review Papers*, vol. 28, pp. 1735-1741, 1989.
- [29] J. H. Anderson Jr. and K. A. Wickersheim, "Near infrared characterization of water and hydroxyl groups on silica surfaces," *Surface Science*, vol. 2, pp. 252-260, 1964.
- [30] W. K. Thompson, "Infra-red spectroscopic studies of aqueous systems. Part 1-Molar extinction coefficients of water, deuterium oxide, deuterium hydrogen oxide, aqueous sodium chloride and carbon disulphide," *Transactions of the Faraday Society*, vol. 61, pp. 2635-2640, 1965.
- [31] K. Klier and A. C. Zettlemoyer, "Water at interfaces: Molecular structure and dynamics," *Journal of Colloidal and Interface Science*, pp. 216-299, 1977.
- [32] C. Bergaud, L. Nicu, and A. Martinez, "Multi-mode air damping analysis of composite cantilever beams," *Japanese Journal of Applied Physics, Part 1: Regular Papers and Short Notes and Review Papers*, vol. 38, pp. 6521-6525, 1999.

- [33] F. Lochon, I. Dufour, D. Rebiere, U. Sampath, S. M. Heinrich, and F. Josse, "Effect of viscoelasticity on quality factor of microcantilever chemical sensors: Optimal coating thickness for minimum limit of detection," in *Proc. IEEE Sensors*, 2005, pp. 265-268.
- [34] L. D. Landau and E. M. Lifshitz, "Fluid mechanics", *Course of theoretical physics*, 2<sup>nd</sup> ed. Oxford, UK: RE&PPL, 1987, pp. 93-97.
- [35] R. K. Kapania, R. C. Singh, and C. Sultan, "Modeling Energy Harvesting from Membrane Vibrations in COMSOL," presented at the COMSOL Conference Boston, 2010.
- [36] A. Tai, H. Karagozoglu, and K. L. Chuan, "Organic sealant materials for quasi-hermetic sealing of MEMS sensor packages," in *Proc. 2006 Electronics Packaging Technology Conference*, vol. 8, 2006, pp. 462-471.
- [37] F. Y. Xu, "Quasi-hermetic photonic packages with polymer sealants in a central office environment," in *Proc. Electronic Components and Technology Conference*, vol. 53, 2003, pp. 1301-1307.
- [38] M. O. Alam, Y. C. Chan, and K. N. Tu, "Effect of reaction time and P content on mechanical strength of the interface formed between eutectic Sn-Ag solder and Au/electroless Ni(P)/Cu bond pad," *Journal of Applied Physics*, vol. 94, pp. 4108-4115, 2003.
- [39] K. Woonbae, W. Qian, J. Kyudong, H. Junsik, and M. Changyoul, "Application of Au-Sn eutectic bonding in hermetic RF MEMS wafer level packaging," in *Proc. International Symposium and Exhibition on Advanced Packaging Materials Processes, Properties and Interfaces*, vol. 9, 2004, pp. 215-219.
- [40] C. Sihai, C. Mingxiang, Y. Xinjian, Z. Honghai, and L. Sheng, "Research on wafer scale bonding method based on gold-tin eutectic solders [MEMS packaging]," in *Proc. International Conference on Electronic Packaging Technology*, 2003, pp. 187-189.
- [41] W. Y. Zhang, G. S. Ferguson, and S. T. Lucic, "Room temperature wafer bonding by elastomeric polymer-supported cold welding," in *Proc. 2003 International Semiconductor Device Research Symposium*, 2003, pp. 287-288.
- [42] W. Y. Zhang, G. S. Ferguson, and S. T. Lucic, "Elastomer-supported cold welding for room temperature wafer-level bonding," in *Proc. 17<sup>th</sup> IEEE International Conference on Micro Electro Mechanical Systems*, 2004, pp. 741-744.

- [43] F. W. Maur, "Detecting and Analyzing Wafer Bump Voids with X-Ray Inspection," in *Proc. 6<sup>th</sup> International conference on Electronic Packaging Technology*, vol. 2005, 2005, pp. 1-3.
- [44] C. Neubauer, "Intelligent X-ray inspection for quality control of solder joints," Components, in *Proc. IEEE Transactions on Packaging and Manufacturing Technology, Part C*, vol. 20, 1997, pp. 111-120.
- [45] R. C. Kullberg and D. J. Rossiter, "Measuring mass flows in hermetically sealed MEMs MOEMs to ensure device reliability," in *Proc. The International Society for Optical Engineering*, vol. 6884, 2008.
- [46] G. Elger, L. Shiv, N. Nikac, F. Muller, R. Liebe, and M. Grigat, "Optical leak detection for wafer level hermeticity testing," in *Proc. IEEE/CPMT International Electronics Manufacturing Technology*, vol. 29, 2004, pp. 326-331.
- [47] I. B. Celik, U. Ghia, P. J. Roache, C. J. Freitas, H. Coleman, and P. E. Raad, "Procedure for estimation and reporting of uncertainty due to discretization in CFD applications," *Journal of Fluids Engineering, Transactions of the ASME*, vol. 130, pp. 0780011-0780014, 2008.
- [48] K. D. Budd, S. K. Dey, and D. A. Payne, "Sol-Gel Processing of PbTiO<sub>3</sub>, PbZrO<sub>3</sub>, PZT, and PLZT Thin Films," *Journal of Electrical Ceramics*, vol. 36, pp. 107-121, 1985.
- [49] K. Tanaka, E. Takata, and K. Ohwada, "Anodic bonding of lead zirconate titanate ceramics to silicon with intermediate glass layer," *Sensors and Actuators, A: Physical*, vol. 69, pp. 199-203, 1998.

## CHAPTER 3

### ANALYTICAL AND THEORETICAL MODELING

This chapter discusses the various theoretical and finite element models that were developed to study the deflection of a pressure diaphragm and its application as an optical deflection technique to monitor and measure vacuum pressure in packages. In addition to the analytical models that were designed to study the different parameters of microdevices, the finite element models of PZT microcantilevers developed here was used to optimize the design parameters of the PZT microcantilevers. The results gathered from these studies were later compared to experimental results and evaluated for consistency.

#### 3.1 Finite Element Modeling of Si Pressure Diaphragm

Since the optical lid deflection method employed a circular diaphragm, a cylinder with fixed radius and thickness was modeled. COMSOL Multiphysics™, hereafter referred to as Comsol, was employed to obtain finite element solutions for the maximum deflection of the diaphragm for varying ambient pressure magnitudes. Initially the diameter and thickness of the diaphragm was to be optimized. The criteria for determining an optimal diaphragm design were sensitiveness of the diaphragm. Diaphragm sensitivity was determined by the difference in the diaphragm deflection for the difference in ambient pressure magnitudes. The higher the difference in deflection for

corresponding changes in pressure, the greater the accuracy of the system to determine the internal cavity pressure. The sensitivity of the diaphragm was inversely proportional to its thickness. Hence, a thin diaphragm would be highly sensitive to change in cavity pressure. However, limitations of fabricating very thin diaphragms on a Si substrate using inductively coupled plasma (ICP) were taken into consideration. A  $50 \times 50 \mu\text{m}$  mesh was created using mapped mesh-type containing quadrilateral elements. The two dimensional mapped mesh elements were swept three dimensionally from the top face to the bottom face of the cylindrical diaphragm, creating  $50 \times 50 \times 10 \mu\text{m}$  mesh elements throughout the solid. Figure 3.1 shows the meshed diaphragm.

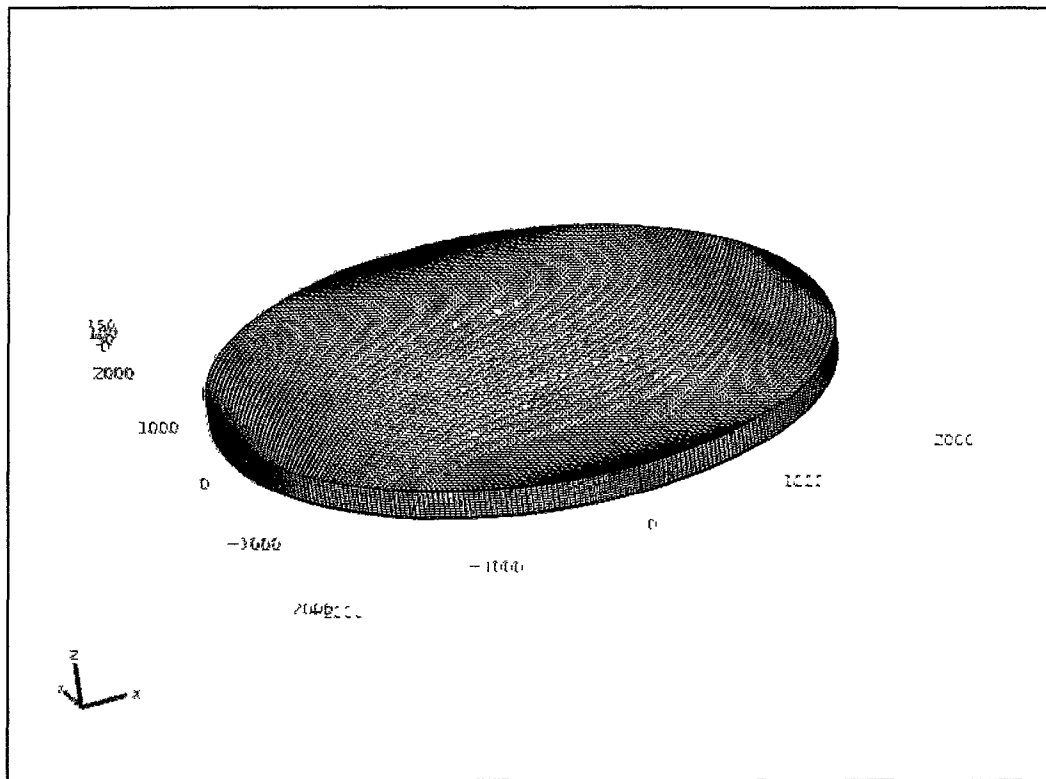


Figure 3.1. Meshed Si diaphragm model in Comsol that employed quadrilateral mesh type elements.

Solid mechanics physics was selected to solve the displacement of the diaphragm under applied load pressure. The boundary conditions used in solving the finite element model for displacement are given below:

- Linear elastic model was applied to the entire domain, which comprises the Si diaphragm. In terms of the displacement gradient, the total strain tensor is given in Equation (3.1).

$$\varepsilon = \frac{1}{2}(\nabla u + \nabla u^T) \quad (3.1)$$

$u$  is the displacement variable. The Duhamel-Hooke's law relates the stress tensor to the strain tensor by the following Equation (3.2).

$$s = s_0 + c: (\varepsilon - \varepsilon_0 - \alpha\theta) \quad (3.2)$$

$c$  is the fourth-order of the elastic tensor,  $s_0$  and  $\varepsilon_0$  are the initial stresses and strains respectively,  $\theta$  is the difference between temperature and reference temperature, and  $\alpha$  is the thermal expansion tensor.

- Three degrees of freedom were applied to the top and bottom surfaces of the diaphragm in the x, y, and z- axes.
- Fixed boundary condition applied to the sides of the cylindrical diaphragm,  $u(x)=u(y)=u(z)=0$ , where  $u$  is the displacement.
- Boundary load applied in the negative z-direction with varying pressure magnitudes.

Pressure magnitudes that simulate the internal cavity pressure of the vacuum cavities between Si wafers were varied from  $1 \times 10^{-4}$  mBar to 1 bar. The diaphragm diameter and thickness were varied in order to optimize the design specifications for the pressure diaphragm. It was concluded that an aspect ratio (ratio of diameter to thickness) of 80

would give satisfactory sensitivity to accurately measure the cavity pressure using the pressure diaphragm.

Using the results obtained from the design parameter optimization, a diaphragm with a 4000  $\mu\text{m}$  diameter and 50  $\mu\text{m}$  thickness was modeled and meshed using quadrilateral mesh type elements. Grid convergence technique was used to carry out mesh optimization [1]. Once the volume of a coarse mesh was obtained, the grid cell size,  $h$ , was calculated using Equation (3.3).

$$h = \left[ \frac{1}{N} \sum_{i=1}^N (\Delta V_i) \right]^{1/3} \quad (3.3)$$

$N$  was the number of elements on the surface of the diaphragm, and  $V$  was the volume of the element. Three different grid sizes for the same model were obtained through further finer meshing of the diaphragm. Solutions for each finer mesh were recorded. Let  $\phi_i$  be the displacement solutions obtained for corresponding finer grid sizes where  $h_1 < h_2 < h_3$  and so on. The criterion for choosing appropriate grid size for each consecutive mesh refinement was to keep the mesh refinement index at a desirable value of greater than 1.3. Mesh refinement index  $r$  was calculated using Equation (3.4).

$$r = \frac{h_{course}}{h_{fine}} \quad (3.4)$$

I.B Celik, et al. based the value of 1.3 on experience rather than a formal derivation [1].

Therefore,  $r$  was calculated for each set of mesh sizes as shown in Equation (3.5).

$$r_{21} = \frac{h_2}{h_1} \text{ and } r_{32} = \frac{h_3}{h_2} \quad (3.5)$$

The apparent order  $p$  was calculated using Equation (3.6).

$$p = \frac{1}{\ln(r_{21})} \left| \ln \left( \left| \frac{\epsilon_{32}}{\epsilon_{21}} \right| + q(p) \right) \right| \quad (3.6 \text{ a})$$

$$q(p) = \ln\left(\frac{r_{21}^p - s}{r_{32}^p - s}\right) \quad (3.6 \text{ b})$$

$$s = \text{sgn}(\varepsilon_{32}/\varepsilon_{21}) \quad (3.6 \text{ c})$$

$$\text{and } \varepsilon_{32}, \varepsilon_{21} = \phi_3 - \phi_2, \phi_2 - \phi_1 \quad (3.6 \text{ d})$$

Relative error  $e_a^{21}$  is approximately calculated using Equation (3.7).

$$e_a^{21} \approx \frac{(\phi_1 - \phi_2)}{(\phi_1)} \quad (3.7)$$

The fine-grid convergence index  $GCI_{fine}^{21}$  was calculated using Equation (3.8).

$$GCI_{fine}^{21} = \frac{1.25e_a^{21}}{r_{21}^p - 1} \quad (3.8)$$

An acceptable grid convergence index percentage was chosen as less than 2.2%. This technique was employed for the entire following finite element modeling mesh refinement techniques.

Once an optimized mesh size was determined ( $50 \times 50 \times 10 \mu\text{m}$ ), the Si diaphragm was loaded with pressure magnitudes ranging from  $1 \times 10^{-4}$  mBar to 1 Bar. Figure 3.2 shows the sample displacement solutions obtained for the Si pressure diaphragm for load pressures applied in the negative z-axis. As evident from the figure, maximum deflection was observed in the central region of the pressure diaphragm. Therefore, when measuring the diaphragm deflection experimentally, care should be taken to accurately perform surface profilometry along the central region of the diaphragm. Since these pressure diaphragms were etched into the Si wafer substrate using ICP, displacement solutions for varying pressure magnitudes were obtained for a range of diaphragm thicknesses in order to accurately predict the pressure magnitudes inside vacuum cavities, even though the ICP failed to uniformly etch the diaphragms resulting in varying diaphragm thicknesses.

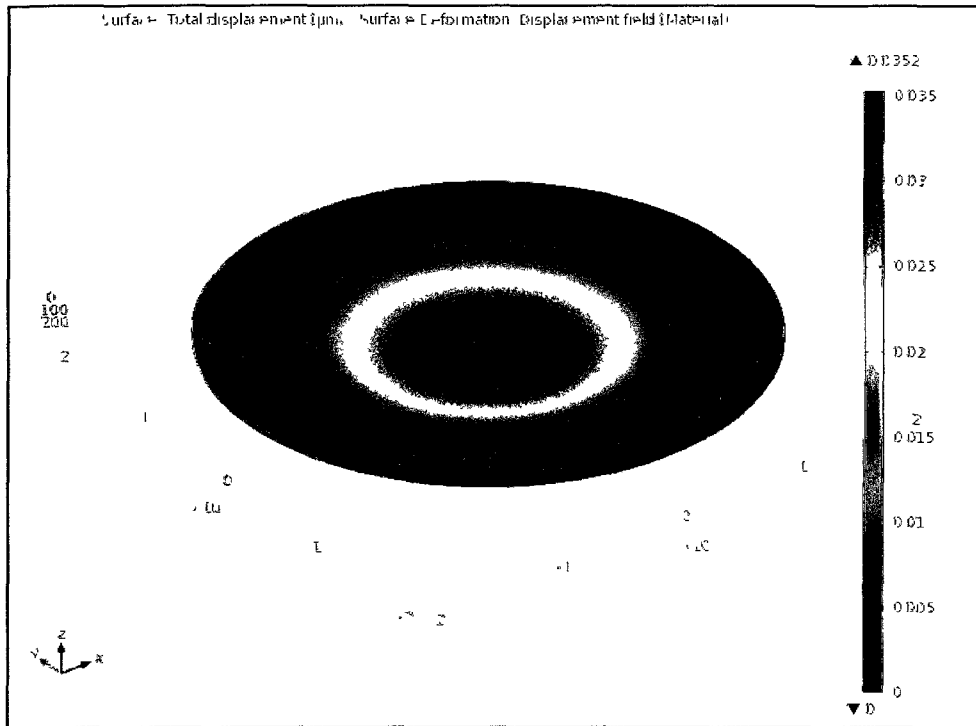


Figure 3.2. Finite element solutions for the displacement of the diaphragm for applied load pressure in the negative z-axis.

A parametric study was conducted using the finite element model to vary the diaphragm thickness and solve for diaphragm displacement for corresponding load pressure on the top surface. Hence, a library of maximum diaphragm deflection vs. diaphragm thickness for varying pressure magnitude was created. Figure 3.3 shows the results obtained from this parametric study. In order to evaluate the sensitivity of the diaphragm for different thicknesses, the difference between each consecutive diaphragm deflection magnitudes for corresponding loading pressure magnitudes were calculated. The average of the differences of the deflection magnitude was calculated and was plotted against the diaphragm thicknesses. Figure 3.4 shows the results obtained. From the plot, it was evident that diaphragms with the lowest thicknesses were highly sensitive to pressure changes. Therefore, the target diaphragm thickness that needed to be achieved

using ICP was kept at 50  $\mu\text{m}$ . If they were any lower, the diaphragms in the Si substrate would run the risk of being ruptured through over-etching.

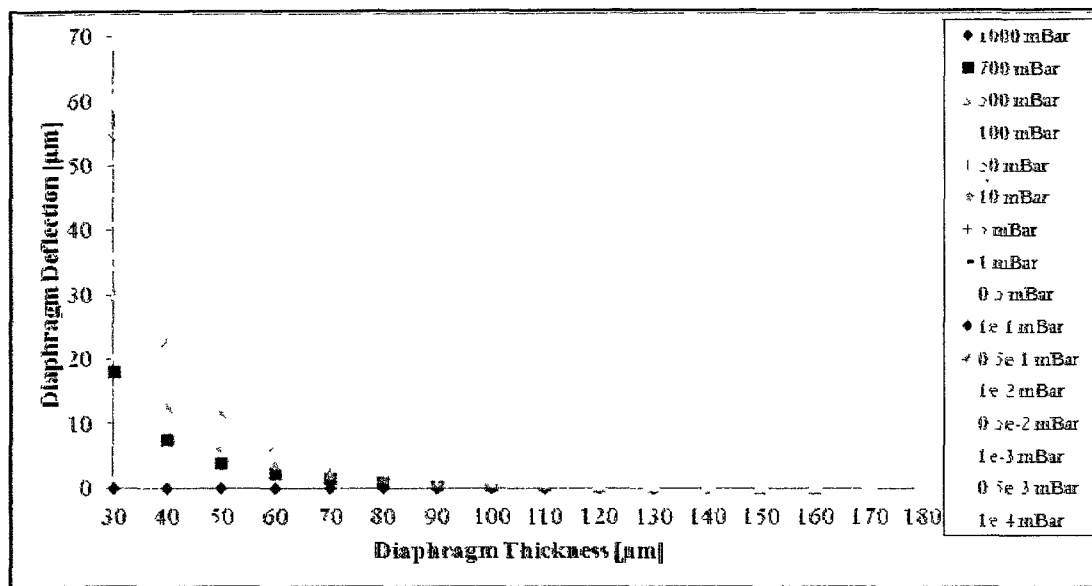


Figure 3.3. Plot showing the finite element diaphragm deflection solutions obtained for diaphragm with varying thicknesses and for various pressure magnitudes.

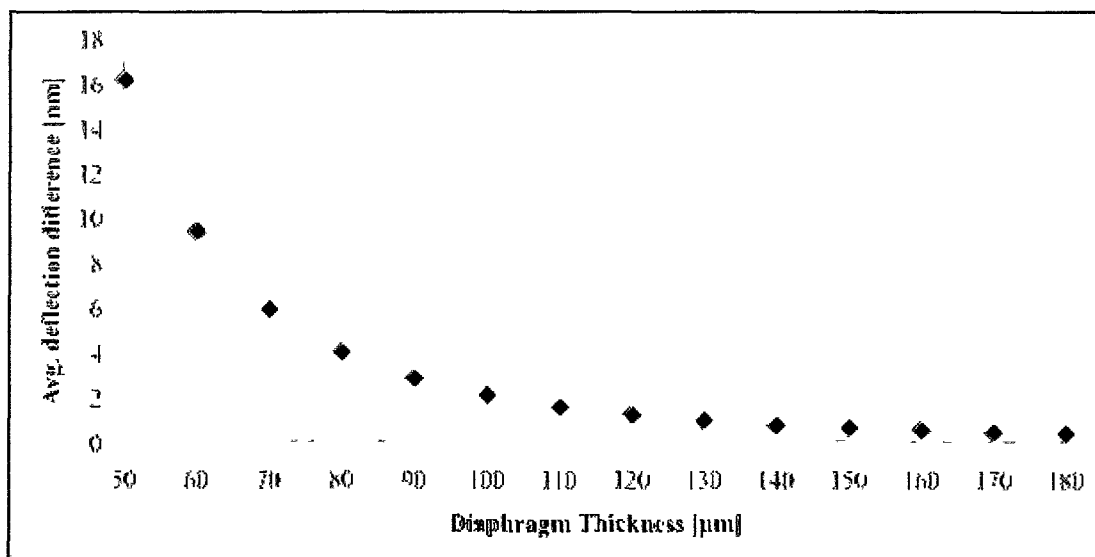


Figure 3.4. Plot showing the average difference in deflection of diaphragm for various pressure magnitudes against various diaphragm thicknesses.

### 3.2 Optimization of PZT Composite Beam

A PZT composite rectangular cantilever beam was constructed in Comsol in order to optimize beam design parameters, like length and width, in order to obtain a measurable resonant frequency and voltage. Plus, the beam must be thick and long enough on which to focus a large-sized (300  $\mu\text{m}$ ) laser spot (from laser vibrometer used for calculating resonant frequency amplitude). Figure 3.5 shows the different layers of the composite beam designed in Comsol. The layers illustrated in Figure 3.5 are of the following thicknesses: Pt = 0.125  $\mu\text{m}$ , PZT = 1  $\mu\text{m}$ , Ti = 0.025  $\mu\text{m}$ , SiO<sub>2</sub> = 1  $\mu\text{m}$ . Beam width and length were the parameters chosen for optimization, while keeping the total thickness of the beam fixed at 2.275  $\mu\text{m}$ .

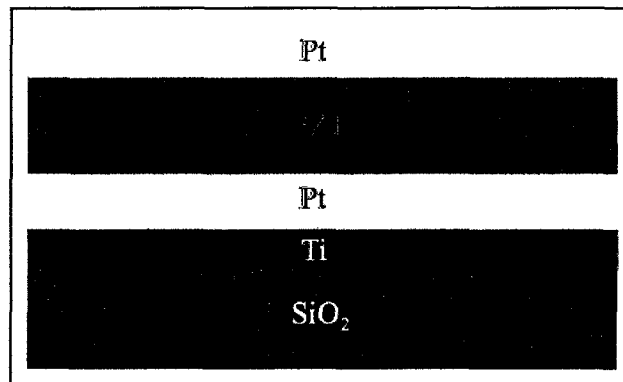


Figure 3.5. Illustration of the layers of the composite beam.

Initially, rectangular beam geometry was used to design each layer with the specified thicknesses. Solid mechanics physics was employed to linearly solve the model of a composite PZT beam for displacement. The boundary conditions used in solving the composite PZT beam are as follows:

- Fixed constraints applied to all faces at  $u(x)=0$ , which clamps one end of the beam to zero displacement in all three axes, i.e.  $u(x)=u(y)=u(z)=0$  where  $u$  is the displacement component.
- Bottom Pt layer was designated as the positive electrode, while the top Pt layer was designated as the ground electrode.
- Loading condition of input actuating voltage = 50 mV was applied to the top and bottom electrodes of the beam.
- The beam layers were assumed to have zero initial stress.

Static solver was used to simulate the maximum displacement produced for corresponding input actuating voltage. Quadrilateral mesh type was used for meshing the entire beam geometry. Mesh optimization was carried out using the grid convergence technique discussed in Section 3.1.

First, the beam length  $L_b$  was varied from 100-1000  $\mu\text{m}$  while keeping the beam width constant at  $W_b=350$   $\mu\text{m}$ . Static solutions for maximum beam-tip displacement was obtained and plotted against corresponding varying beam lengths. Figure 3.6 shows the results obtained for varying beam lengths and corresponding maximum tip-displacements. The plot shows a linear characteristic behavior, which is confirmed by the square of regression value  $R^2=1$ . Next the beam width  $W_b$  was varied from 50-500  $\mu\text{m}$  and corresponding maximum tip displacements were plotted, keeping the beam-length constant at  $L_b=1000$   $\mu\text{m}$ . Figure 3.7 shows the results obtained from this study. The square of regression value shows a near linear characteristic behavior of the maximum tip displacement for varying beam width. From Figures 3.6 and 3.7, it was concluded that beam length had a larger impact on tip displacement than beam width. Hence, an

optimized design of  $L_b=1000 \mu\text{m}$  and  $W_b=350 \mu\text{m}$  was obtained. This would give a maximum tip displacement of  $4.2 \mu\text{m}$  while the beam width was wide enough for the laser vibrometer laser.

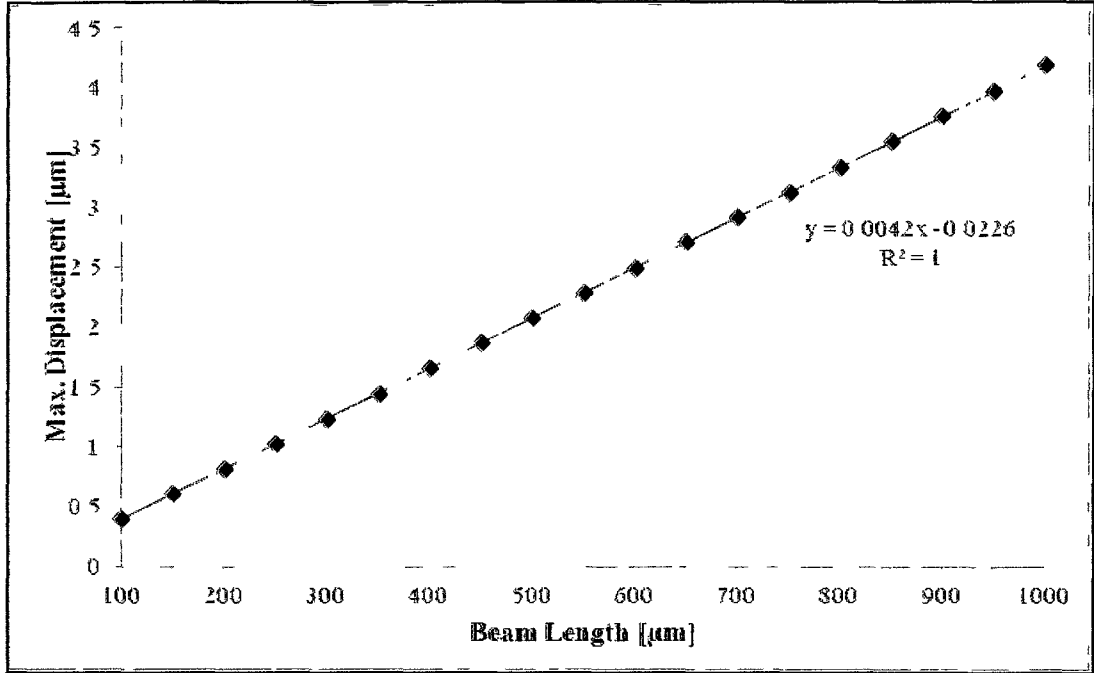


Figure 3.6. Plot showing the maximum tip displacement of the beam for varying beam length.  $W_b = 350 \mu\text{m}$ .

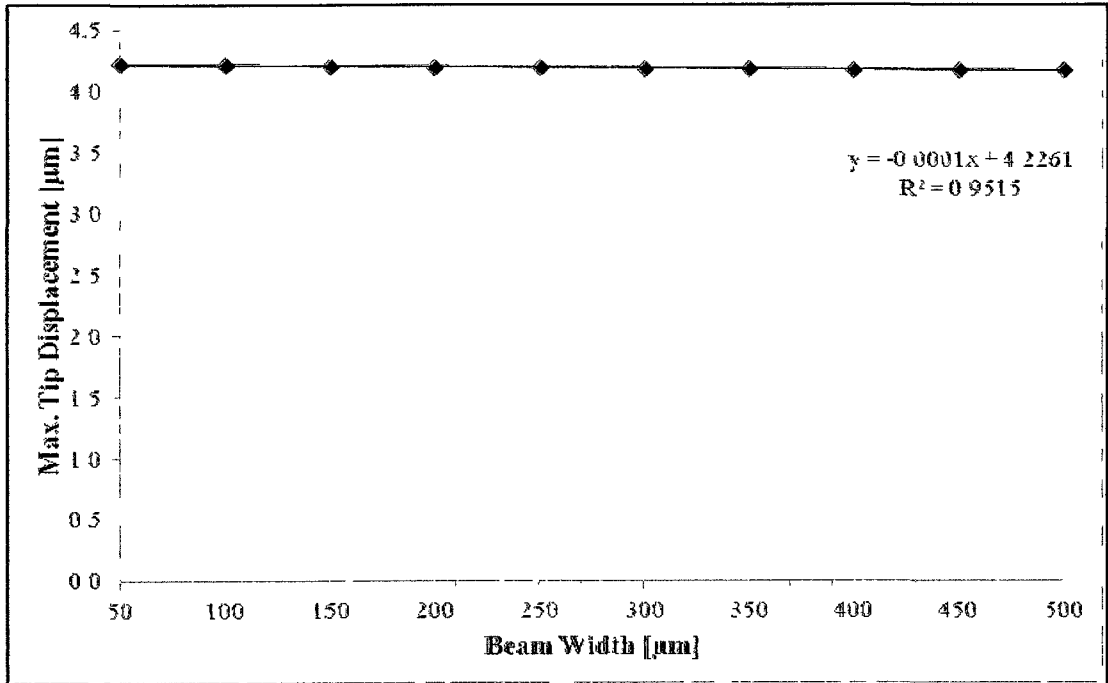


Figure 3.7. Plot showing the maximum tip displacement of the beam for varying beam width.  $L_b=1000 \mu\text{m}$ .

### 3.3 Analytical Modeling of PZT Composite Beam

An analytical model for the resonant frequency of the composite beam was obtained. The resonant frequency of an undamped beam with a uniform cross-section can be derived from the fundamental one-dimensional Euler-Bernoulli equation for transversal vibrations of a cantilever beam is shown in Equation (3.8).

$$\rho A = \frac{\partial^2 w}{\partial t^2} + EI \frac{\partial^4 w}{\partial x^4} = 0 \quad (3.8)$$

$w(x,t)$  is the time dependent transverse-displacement of the central line of the cantilever beam from the neutral position,  $EI$  is the beam bending stiffness,  $\rho$  is the beam density, and  $A$  is the area of cross-section [2]. The time dependent function,  $w(x,t)$ , can be separated independently into its position and time functions as shown in Equation (3.9).

$$w(x,t) = W(x)Y(t) \quad (3.9)$$

Substituting Equation (3.9) into (3.8) generates ordinary differential equation, as shown below.

$$\ddot{Y}(t) + \omega_n^2 Y(t) = 0 \quad (3.10)$$

$$\frac{\partial^4}{\partial x^4} W(x) + \omega_n^2 \left( \frac{\rho A}{EI} \right) W(x) = 0 \quad (3.11)$$

$\omega_n$  is the natural frequency of the beam. Equation (3.10) depicts the oscillation of an undamped harmonic oscillator with one degree of freedom. Solving Equation (3.11) gives the modal shapes of a vibrating cantilever beam. Equation (3.12) shows the solution obtained below.

$$W_n(x) = \cosh \frac{\lambda_n x}{L} - \cos \frac{\lambda_n x}{L} - C_n \left( \sinh \frac{\lambda_n x}{L} - \sin \frac{\lambda_n x}{L} \right) \quad (3.12)$$

$L$  is the beam length and  $C_n$  depicts the integration constants.  $\lambda_n$  is defined by Equation (3.13). Since the cantilever beam modeled in this study is clamped at one end while free at the other, applying the aforementioned boundary conditions from Equation (3.8-3.11) to Equation (3.12) yields the resonant frequency equation, shown in Equation (3.13).

$$\cos(\lambda_n L) \cosh(\lambda_n L) + 1 = 0 \quad (3.13)$$

The boundary conditions applied in Equation (3.12) determined the integration constants for different modal vibrations, as shown in Equation (3.14).

$$C_n = \frac{\sinh \lambda_n L - \sin \lambda_n L}{\cosh \lambda_n L + \cos \lambda_n L} \quad (3.14)$$

Quadratic solutions for Equation (3.14) were obtained, which yielded the roots of the equation  $\lambda_1 L = 1.875$ ,  $\lambda_2 L = 4.694$ , and  $\lambda_3 L = 7.855$ . These roots denoted the first three modes of vibration of an undamped beam. Hence, Equation (3.15) was derived that solves the resonant frequency of an undamped beam vibrating in mode 1.

$$f_1 = \frac{(1.875)^2}{2\pi L^2} \sqrt{\frac{EI}{\rho A}} \quad (3.15)$$

N. Hossaine, et al. derived the equation for resonant frequency of an undamped composite beam by substituting composite-beam bending stiffness and composite-beam density equations into Equation (3.15) [3]. The composite beam stiffness and density is given by Equation (3.16) and (3.17).

$$\overline{EI} = \sum_{i=1}^N E_i I_i \quad (3.16)$$

$$\overline{\rho} = \frac{\sum_{i=1}^N \rho_i t_i}{\sum_{i=1}^N t_i} \quad (3.17)$$

Hence, the resonant frequency for a composite beam was derived by substituting Equations (3.16) and (3.17) back into Equation (3.15) yielding Equation (3.18).

$$f_n = \frac{(\lambda_n)^2}{2\pi} \sqrt{\frac{\sum_{i=1}^N \overline{EI}_i}{\overline{\rho} A}} \quad (3.18)$$

The moment of inertia for individual layers is given by Equation (3.19).

$$I_i = \frac{bt_i^3}{12} + A_i d_i^2 \quad (3.19)$$

$b$  is the beam-width,  $t$  is the thickness of each layer,  $A$  is the cross-sectional area of each layer, and  $d$  is the distance between the beam centroidal axis and the individual layer neutral axis. From Equation (3.15) and the beam parameters optimized from the COMSOL model, the analytical resonant frequency was calculated to be 1060.15 Hz.

### 3.4 Theoretical Modeling of Composite Undamped PZT Beam

The model used in optimizing beam design parameters was used in this study. A 1000  $\mu\text{m}$  long and 350  $\mu\text{m}$  wide PZT composite beam, with the layers described in Section 3.2, was designed and solved using Eigen frequency analysis for the purpose of theoretically determining the resonant frequency for mode 1 vibration. The theoretically solved resonant frequency magnitude was found to be 1082 Hz, which was close to the

analytical modeling. The reason for the slight discrepancy in both the resonant frequencies was due to the fact that the Comsol model accurately models the beam more than the analytical model. Once the resonant frequency for mode 1 was obtained, a frequency sweep was performed, around the resonant frequency, on the model with an input actuating voltage of 50 mV. Figure 3.8 shows the results obtained from the frequency sweep analysis.

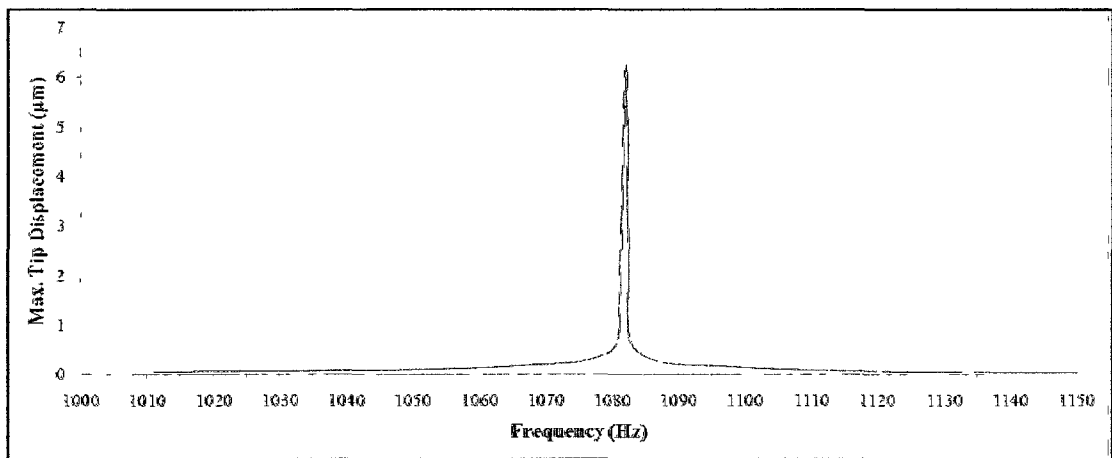


Figure 3.8. Frequency vs. maximum tip deflection magnitude of undamped PZT composite beam with an actuating voltage  $V_a=50$  mV.

### 3.5 Frequency Analyses of Damped Composite PZT Beam

The same model used in Section 3.4 was modeled for damped beam vibration. For the purpose of simulating the operation of the cantilever beam in air, 100  $\mu\text{m}$  thick air columns were modeled above and below the beam under study, as shown in Figure 3.9. The same boundary conditions employed in Section 3.4 were used here. Quadrilateral mesh type with linear elements was used. A separate mesh distribution was employed for each layer, due to the large difference in the thicknesses of the layers. After mesh refinement using the grid convergence technique, a final optimized  $50 \times 10 \times 0.05$   $\mu\text{m}$  mesh

was used for the PZT and SiO<sub>2</sub> layer. Mesh size of 50×10×0.0125 μm were used for the top and bottom 0.125 μm thick Pt electrodes, while a mesh size of 50×10×0.0025 μm were used for the 0.025 μm thick Ti layer. Since the air columns were 100 μm thick, mesh of sizes 50×10×1 μm were used. Multiple physics of solid mechanics with piezoelectric module was coupled with pressure acoustics module in this model. Some additional boundary conditions applied to this model were as follows:

- Acoustics pressure applied to the top and bottom surfaces of the composite cantilever beam.
- Acoustics pressure coupled as viscous damping in the piezoelectric module.

The model was solved for maximum tip displacement for varying ambient air pressure magnitudes using a frequency sweep from 1000-1150 Hz. The beam was solved for three pressure magnitudes- $1 \times 10^{-4}$  mBar, 0.5 mBar, and 1000 mBar. The purpose of this study was to simulate the change in the resonant frequency curve with change in ambient air pressure magnitudes, as shown in Figure 3.10. As evident from the figure, broadening of the resonance peak was observed as the ambient air pressure magnitude was increased. This is trivial as the Q-factor of the device reduces with increase in the air damping. Quality factor calculations for resonance curves for beams showed  $Q=10^6$  for  $10^{-4}$  mBar,  $Q=10^4$  for 0.5 mBar, and  $Q=40$  for 1000 mBar ambient pressure magnitudes. These results further signifies the need for vacuum-encapsulation of PZT microcantilever beams in order to fine-tune the resonance curve for specific applications, in addition to increasing the efficiency of the device by the increase in the Q-factor.

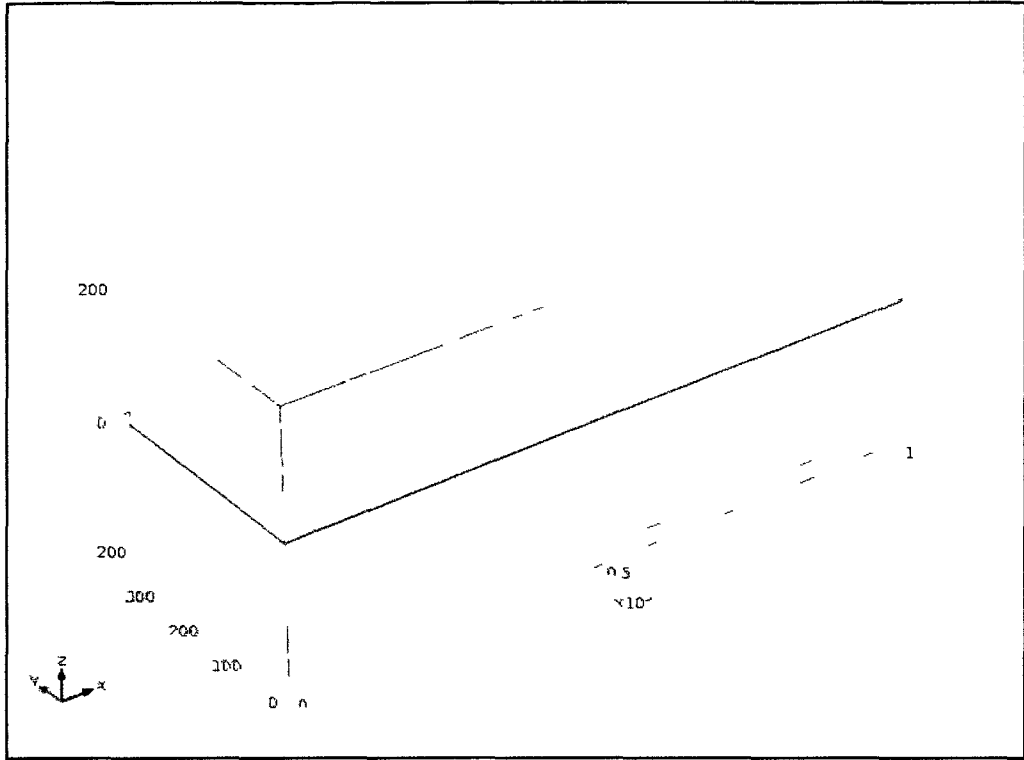


Figure 3.9. Modeled damped composite PZT beam with air-columns on the top and bottom surfaces of the cantilever beam.

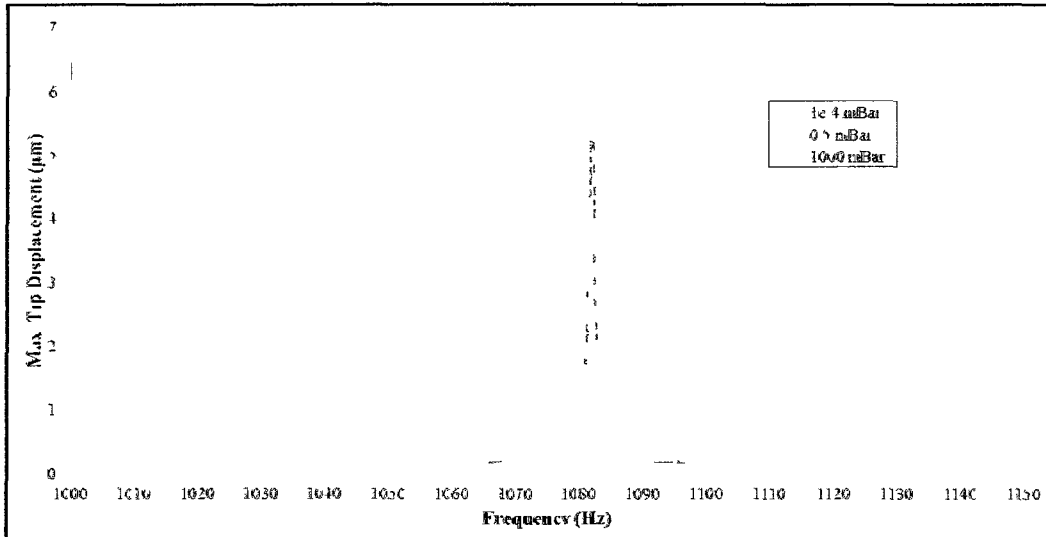


Figure 3.10. Plot showing the results obtained from damped PZT beam analyses.

### 3.6 References

- [1] I. B. Celik, U. Ghia, P. J. Roache, C. J. Freitas, H. Coleman, and P. E. Raad, "Procedure for estimation and reporting of uncertainty due to discretization in CFD applications," *Journal of Fluids Engineering, Transactions of the ASME*, vol. 130, pp. 0780011-0780014, 2008.
- [2] I. R. Voiculescu, M. E. Zaghoul, R. A. McGill, and J. F. Vignola, "Modelling and measurements of a composite microcantilever beam for chemical sensing applications," *Proceedings of the Institution of Mechanical Engineers, Part C: Journal of Mechanical Engineering Science*, vol. 220, pp. 1601-1608, 2006.
- [3] N. Hossain, J. W. Ju, B. Warneke, and K. S. J. Pister, "Characterization of the Young's modulus of CMOS thin films," *ASTM Special Technical Publication*, vol. 1413, pp. 139-151, 2001.

## CHAPTER 4

### EXPERIMENTAL PROCEDURES

This chapter discusses the experimental methods and test benches designed in the various stages of the research work.

#### 4.1 Direct Fusion-Bonding of Si/Si

Initially two p-type 100 mm diameter prime (100) Si wafers were taken and cleaned with acetone and isopropyl alcohol (IPA) in order to remove organic impurities. The wafers chosen had an average roughness of less than 2 nm and less than 30  $\mu\text{m}$  wafer bow. After a quick dump rinse (QDR) in de-ionized (DI) water, the wafers were spin rinse dried (SRD). The wafers were then treated with 5:1 buffered oxide etch (BOE) in order to remove any native oxide present on the wafer surfaces. Following QDR and SRD, the wafers were treated with standard cleaning procedures, like RCA 1 and RCA 2. RCA 1, consisting of 5:1:1 proportion of  $\text{H}_2\text{O}:\text{NH}_4\text{OH}:\text{H}_2\text{O}_2$ , was used in order to remove all organic impurities while RCA 2, consisting of 5:1:1 proportion of  $\text{H}_2\text{O}:\text{HCl}:\text{H}_2\text{O}_2$ , was used in order to remove all metallic impurities from the surface of the wafers. First the wafers were dipped into RCA 2 bath at 85°C for 10 min. After a QDR and SRD the wafers were dipped into RCA 1 bath at 85°C for 10 min. Finally, any remaining chemical residues were removed with QDR and SRD, and the wafers were ready to be pre-bonded.

A substrate bond aligner was employed to align the two wafers onto a fixture that kept the wafers in position and clamped with 100  $\mu\text{m}$  separation. Figure 4.1 shows a picture of two wafers mounted onto the fixture. The fixture was then manually placed into the substrate bonder. Once a target chamber vacuum pressure of  $2 \times 10^{-4}$  mBar was achieved, the wafers were brought into contact by the removal of the clamps and spacers. Bonding was carried out at 400  $^{\circ}\text{C}$  for 30 min. This step is generally referred to as pre-bonding. Following pre-bonding, the wafer stack was transferred into a furnace and thermally annealed at 1000  $^{\circ}\text{C}$  for 4 hr to permanently seal and bond the wafers. NIR and tensile tests were conducted on dies diced from the bonded wafer stack to qualitatively and quantitatively determine the bond integrity of the wafer-stack.

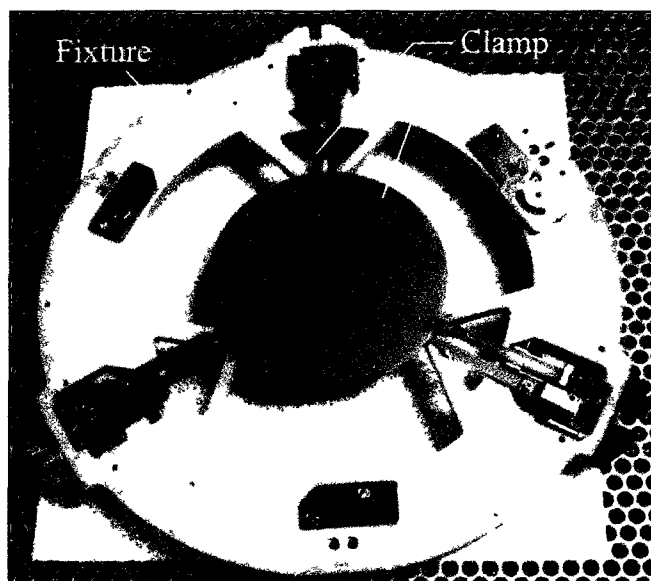


Figure 4.1. Picture of the wafer-stack clamped onto the fixture. Spacers are shown inserted between the wafers keeping the stack 100  $\mu\text{m}$  apart.

## 4.2 Plasma-Activated Wafer Bonding

Plasma-activation was carried out in a reactive ion etch (RIE) chamber. Figure 4.2 shows an illustration of the plasma-activation setup. Plasma-activation was carried out immediately following wet chemical activation of the surfaces using RCA 1 and 2. Wafers were plasma-activated using O<sub>2</sub> gas at a flow rate of 25 sccm and pressure of  $266 \times 10^{-3}$  mBar. Activation was carried out using an RF power of 100 W for 60 s. The plasma-activation recipe was optimized through trial and error. Activation time and plasma-power was found to have the most impact on the surface of the wafers. Too much power or time had detrimental effects on the surface of the wafers, such as increased surface roughness. After the dry surface activation, the wafers were aligned, clamped, and placed into the substrate bonder. Since the wafer surfaces were activated and were highly reactive, the pre-bonding recipe was modified. The bonding temperature was reduced from 400 °C to 85 °C for 2 hr. In addition, the final thermal annealing temperature was reduced from 1000 °C for 4 hr to 300 °C for 1 hr. For the purpose of measuring the bond strength between the wafers, dies from random locations of the diced wafer were chosen to be pull-tested. Individual dies were sandwiched between an aluminum stud and a ceramic backing tile. The aluminum stud and the ceramic tile were pre-coated with epoxies that were cured at 150 °C for 1 hr. A Sebastian V tensile test station was employed to pull test the die. One end of the aluminum stud was fixed to a clamp and pulled. A swivel ring let the aluminum stud through but held back the ceramic tile. This enabled the two dies to be pulled apart at right angles ensuring accurate tensile test results.

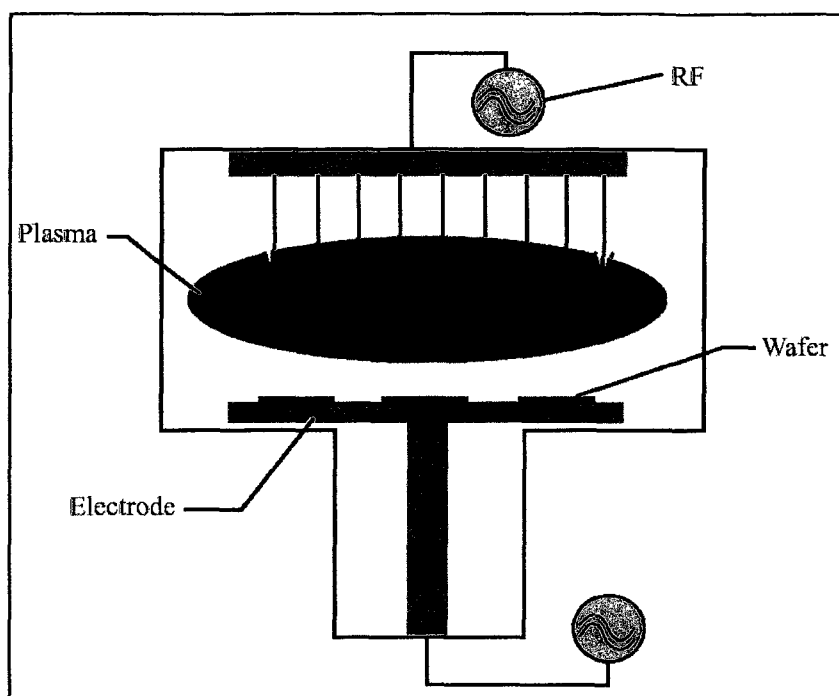


Figure 4.2. Illustration of plasma-activation of Si wafers in an RIE chamber.

### 4.3 Investigation on Interfacial Oxide Formation and Growth

Plasma-activated and fusion bonded wafers were diced in order to study the oxide layer at the interface of the wafer-stack. However, the diamond resin blade employed in the dicing operation creates heavy scratches and striations at the interface of the dies, which causes the inability to effectively observe and study the true interface. Figure 4.3 shows an SEM image of the interface of a diced die from a fusion-bonded wafer-stack. In order to observe the true surface, the edges of the die were immersed in 32 % wt/wt potassium hydroxide solution (KOH) at 80 °C for 30 min. This process etched a small portion of Si material from the interface, exposing the true interface in the process. The apparatus was setup in such a way so that only the edges of the dies were immersed in the KOH etchant and not the entire die, as illustrated in Figure 4.4. SEM images of the

interface of the etched die revealed the presence of an interfacial oxide layer. The role of the oxide layer at the interface was also investigated.

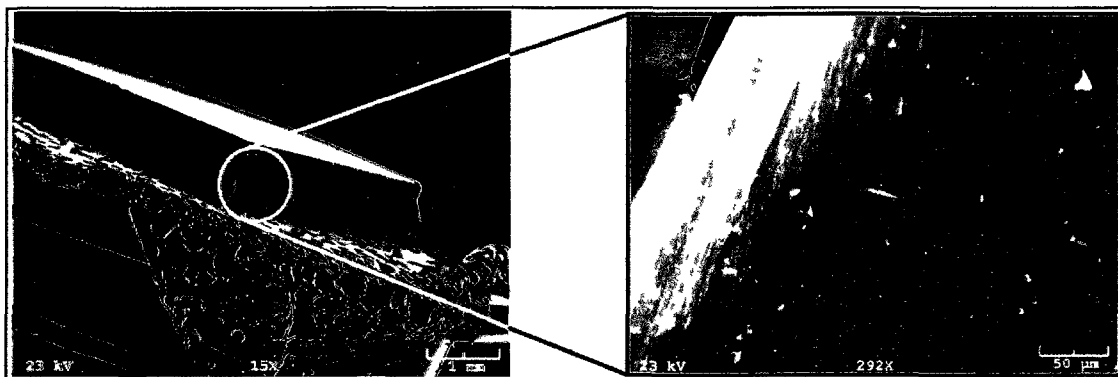


Figure 4.3. SEM micrograph of the interface of a cleaved die from a Si/Si wafer stack. Inset shows a close-up revealing the hairline interface.

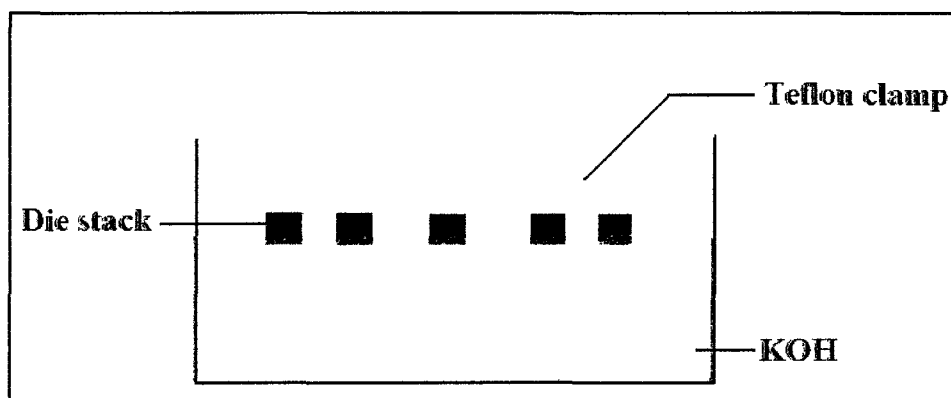


Figure 4.4. Illustration of KOH etching of die-stacks to obtain true interface for SEM imagery.

Plasma-activation is an interim process that is carried out in between RCA cleaning and wafer fusion bonding. It was therefore important to study the effects of storage time (time interval between plasma-activation and bonding) on the bond strength and bond quality of the wafers. Two (100) Si wafers (one single-side polished and another double-side polished) wafers were chosen and cleaned with acetone and

isopropyl alcohol. After QDR and SRD, the native oxides on the wafer surfaces were removed by BOE etching. After plasma-activation using RIE, the wafers were stored for various time intervals before being pre-bonded. Immediately following bonding, the wafers were inspected for bond-quality using NIR imagery, and were diced and measured for bond strength.

#### **4.4 Fabrication of Cavities and Pressure Diaphragms in Silicon**

Fabricating cavities in one Si wafer and capping them using another Si wafer in vacuum realized the vacuum encapsulation of cavities. Since the optical lid-deflection method of measuring cavity vacuum pressure was employed, high-aspect ratio pressure diaphragms were also fabricated and etched into the capping Si wafer. Three major studies were conducted with vacuum cavities between two Si wafers. The initial study conducted was the fabrication of vacuum cavities without any gettering material. Following this, a gettering intermediate layer and gettering rings were fabricated, and their application in maintaining the integrity of the vacuum seal and pressure were studied.

##### **4.4.1 Fabrication of Cavities in Si Substrate**

Initially a 100 mm diameter prime (100) Si wafer with 1  $\mu\text{m}$  thick  $\text{SiO}_2$  layer was chosen and cleaned with acetone and isopropyl alcohol in order to remove any organic impurities from the surface of the substrate. After QDR and SRD, the wafer was dehydrated at 250  $^{\circ}\text{C}$  for 5 min on a hot plate in order to remove any  $\text{H}_2\text{O}$  molecules, thus preparing the wafer for photolithography. A wafer spinner was used to spin-coat priming agent Hexamethyldisilazane (HMDS) onto the Si substrate using the recipe mentioned in Appendix B. A 4  $\mu\text{m}$  thick SPR220 positive photoresist (see Appendix A for details) was

then spin-coated onto the Si surface. The spin recipes for HMDS and photoresist are included in Appendix B. The entire fabrication process flow is illustrated in Figure 4.5.

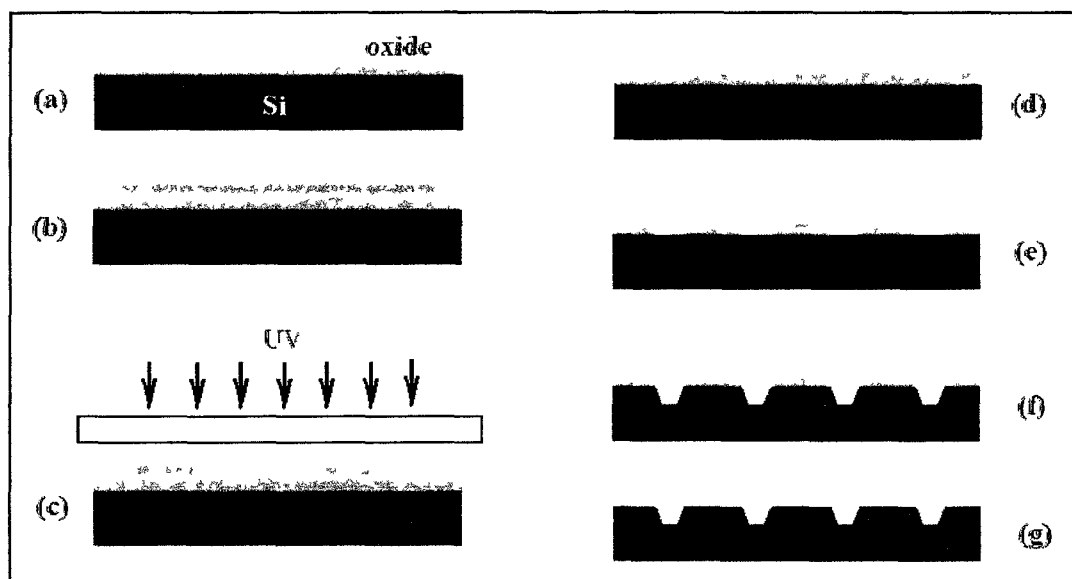


Figure 4.5. Illustration of the cavity fabrication process. (a) Si wafer with 1  $\mu\text{m}$  oxide, (b) Photoresist spin-coating, (c) Exposure to UV light, (d) Developing, (e) BOE etching of oxide, (f) KOH etching of Si, and (g) Oxide stripping.

In order to enhance photoresist adhesion, the wafer was soft-baked at 110  $^{\circ}\text{C}$  for 3.5 min on a hot plate. This was done by first heating the wafer to 90  $^{\circ}\text{C}$  and then 100  $^{\circ}\text{C}$ , each for 1.5 min. The slow ramping up to the desired soft-baking temperature was done in order to prevent cracking of the thermal shock-sensitive photoresist. Ramping down of the temperature was carried out by first transferring the wafer at 110  $^{\circ}\text{C}$  to 100  $^{\circ}\text{C}$  and then 90  $^{\circ}\text{C}$ , each for 1.5 min. Wafer was then exposed to ultra-violet (UV) radiation at 1000 W for 7 s. Figure 4.6 shows the mask used for patterning the cavities on the photoresist. Multiple exposures were employed during UV irradiation at three cycles with 10 min wait per cycle. This also was done to prevent any thermal shocking of the polymer. After exposure, the photoresist was developed in MF319 developer. Following

a QDR and SRD, the wafers were inspected for defects under a microscope. Finally, hard baking at 125 °C for 5 min hardened and bonded the patterned photoresist onto the wafer surface.

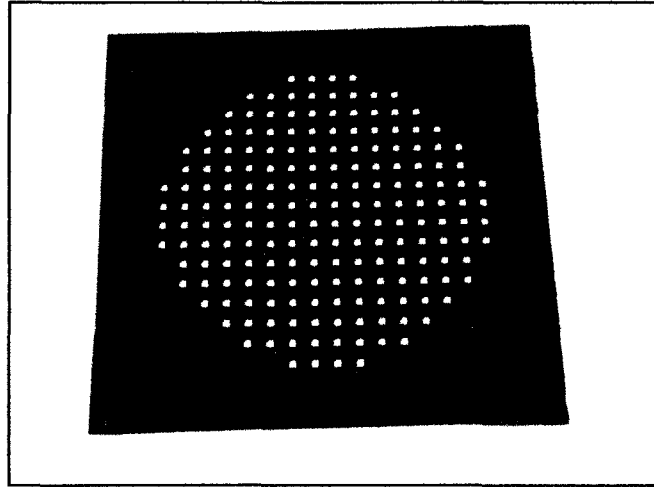


Figure 4.6. Picture of the dark-field mask used to pattern cavities into the Si wafer.

Following photolithography, the exposed oxide windows were etched through to the bare Si substrate in 5:1 BOE for 20 min. After stripping of the photoresist using acetone, the wafer was then rinsed in isopropyl alcohol and DI water. In order to obtain 60  $\mu\text{m}$  deep square cavities with trapezoidal cross-section, the Si wafer with the patterned oxide layer was immersed in KOH at 80 °C for 60 min. The oxide layer served as a hard mask during the Si etching. The oxide layer was finally stripped by immersing the wafer in BOE. This was followed by QDR and SRD. From this point on, the wafer with cavities is referred to as ‘cavity wafer’.

#### 4.4.2 Fabrication of Pressure Diaphragms in Si Wafer

The magnitudes of the deflection of the pressure diaphragms were measured by stylus tip profilometry. The opposite side of the wafer was also patterned with ‘trace

guides' so as to ensure that the stylus profilometer tip was scanned across the exact central region of the diaphragm. This ensured accurate measurement of the maximum deflection of the pressure diaphragm.

Initially a (100) double side polished 100 mm diameter Si wafer, with 300 nm of a thermally deposited Al layer on both sides, was chosen and cleaned with acetone and isopropyl alcohol. After a QDR and SRD in DI water, the wafers were dehydrated at 250 °C for 5 min. First, the trace guide patterns for the stylus profilometer were patterned on one side of the wafer. The entire fabrication process is illustrated in Figure 4.7. After spin-coating SPR220 onto the Al layer, the wafer was soft-baked at 110 °C with the temperature ramp-up process discussed earlier.

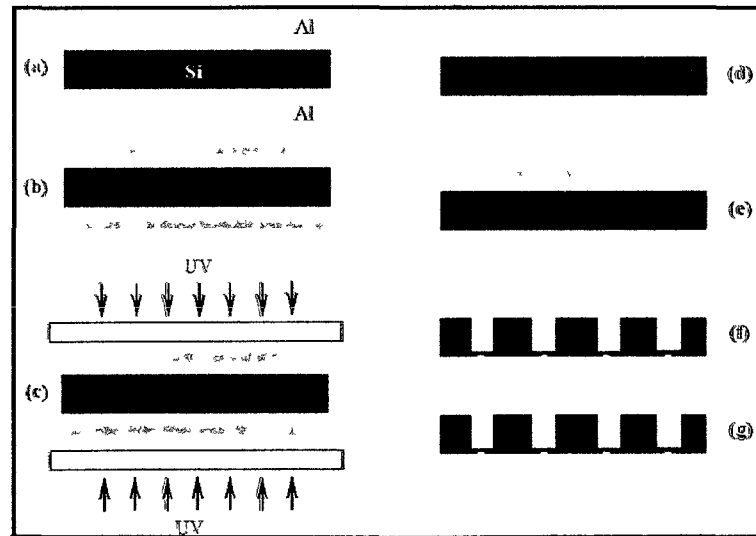


Figure 4.7. Illustration of the fabrication process-flow for the pressure diaphragms and trace-guides on Si substrate. (a) Si wafer with top and bottom Al layer, (b) Photoresist spin-coated on both sides, (c) UV irradiation, (d) Resist development, (e) Al etching, (f) ICP etching, and (g) Al stripping.

The photoresist was then exposed under UV light using the “trace guide” mask pattern shown in Figure 4.8, and then developed. Following the hardbaking of the

patterned and developed side, the other side of the wafer was also spin-coated with photoresist. After spin-coating SPR220 onto the Al layer, the pressure diaphragms were patterned and developed. Figure 4.9 shows the mask used to transfer the pressure diaphragm patterns onto the photoresist.

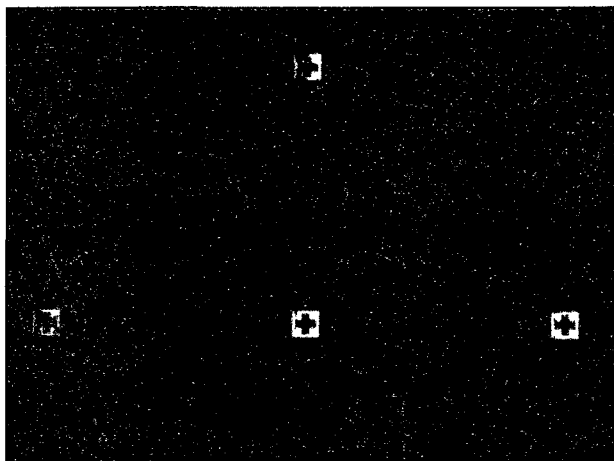


Figure 4.8. Picture of the dark-field trace-guide mask used to pattern trace guides on the center of the pressure diaphragm (on the other side of wafer).

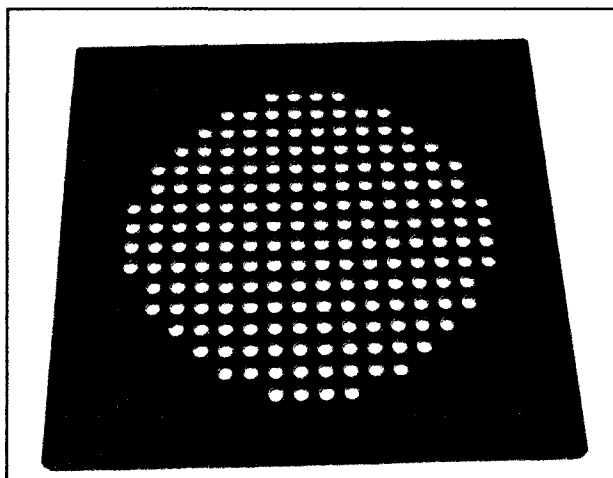


Figure 4.9. Dark-field pressure diaphragm mask showing circular patterns that would be ICP etched.

During exposure, alignment marks on the “pressure diaphragms” mask was used to align the mask to the patterned trace guides on the opposite side. In this way, the alignment marks for the stylus profilometer was positioned accurately over the central region of the pressure diaphragms. Following developing and inspection of the patterns, the wafer was hardbaked.

Commonly known as PAN solution because of its chemical composition, the Al etchant comprising of  $\text{H}_3\text{PO}_4:\text{CH}_3\text{COOH}:\text{HNO}_3:\text{DIH}_2\text{O}$  (16:1:1:2), was used to transfer the photoresist patterns into the Al layer. The Al layer was etched in the etchant at 45 °C for 3 min. Finally, the photoresist was stripped and the wafer was rinsed and dried using QDR and SRD. Using the Al layer as a hardmask, the trace guide side of the wafer was etched up to a depth of 10  $\mu\text{m}$ . The BOSCH recipe used in the ICP etching of the Si substrate is detailed in Appendix B. The wafer was then flipped over and the pressure diaphragms were etched until diaphragms of approximately 50  $\mu\text{m}$  thickness were obtained across the wafer. Finally, the Al layer was stripped off with a final immersion in the Al etchant. Figure 4.10 shows a contour plot of the etch-depth profile of the pressure diaphragms across the wafer surface. As evident from the figure, the ICP etching was not uniform across the wafer and thus diaphragms of varying thicknesses were obtained. Hereafter, the wafer with the pressure diaphragms is referred to as ‘pressure diaphragm wafer’.

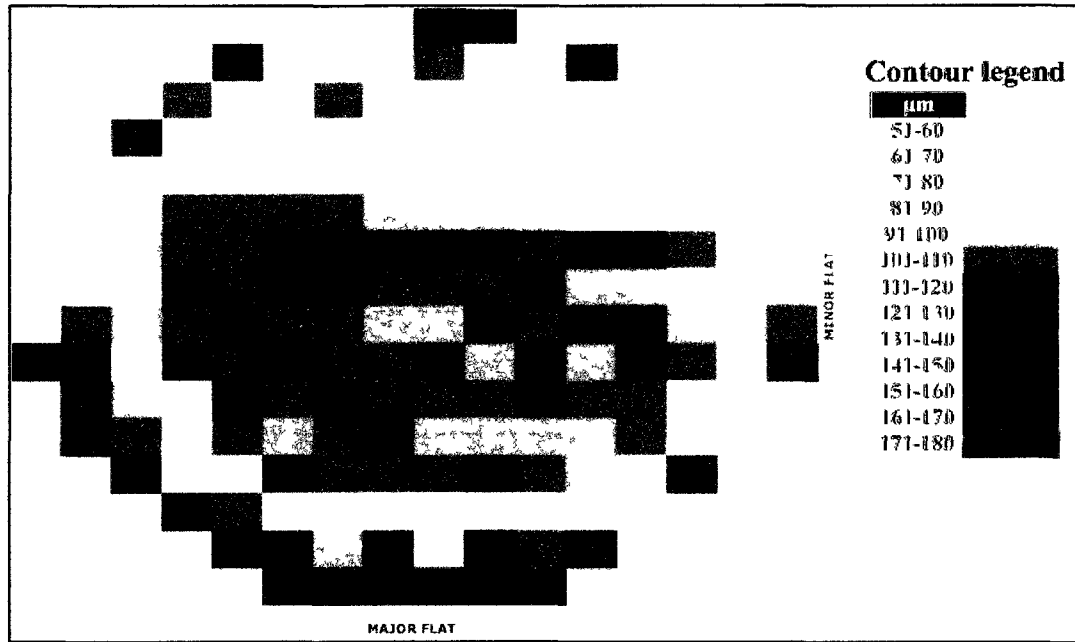


Figure 4.10. Contour plot created in Excel from the etch-depth profile of ICP etched pressure diaphragms.

#### 4.5 Experimental Procedure for Measuring Vacuum Pressure

The cavity wafer and the pressure diaphragm wafers were plasma-activated in O<sub>2</sub> plasma using the recipe mentioned previously. Following QDR and SRD, the wafers were aligned and bonded at  $2 \times 10^{-4}$  mBar vacuum pressure. Figure 4.11 shows an illustration of the wafer-stack with the pressure diaphragm and vacuum cavity. Once the bonded wafer-stack was unloaded, deflection of the pressure diaphragms (as a result of the difference in the pressure between ambient and internal cavity pressure) was clearly evident. NIR image of the wafer-stack is shown in Figure 4.12. The wafer-stack was measured for diaphragm deflection magnitude using a stylus tip profilometer. Figure 4.13 shows an illustration of the trace-path of the stylus tip along the trace-guides etched into the pressure diaphragm wafer. As illustrated in the figure, the tip was traced from a reference start point (*R1*) to the reference finish point (*R2*). *R1* and *R2* were kept on either

side of the diaphragm, thus having the same step height. Step height ( $h$ ) of  $RI$  and the mid-point ( $MP$ ) were measured by the profilometer, which gave the maximum deflection magnitude of the pressure diaphragm. This measurement technique was repeated over several diaphragms and the deflection magnitudes of the diaphragm were recorded.

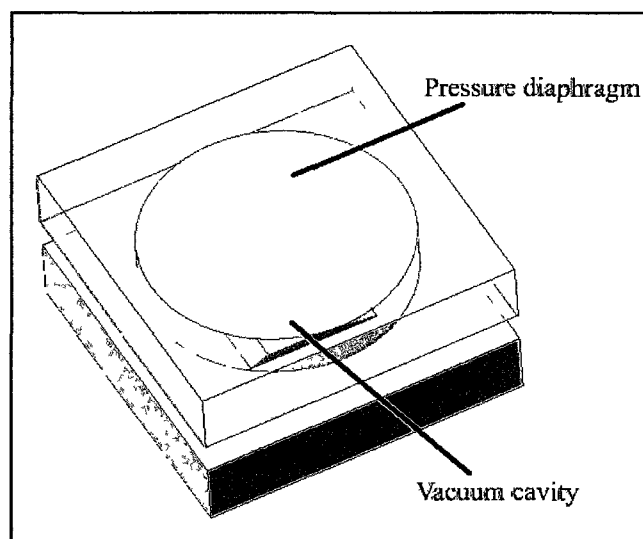


Figure 4.11. Illustration of the pressure diaphragm-vacuum cavity stack.

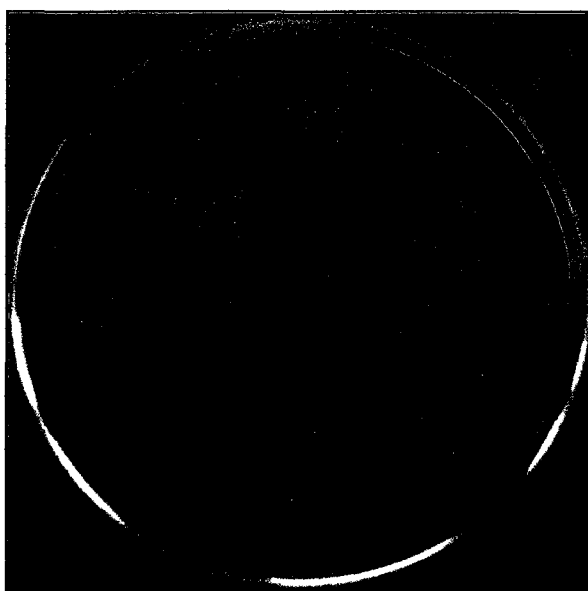


Figure 4.12. NIR image of the pressure diaphragm-vacuum cavity wafer-stack showing a good bond quality with no debonded regions at the interface.

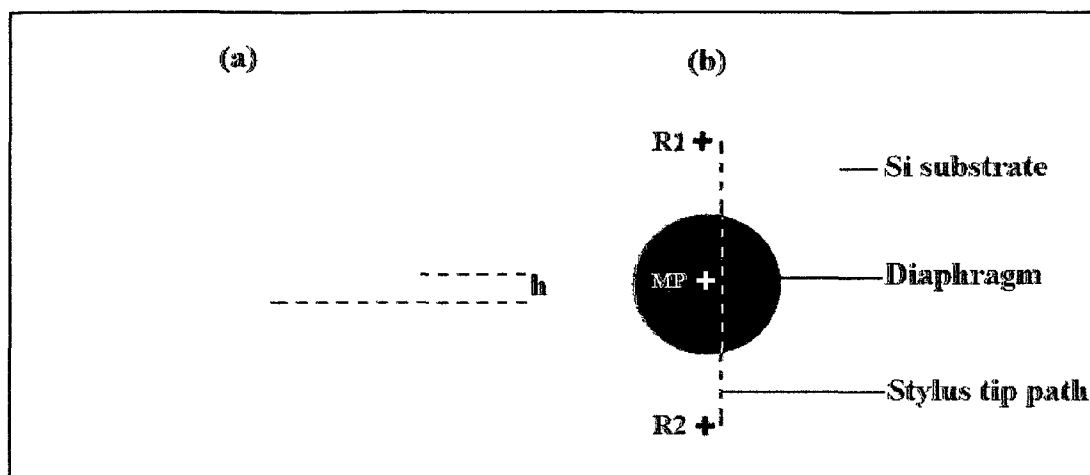


Figure 4.13. Illustration of the trace followed by the stylus tip profilometer to measure the maximum deflection magnitude of the pressure diaphragm. (a) side-view (b) top-view.

#### 4.6 PZT Thin-Film Deposition

Thin-film PZT was deposited onto a Si substrate through sol-gel deposition technique. A top-down fabrication approach was carried out to fabricate PZT microcantilevers, where the composite beam layers were deposited first followed by patterning and etching of the consecutive layers. Initially, a (100) Si wafer with 1  $\mu\text{m}$  thick thermal  $\text{SiO}_2$  layer was selected and cleaned with acetone and isopropyl alcohol. After QDR and SRD in DI  $\text{H}_2\text{O}$ , the wafers were sputter coated with 25  $\text{nm}$  thick Ti layer followed by 125  $\text{nm}$  thick Pt layer. Ti served as an adhesion layer for increasing the adherence of Pt to  $\text{SiO}_2$ .

Sol-gel deposition of thin-film PZT began first with the spin-coat deposition of lead titanate (PT) on the Pt surface of the wafer. The spin coating recipe is included in Appendix B. PT deposition was followed by annealing in a furnace at 450  $^\circ\text{C}$  for 30 min. Annealing was carried out in such a way so as not to thermally shock the deposited layer. Hence, the furnace-temperature was raised from room temperature to the target

temperature at a ramp rate of 2 °C/min. The same process was carried out for cooling the wafers back to room temperature. Following the Pt deposition, 5 ml of PZT was pipetted onto the wafer and spin-coated (refer Appendix B for spin-coating recipe). Pt served as the adhesion seed layer to enhance the adhesion of PZT onto the Pt surface. Following the spin coating of PZT, the layer was pyrolyzed at 110 °C for 10 min on a hot plate to sublimate polymers from the PZT layer. The wafers were then transferred to the furnace and annealed at 450 °C, where the furnace temperature was ramped up from room temperature to the target temperature at a rate of 2 °C/min. This process was repeated until 1 µm of PZT was achieved. The deposition of the Pt adhesion layer was carried out after every three layers of PZT deposition in order to ensure a crack-free continuous PZT thin-film across the wafers. The final 1 µm thick PZT layer was annealed at 600 °C in order to improve the crystal orientation of PZT, significantly reducing film-stress in the process. Following the sol-gel deposition, a final Pt layer was sputtered onto the PZT layer. This deposition process ensured a continuous thin-film PZT layer with top and bottom Pt electrodes. Finally, a 500nm gold (Au) layer was sputtered onto the top Pt layer, following a 25 nm Ti sputter deposition (in order to improve Au adhesion to Pt).

#### **4.7 Fabrication of PZT Microcantilevers**

The objective was to fabricate PZT microcantilever beams onto a Si substrate. A device package containing several beams were placed into a ceramic package in order to electrically interface the top and bottom Pt electrodes to external actuation or data acquisition systems. Initially the wafers were cleaned with acetone and isopropyl alcohol. After a DI H<sub>2</sub>O rinse using QDR and SRD, the wafers were dehydrated at 250 °C on a hot plate for 5 min. Following dehydration, HMDS primer was spin-coated onto the

wafer surface (recipe included in Appendix B) in order to improve the adhesion of the photoresist in the next step. SPR 220 positive photoresist was spin-coated onto the wafer, using spin-recipe included in Appendix B, and was soft baked in order to sublimate dissolved polymers in addition to improving the photoresist adhesion onto the Pt surface. Soft baking was carried out first by heating the wafer substrate to 90 °C for 1.5 min on a hot plate, then at 100 °C for 1.5 min, and finally at 110 °C for 3.5 min. Following a ramp-down of the temperature after soft baking by reversing the ramp-up process, the wafer was transferred onto the mask-aligner. The photoresist was initially exposed with the Au bond-pad mask pattern at 1000 W for 7 s. A multiple exposure technique was carried out in three cycles with 10 s interval between each cycle in order to prevent thermally shocking the temperature-sensitive photoresist. After developing the exposed wafer in MF319 developer, the wafer was rinsed in DI water and dried. Once the patterns were inspected under a microscope, the photoresist was hard-baked at 125 °C. Following lithography, exposed regions of the Au layer were etched using Aqua-regia Au etchant at 80 °C for 3 min. A final photoresist strip using acetone left behind Au bond pads on the top Pt surface. These bond pads would serve as electrodes to which Au wires could be wire-bonded later in the device packaging stage. Figure 4.14 shows an illustration of the etched Au bond-pads and the mask-pattern used in the fabrication of the Au bond pads. Following the Au bond-pad fabrication, the top Pt electrodes and PZT beams were patterned and developed using the same process discussed above. After lithography, the patterns were permanently transferred onto the wafer with the help of dry plasma etching of the top Pt and PZT layers. Chlorine (Cl) plasma was used to carry out the etching process. A combination of Cl gas at a 20 sccm flow-rate and Ar gas at 25 sccm flow-rate

wasselected in an RIE chamber at chamber pressure and power of  $6.67 \times 10^{-3}$  mBar and 300 W respectively.

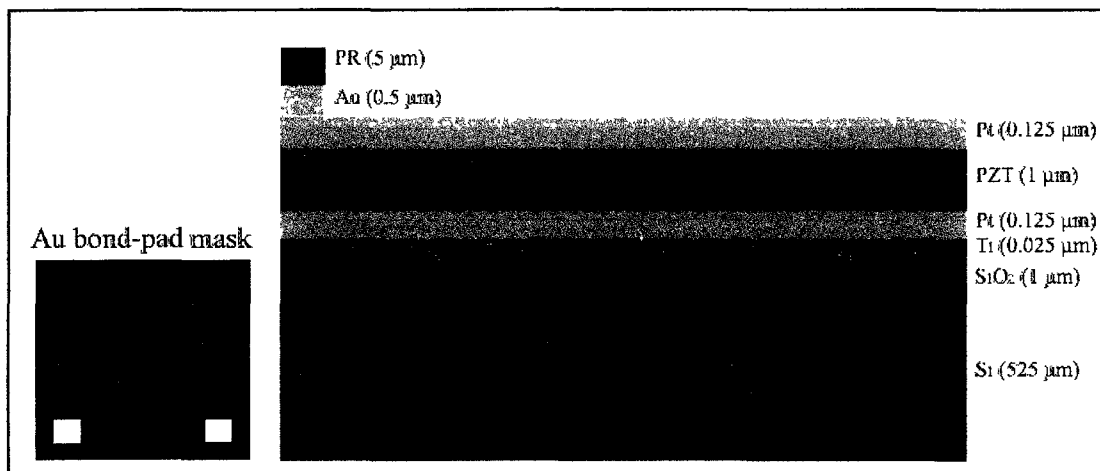


Figure 4.14. Illustration of patterning and etching of Au bond-pads on the top Pt surface of the Si wafer.

Plasma etching of the exposed layers resulted in a profile illustrated in Figure 4.15. The employment of optimized recipes for etching Pt and PZT helped in obtaining accurate layer thicknesses. The bottom Pt electrode was patterned in the same way.

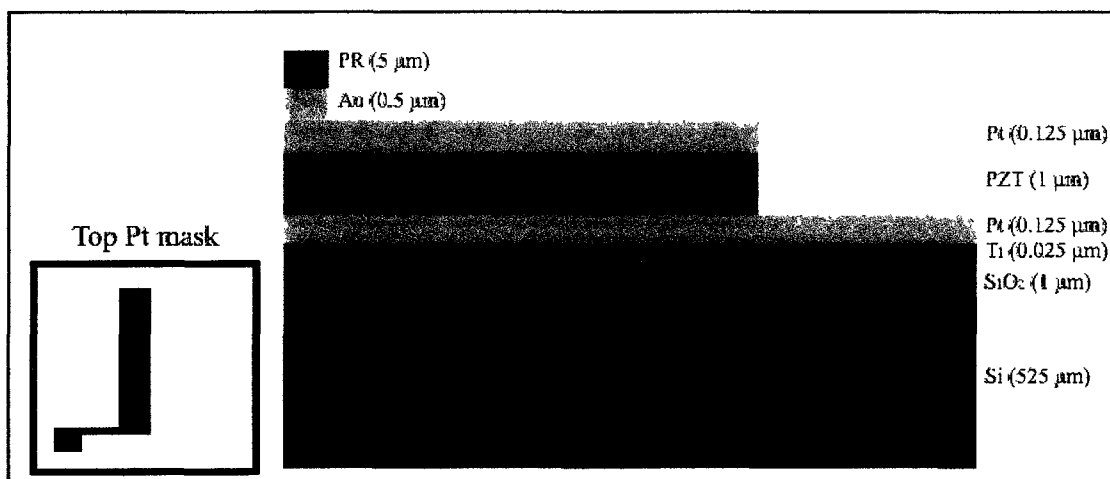


Figure 4.15. Illustration of the patterning and etching of top Pt and PZT layer using the top Pt light-field mask.

Meanwhile, the light-field Pt bottom mask protected the top Pt electrode pattern as well. The same etching recipe used for the top Pt and PZT was used to etch the bottom Ptelectrode pattern as well as the Ti adhesion layer. Figure 4.16 shows an illustration of the mask employed as well as the side-view profile of the etched layer-stack. The next step was to pattern and etch the oxide layer to open up windows for the Xenon difluoride ( $\text{XeF}_2$ ) etching of Si.  $\text{XeF}_2$  was used to dry-etch the Si substrate for the purpose of releasing the fabricated cantilever beams.  $\text{SiO}_2$  served as the masking agent for the  $\text{XeF}_2$  etching of Si. Oxide etching was carried out using RIE:  $\text{CHF}_3$  at 35 sccm,  $\text{CF}_4$  at 5 sccm, and He at 266.64 mBar chamber pressure and 100 W RF power. Figure 4.17 shows an illustration of the  $\text{XeF}_2$  etch pattern of the oxide layer and the dark-field mask used in the lithography process. Since RIE etching of  $\text{SiO}_2$  was found to have detrimental effects on the Au bond pads, they were protected during the oxide etching using photoresist.

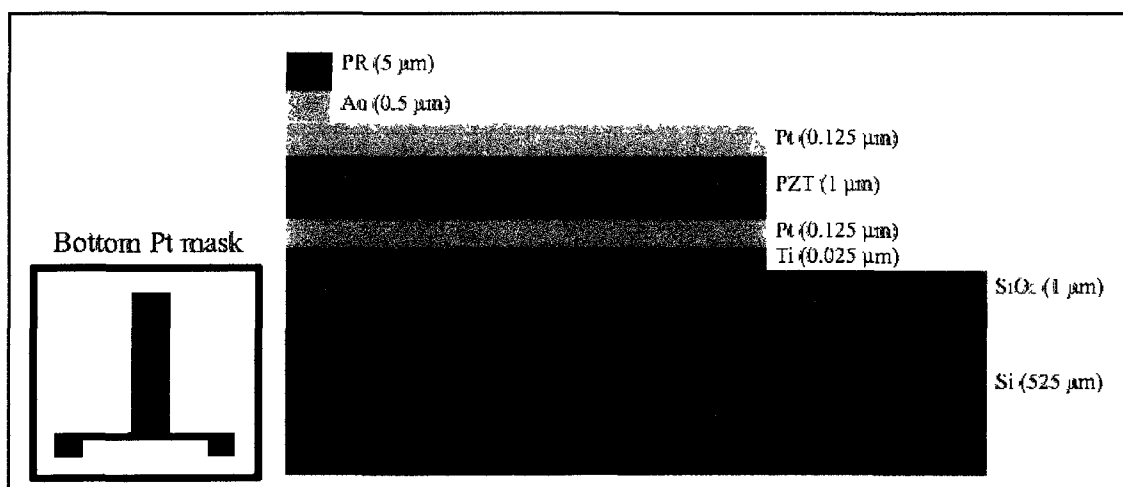


Figure 4.16. Illustration of the bottom Pt electrode and Ti adhesion layer etching using a light-field bottom Pt mask.

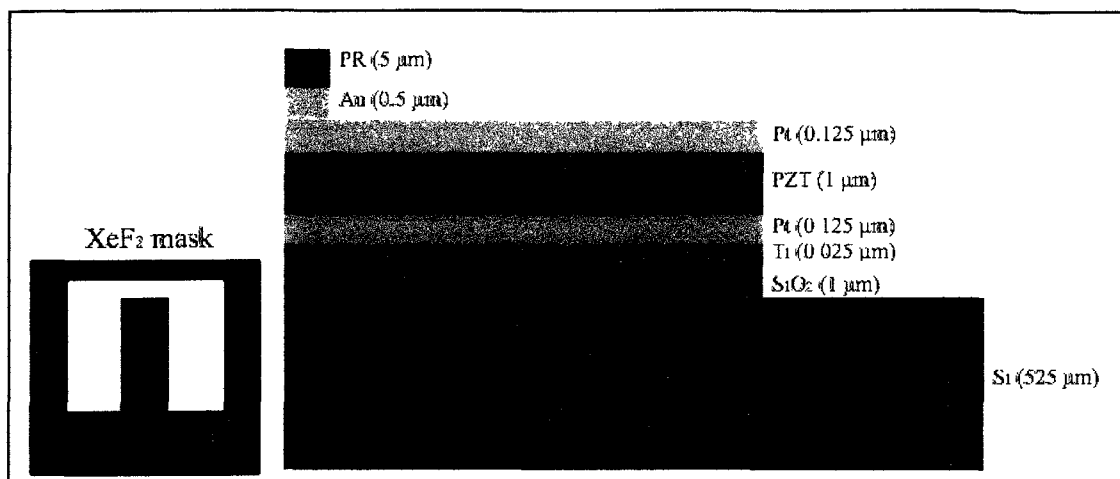


Figure 4.17. Illustration of the  $\text{XeF}_2$  patterning and etching of  $\text{SiO}_2$  layer with a dark-field mask.

The wafer was finally stripped of photoresist and was cleaned and dried using QDR and SRD. Figure 4.18 shows a picture of the patterned and etched device wafer before being diced for  $\text{XeF}_2$  etching. A Xactix  $\text{XeF}_2$  etching station was used to etch the exposed Si around the cantilever beams.  $\text{SiO}_2$  was used as the masking agent during the etching process. In this way, the cantilever beams were released from the Si substrate.

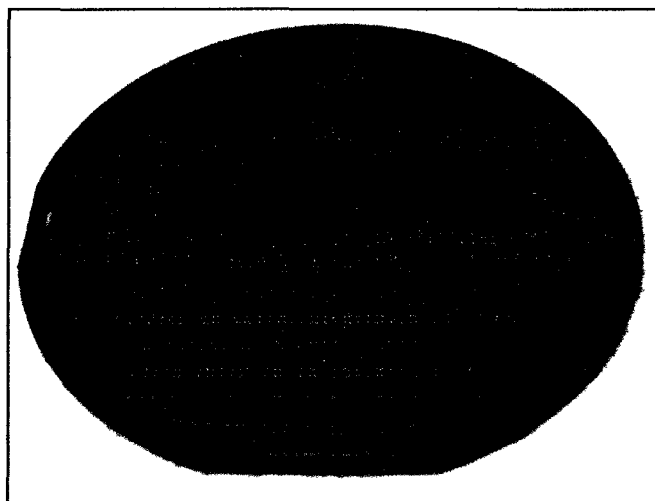


Figure 4.18. Picture of the device wafer showing the fabricated PZT cantilever beams.

The wafer was diced into individual dies using a dicing saw. Each of the individual dies consisted of four PZT beams in total that were electrically isolated from each other. This meant that each of the devices could be actuated or measured for voltage/current independently. Figure 4.19 shows an illustration of a device die. The device die was mounted onto a ceramic package using a tri-bond epoxy. The epoxy was cured at 85 °C for 4 hr. Au wires were used to wire-bond the Au bond pads on the dies with the bond pads of the ceramic package, using a ball bonder.

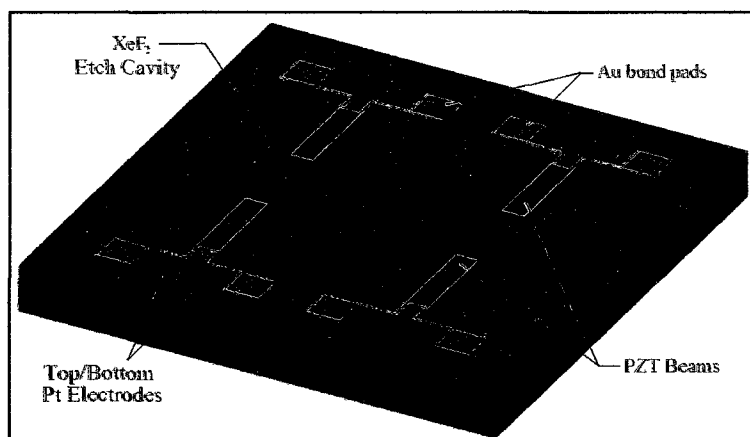


Figure 4.19. Illustration of the device die containing four PZT beams on a Si substrate.

Figure 4.20 shows a picture of the packaged device. Glass lid that seals the packaged device from external elements was not placed over the device die since the packaged device was to be tested in ambient air pressure and vacuum pressures. Sealing the device with the glass lid would prevent the cantilever beams from being subjected to the controlled ambient air pressure studies.

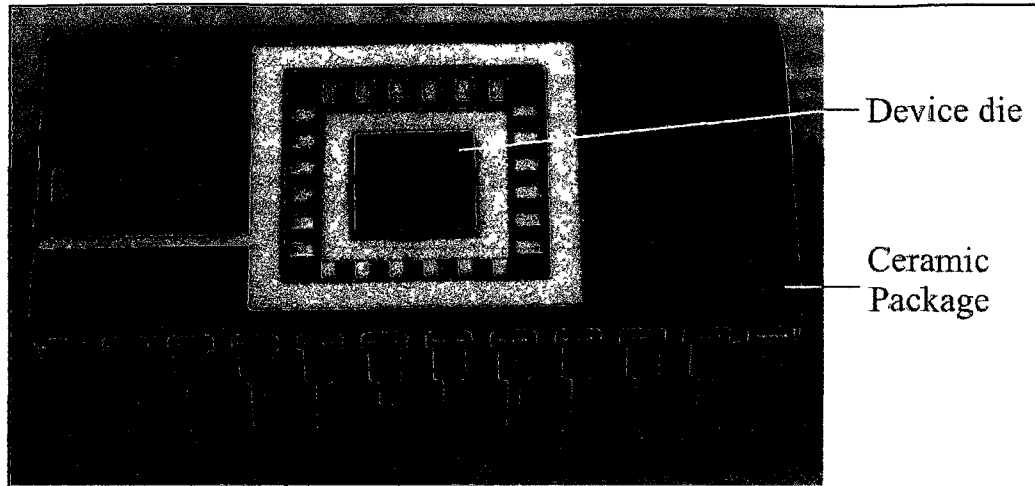


Figure 4.20. Picture of a packaged device die onto ceramic package.

#### 4.8 Experimental Setup and Results for Device Capacitance Measurements

Capacitance of the PZT composite beam was accurately measured using a Keithley electrical test-bench. The experimental setup is shown in Figure 4.21. As shown in the figure, actuators were used to electrically connect to the bond pads of the device. Using BNC cables attached to the actuators, a multimeter was interfaced with the test-bench that measured the device capacitance.

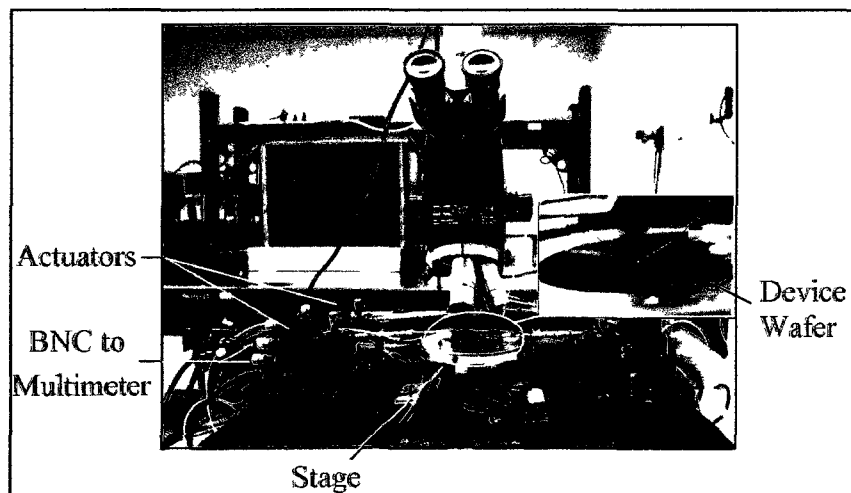


Figure 4.21. Picture of the experimental setup of capacitance measurement of the devices using a Keithley test bench.

PZT composite beam with top and bottom electrodes act as a parallel plate capacitor. Capacitance of a parallel plate capacitor can be calculated using Equation (4.1).

$$C = \frac{\epsilon_0 \epsilon_r A}{d} \quad (4.1)$$

$C$  is the capacitance,  $\epsilon_0$  is the permittivity of free-space ( $8.85 \times 10^{-12} \text{ m}^{-3} \text{ kg}^{-1} \text{ s}^4 \text{ A}^2$ ),  $\epsilon_r$  is the relative permittivity,  $A$  is the surface area of the parallel plates, and  $d$  is the distance between the plates.  $\epsilon_r$  of PZT was found to be 1700 (from the manufacturer listed in Appendix B), surface area of the Pt electrodes was calculated to be  $A=35000 \text{ } \mu\text{m}^2$ , and the distance between the electrodes was  $1 \text{ } \mu\text{m}$ . Substituting these constants into Equation (4.1), the theoretical capacitance of the composite beam was calculated to be  $C=5.27 \text{ nF}$ . Similarly the capacitance of the top electrode bond pad (the other just containing a bottom electrode layer of Pt) was calculated to be  $2.41 \text{ nF}$ . Since the capacitors are in parallel, the capacitances add up to give overall device capacitance of  $7.63 \text{ nF}$ . Using the experimental setup shown in Figure 4.21, the device capacitance was measured to be  $9 \text{ nF}$ . The reason for the discrepancy in the theoretical and electrical capacitances was due to the added parasitic capacitances in the composite beam.

#### 4.9 Experimental Setup for Testing PZT Resonators in Vacuum and Air

The fabricated and packaged device was operated in varying air pressure magnitudes in order to study the air-damping effects on the resonance characteristics of the PZT beam. First, the beam was operated in atmospheric air pressure of  $1000 \text{ mBar}$ . This was accomplished by connecting the top and bottom electrode pins of the ceramic package to an external function generator. A sine waveform of  $50 \text{ mV}$  amplitude was used to actuate the beams. A function generator aboard a cathode ray oscilloscope was

used to generate the sine wave. The deflection magnitude of the beam was measured using a laser Doppler vibrometer. The fiber optic cable from the laser interferometer was connected to an optical microscope so that the laser spot could be accurately focused onto the tip of the actuating PZT beam placed atop the microscope stage. The experimental setup used to actuate and measure beam deflection is shown in Figure 4.22. The deflection magnitude of the beam, measured by the laser vibrometer, was recorded using a PC interfaced to a digital signal processor module. A frequency sweep from 300-1700 Hz was performed for the aforementioned voltage amplitude on the device, and the corresponding maximum tip deflection magnitudes were recorded. The change in the resonance characteristics of the PZT beam was studied by actuating the beam in vacuum. This was accomplished by placing the device package in a vacuum chamber as shown in Figure 4.23. The device inside the vacuum chamber was electrically connected to the function generator by means of electrical feed-throughs that came equipped with the chamber.

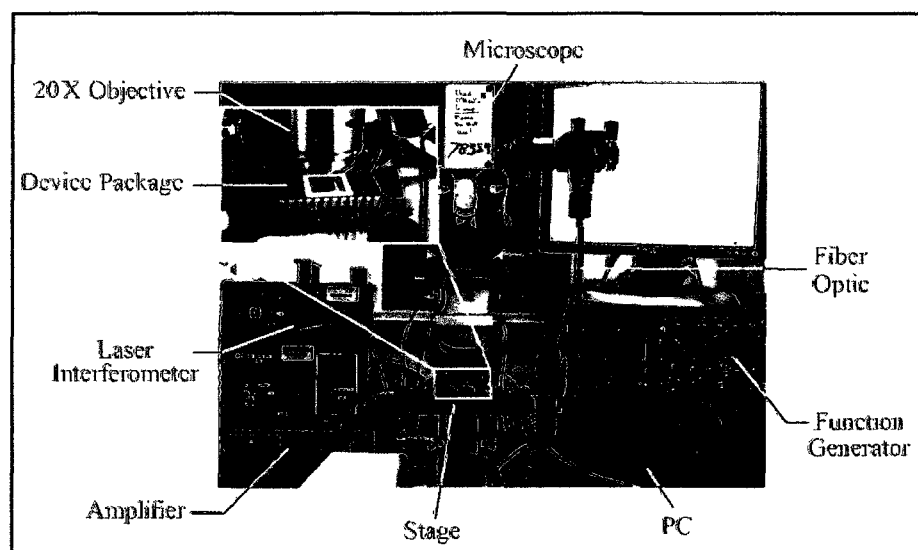


Figure 4.22. Picture of the experimental setup of PZT beam actuation in atmospheric air pressure.

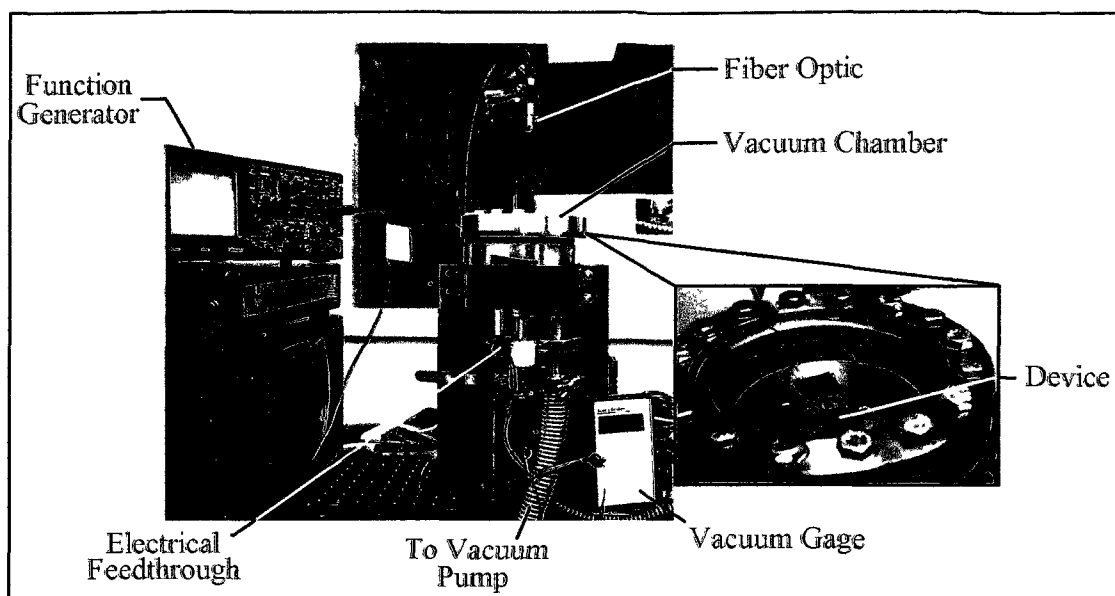


Figure 4.23. Picture of the experimental setup for actuating PZT beam in vacuum.

The chamber was evacuated and internal pressure was held at 0.5 mBar. Chamber pressure was monitored using a vacuum gage interfaced with the system. The laser vibrometer fiber optic was placed above the window of the vacuum chamber lid, and the laser spot from the interferometer was roughly focused on the tip of the PZT beam. Since an Al chuck was used as a flat platform for the device package, an insulating electric tape was used below the pins of the ceramic package in order to prevent an electrical short circuit. The beam was actuated at 50 mV using a sine wave for frequencies ranging from 350-1700 Hz. Corresponding deflection magnitudes of the beam was recorded using a PC interfaced to the digital signal processor of the laser vibrometer.

## **CHAPTER 5**

### **RESULTS AND DISCUSSION**

This chapter documents the results obtained from the different theoretical and experimental models. It compares the results obtained from various test-benches and discusses the reasons for certain characteristics. Solutions to problems faced in certain areas of study were also discussed.

#### **5.1 Bond Integrity Results of Plasma-Activated Fusion-Bonded Wafers**

Immediately following pre-bonding and annealing, the wafer-stack was inspected for bond integrity. A closer look at the surface of the wafer-stack using an optical microscope showed cracks at 90° angles. Figure 5.1 shows the microscope image obtained. The cracks were formed at exactly 90° to each other due to the perfect crystalline nature of the Si wafers used in the fusion bond. This phenomenon, known as stacking faults, was caused due to the uneven application of pressure during the fusion-bonding process. The reason for uneven pressure application was caused by large particulates trapped in between the wafer substrates. A thorough cleaning of the wafer surface, in addition to meticulously inspecting and handling exposed wafer surfaces solved this problem. Stacking faults had detrimental effects on the bond quality of the wafers. This was revealed when the bond failed during the dicing of the wafer-stack.

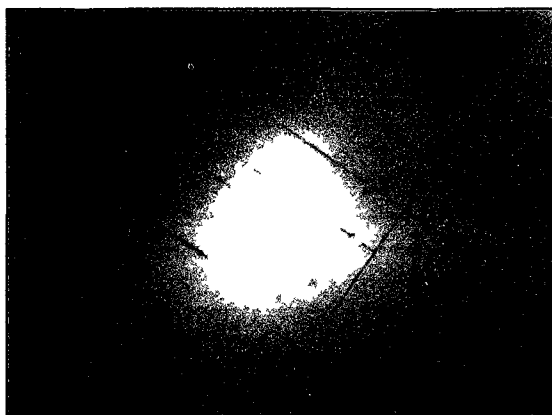


Figure 5.1. Microscope image of the top surface of fusion-bonded Si wafer-stack showing stacking faults.

NIR imagery was used to inspect the bond quality between wafers. Debonded regions were evident as Newton rings. Figure 5.2 shows an NIR image of a plasma-activated and bonded wafer pair in comparison with wafer pairs with debonded/air-pocket regions. As evident from the figure, plasma-activated wafers showed no debonded regions at the interface ensuring a good bond. Tensile test results of random dies diced from plasma-activated and bonded wafer-stacks showed a bond strength of 22.5 MPa, which was close to the bulk fracture strength of 24 MPa for Si.

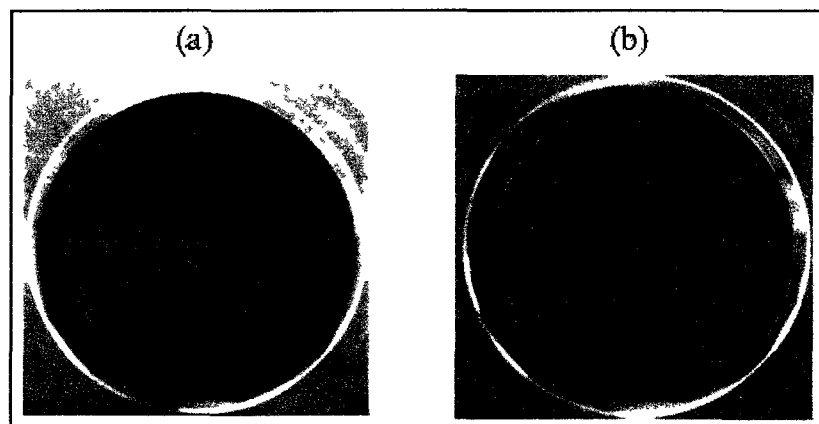


Figure 5.2. NIR images of fusion-bonded Si-Si wafers showing (a) a good bond (b) debonded regions at the interface revealed by Newton rings.

The integrity of the bond was also further confirmed by examining the interface of the bonded wafer. In order to achieve this, a small die was cleaved from the wafer stack and was examined under a scanning electron microscope (SEM). Figure 5.3 shows the SEM micrograph of the interface of the cleaved die. As evident from the figure, the interface was barely visible. This ensured that the bonded surfaces were in fact fused together ensuring a permanent seal.

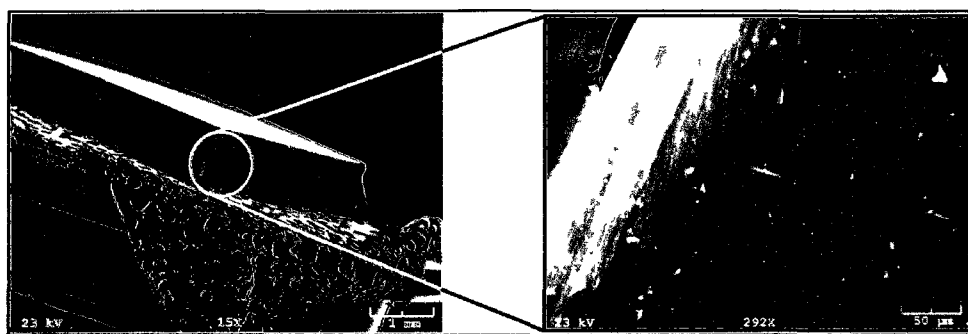


Figure 5.3. SEM micrograph of the interface region of a cleaved die diced from plasma-activated Si wafer stack. Inset: Close-up of the edge of the cleaved die showing a hairline of what was the interface between the two wafers.

## 5.2 Significance of RCA Cleaning

This study was conducted in order to determine the significance of an RCA wet chemical activation technique when a dry surface activation technique, like plasma-activation, was employed. RCA cleaning was usually carried out before plasma-activation and immediately following the BOE treatment of the wafers. In this study the wafers were treated for native oxide removal using BOE and then rinsed in DI water using QDR and SRD. The RCA 1 and 2 treatments, which were the next steps before pre-bonding the wafers, were eliminated here. Hence, the wafers were plasma-activated and pre-bonded immediately following the QDR and SRD after BOE treatment. After the

final thermal annealing process, the wafers were inspected using NIR imagery. As evident from Figure 5.4, wafers that were not treated with RCA had debonded regions at the interface. While the surface of the wafers was activated during plasma-activation, removal of metallic and organic impurities was imperative, which could only be possible with an RCA treatment. Even though the initial acetone and IPA treatment of the wafer surfaces removes organic impurities, a thorough organic strip was absent with the elimination of RCA process as a whole. Tensile tests revealed that wafers bonded without an RCA treatment had an average bond strength of 18 MPa, which was significantly lower than those wafers given an RCA treatment (22 MPa).

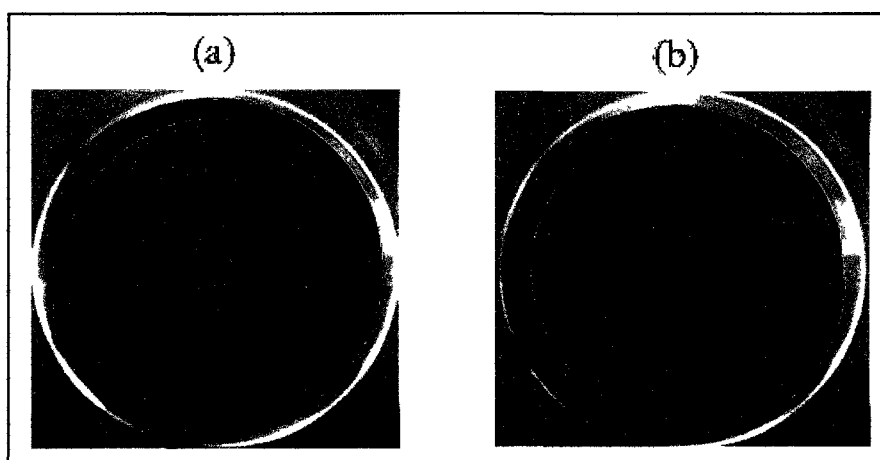


Figure 5.4. NIR image of (a) wafers bonded with RCA treatment (b) wafers bonded without RCA treatment.

### 5.3 Sequential Plasma-Activation

This study was conducted in order to improve the bond quality of plasma-activated and stored wafers. Storage time was found to cause detrimental effects on plasma-activated wafers. Sequential plasma-activation initially involves the  $O_2$  plasma-activating of substrates followed by activation of the same surface using  $N_2$  radicals in

the same RIE chamber. Several studies have been conducted on the effects of sequential plasma-activation and its improvements on the bond quality [20, 21]. Improved bond quality was reported. After the O<sub>2</sub> plasma-activation, N<sub>2</sub> plasma-activation was carried out in the same RIE chamber at a chamber pressure of  $266 \times 10^{-3}$  mBar, 25 sccm of N<sub>2</sub> gas, and 100 W. Plasma-activation was carried out for 1 min. NIR images of the wafer-stack after the sequential plasma-activation were examined. Figure 5.5 shows the NIR images of the wafer-stack. As evident from the figure, a high density of debonded regions was evident at the interface. An investigation of the surface roughness of the sequentially plasma-activated wafers revealed that the wafer surface roughness was significantly higher after N<sub>2</sub> plasma-activation as compared to just O<sub>2</sub> plasma-activated wafers. Further investigation revealed that N<sub>2</sub> ions were bombarding and slowly roughening the Si substrate during the plasma-activation. Multiple areas of the sequentially activated Si surface were profiled for surface roughness.

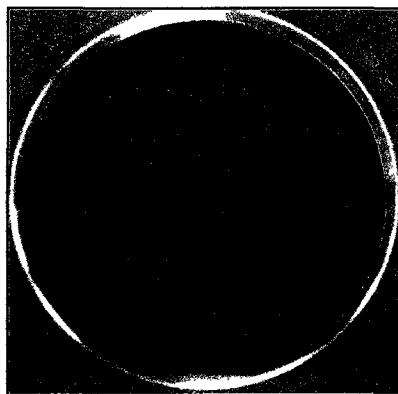


Figure 5.5. NIR images of the wafer-stack bonded after sequential plasma-activation in O<sub>2</sub> and N<sub>2</sub> plasma.

The average roughness was found to be 7 nm, which was significantly higher as compared to 2 nm in O<sub>2</sub> plasma-activated wafers. The increased surface roughness not

only reduced the contact surface area during bonding, but also led to the increased absorption of water molecules at the surface of the wafers. The increased density of H<sub>2</sub>O molecules at the interface resulted in the increased density of released H<sub>2</sub> molecules at the interface. The released H<sub>2</sub> molecules were trapped at the interface during the bonding process, which in turn led to the increased density of voids/debonded regions at the interface of sequentially plasma-activated wafers.

#### 5.4 Final Thermal Annealing Study

Final thermal annealing was an important part of the wafer bonding process as it provides enough kinetic energy to the H<sub>2</sub>O molecules at the interface to diffuse out of the interface. This increases the formation of permanent covalent bonds between Si-O-Si at the interface of the wafer substrates. Final thermal annealing was conventionally carried out in an external furnace at 1000 °C. Using plasma-activation, the final annealing temperature was reduced to 300 °C. Annealing of the wafer-stack in the external furnace, however, had detrimental effects on the bond quality. Figure 5.6 shows the NIR image of the plasma-activated wafer-stack. As evident from the figure, a high density of debonded regions was observed at the interface. This was caused due to the presence of impurities in the ambient atmosphere of the tube furnace. Final bond quality was found to be very sensitive to ambient conditions during annealing. Hence, an *in-situ* thermal annealing was carried out where the prebonded wafer-stack was final thermal annealed within the substrate bonder itself. An NIR image of *in-situ* annealed wafer-stack is shown in Figure 5.7.

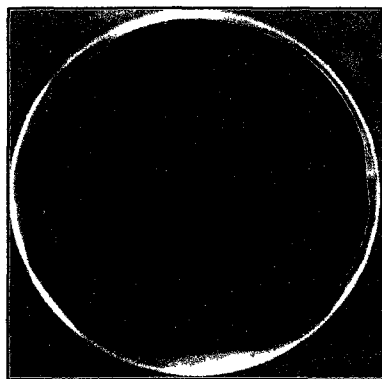


Figure 5.6. NIR image of plasma-activated and bonded wafer-stack annealed in an external tube furnace at 300 °C.

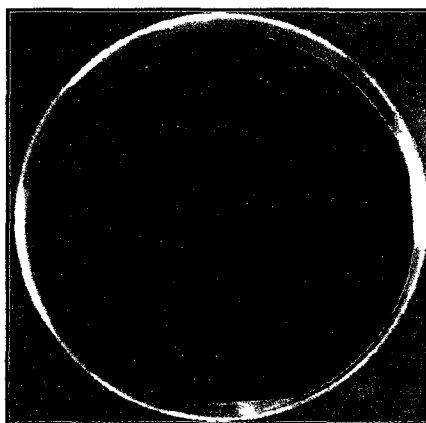


Figure 5.7. NIR image of wafer-stack annealed at 300 °C *in-situ* the substrate bonder immediately following pre-bonding.

After plasma-activation, four Si wafers were stored for 3 hr before being pre-bonded. After pre-bonding, one pair of the Si wafers was pre-bonded and thermal annealed in an external furnace at 300 °C while the other pair was annealed *in-situ* the substrate bonder. Figure 5.8 shows a comparison of the NIR images from this study. As evident from the figure, the wafer-stack bonded *in-situ* showed better bond strength as compared to those annealed in the external furnace. Bond strength measurements of *in-situ* annealed wafers were measured to be 15 MPa, which was significantly higher than

the 5.5 MPa of externally annealed wafers. This proved that in-situ annealed wafer bond quality was superior. Hereafter, all final thermal annealing processes were carried out *in-situ* the substrate bonder immediately following pre-bonding. *In-situ* annealing was only applicable for low temperature annealing. The external furnace had to be used for higher temperatures of 1000 °C.

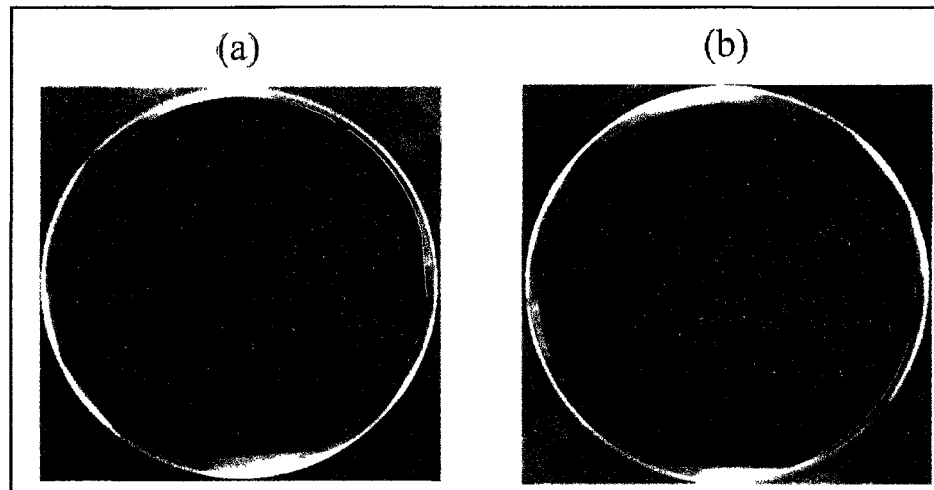


Figure 5.8. Comparison of the NIR images of plasma-activated, 3 hr stored, and pre-bonded wafers annealed (a) in an external furnace (b) *in-situ* substrate bonder.

### 5.5 Evidence of Interfacial Oxide Layer in Plasma-Activated Si/Si Fusion- Bonding

KOH etched dies diced from the wafer stack were analyzed under SEM. Figure 5.9 shows an SEM micrograph of the interface of the etched die. As evident from the figure, a close inspection of the interface of the etched die revealed an inverted V-shaped etch profile. The etch pattern at the interface followed the (111) plane of the Si substrate. SiO<sub>2</sub> layers are known to mask KOH etchant. As mentioned before, the formation of SiO<sub>2</sub> was evident at the interface after fusion bonding. Therefore, it was concluded that the reason for the inverted V-shaped feature at the interface was the KOH etch following the

(111) plane after being masked by the interfacial oxide layer. In the absence of an interfacial oxide layer, the Si etching would have been more uniform in the (010) directions. An illustration of the etch pattern of KOH is shown in Figure 5.10. From the figure it was very clear how the inverted V-shaped etch feature was formed at the interface after the KOH etching of the dies, which confirmed the presence of an oxide layer at the interface of plasma-activated and fusion bonded Si wafers.

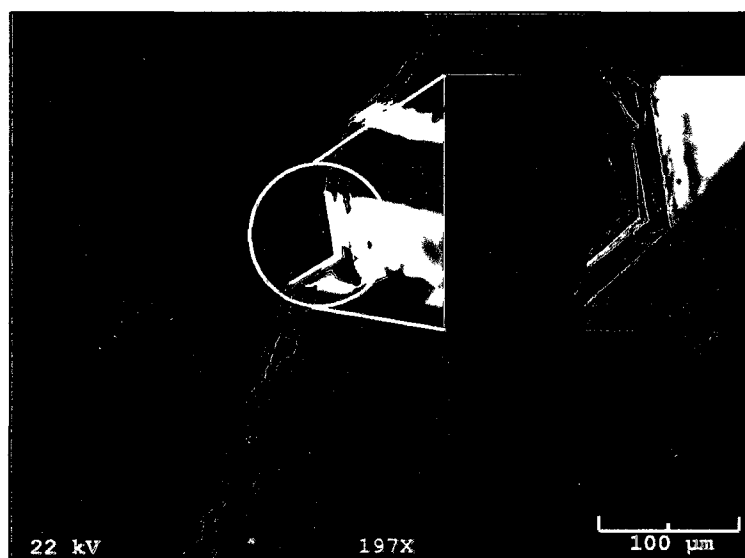


Figure 5.9. SEM micrograph showing the interface of a KOH etched die that was diced from a plasma-activated and fusion bonded wafer-stack. Inset shows a closer look at the inverted V-shaped feature at the interface.

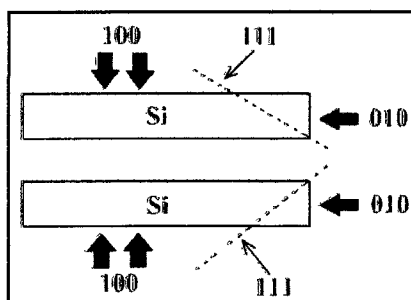


Figure 5.10. An illustration of the etch profile followed by KOH etching on two opposing Si wafers, which was the primary reason for the inverted V-shaped etch feature at the interface.

## 5.6 Effect of Storage Time on Bond Strength

Varying the time interval between plasma-activation and pre-bonding evaluated the effect of storage time of plasma-activated wafers on bond strength. The objective of this study was to investigate a moderate storage time before the bonding-quality was compromised. The storage time was varied from 0 to 168 hr before they were pre-bonded. Tensile tests conducted on dies diced from the wafer-stack quantified the bond strength by measuring the force required to pull the die-stack apart. 4.3×4.3mm dies were used in the tensile test. Table 5.1 shows the tensile test results of ten dies that were diced from wafers that were immediately bonded after being plasma-activated (storage time = 0 hr). Dies from the center and edge portions of the wafer-stack were chosen since the bond-strength varied from the central region to the sides. The reason for this variation was attributed to the wafer bow (less than 30 μm) present at the time of pre-bonding. Average bond strength was calculated along with the standard deviation for each storage times. Finally the average standard deviation of all storage times were calculated and was included in the uncertainty of the tensile test results. Figure 5.11 shows a plot of the results obtained from the tensile tests on wafers stored for varying storage times. From the plot, it was evident that the bond strength deteriorated with the increase in the storage time. Figure 5.12 shows the NIR images of the wafers bonded with various storage times. As evident from the figures, the bond quality increased after 48 hr of storage. Three different samples were taken through the same process cycle in order to rule out any experimental errors. The reason for the decrease in the bond quality and bond strength with the increase in storage time was due to the presence of gas molecules (predominantly H<sub>2</sub>) at the interface. As storage time was increased, the amount of water

molecules adsorbed onto the surface increased as well. This resulted in an increase in the density of released  $H_2$  molecules at the interface as a result of the byproduct of the oxidation reaction in the Si substrate.

Table 5.1: Table showing the bond strength measurements from tensile tests conducted on dies diced from wafers with 0 hr storage time.

Sample	Bond strength (MPa)	Wafer region
1	23.47	Center
2	23.05	Center
3	22.50	Center
4	23.54	Center
5	22.38	Edge
6	22.81	Edge
7	19.82	Edge
8	19.38	Edge

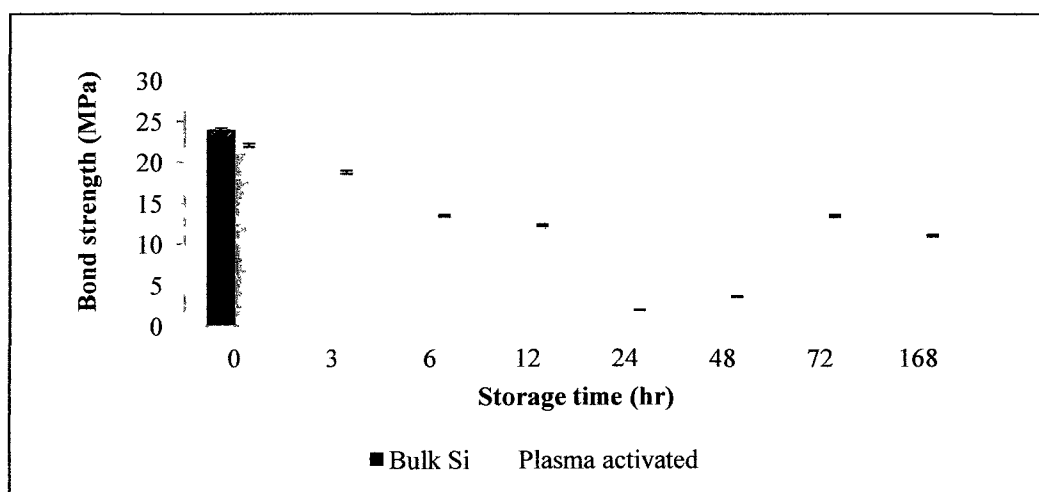


Figure 5.11. Plot showing the bond strength magnitudes of wafers stored for varying time intervals before being pre-bonded.

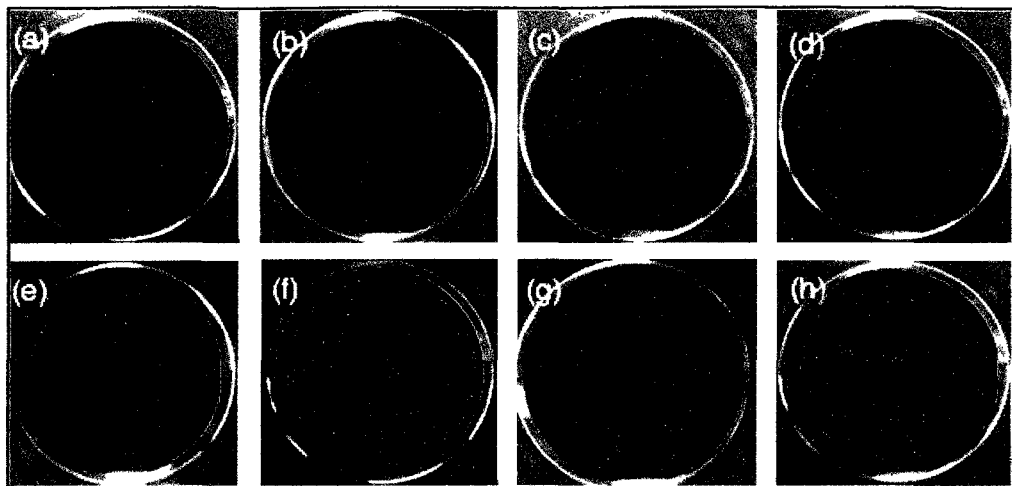


Figure 5.12. Pictures of the NIR images of wafers stored for (a) 0 hr, (b) 3 hr, (c) 6 hr, (d) 12 hr, (e) 24 hr, (f) 48 hr, (g) 72 hr, and (h) 168 hr after plasma-activation and before bonding.

An interesting phenomenon was observed after 48 hr of storage time when the bond strength started to increase again and saturate at 168 hr. This characteristic self-healing nature of bond quality was attributed to the growth of the oxide layer at the surface of the plasma-activated wafers. A separate study was conducted to evaluate the growth of an oxide layer on top of the plasma-activated Si surface. An ellipsometer, with  $70^\circ$  incidence angle, was employed to measure the thickness of the oxide layer. Figure 5.13 shows the results obtained. A thick oxide layer can reabsorb interfacial  $H_2$  molecules. After 48 hr of storage time, the oxide layer was thick enough to absorb any interfacial gas molecules. This increased the bond strength as the density of debonded regions decreased due to the increased absorption of  $H_2$  molecules by the increased oxide layer thickness. Hence, the sudden increase in bond strength for wafers stored for greater than 48 hr after plasma-activation and before pre-bonding. This demonstrated the ability of an interfacial oxide layer to getter interfacial gas molecules.

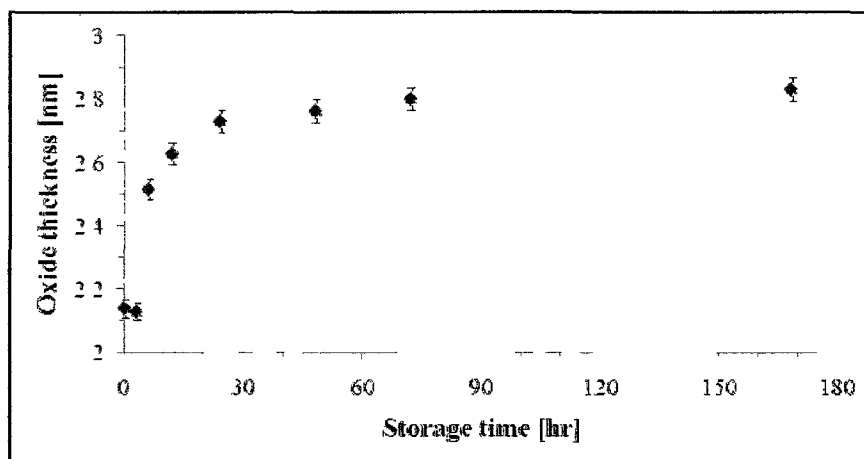


Figure 5.13. Plot showing the increase in the oxide thickness with increase in storage time of plasma-activated wafers.

### 5.7 Plasma-Activated Si/SiO<sub>2</sub> Bonding

The gettering capability of an SiO<sub>2</sub> layer was investigated by performing a fusion bond between Si-SiO<sub>2</sub> wafers. The SiO<sub>2</sub> wafer had an oxide thickness of 2 μm. Since the bond strength and quality was the lowest for a 48 hr storage time, both of the wafers were plasma-activated and stored for 48 hr before being bonded. Figure 5.14 shows the NIR images of the wafer-stack. From the figure, it was evident that the Si-SiO<sub>2</sub> wafer-stack showed better bond quality when compared to the Si-Si wafer-stack. The 2 μm thick oxide layers was able to getter and absorb the interfacial gas molecules thereby rendering a void-free interface. It was necessary to plasma-activate both the Si and SiO<sub>2</sub> wafer. Though hydrophilic in nature, a thick oxide layer will prevent the water molecules from reaching the Si substrate to further oxidize it and release H<sub>2</sub> molecules. In addition, thick oxide layers are unable to bond to a Si substrate at a low temperature of 85 °C due to the lack of bonding sites. Plasma-activation of SiO<sub>2</sub> wafers creates a porous oxide layer that facilitates the propagation of water molecules to the underlying Si substrate to oxidize Si, in addition to creating bonding sites (OH groups) at the interface. Figure 5.15 shows a

comparison of Si-SiO<sub>2</sub> wafers that were and were not plasma-activated before fusion bonding.

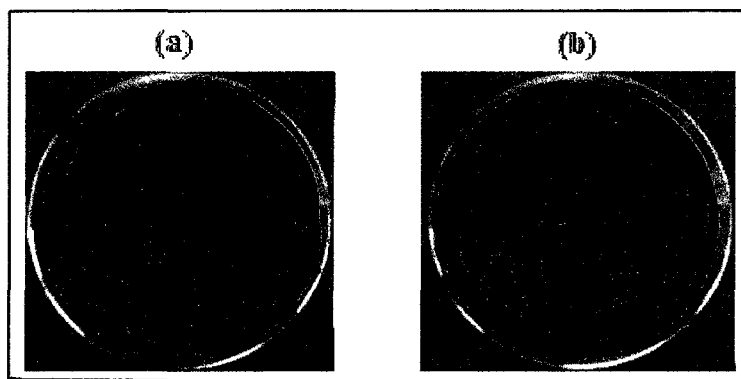


Figure 5.14. Comparison of NIR images of (a) Si-SiO<sub>2</sub> and (b) Si-Si plasma-activated wafers both stored for 48 hr.

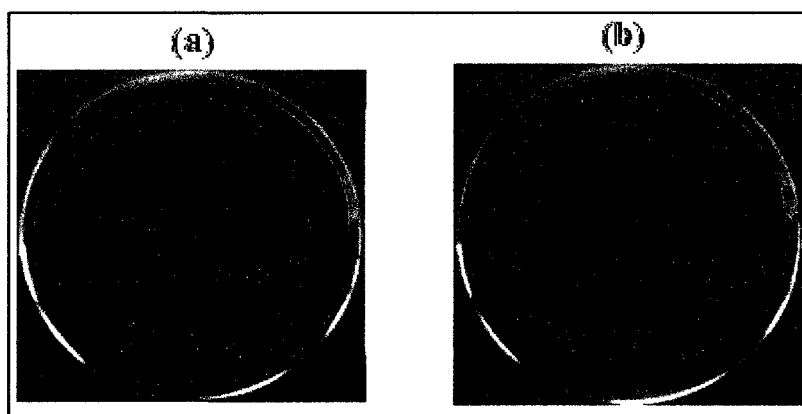


Figure 5.15. NIR images of Si-SiO<sub>2</sub> where (a) both wafers were plasma-activated (b) only the Si wafer was plasma-activated.

### 5.8 Plasma-Activation Before or After Storage

From plasma-activation vs. storage time studies, it was concluded that storing the wafers for 48 hr produced the worst case scenario of low bond strength and bond quality. Since the purpose of storage time was to simulate the time lapse that may occur in an industrial fabrication process flow, it was interesting to evaluate the bond quality of

wafers that were plasma-activated after being stored for a specified time interval. In this case, the wafers were stored after being RCA cleaned and rinsed/dried in DI water. Following storage for 48 hr, the wafers were plasma-activated and immediately bonded. NIR images of the wafers that were plasma-activated before and after storage time were taken and compared, as shown in Figure 5.16. As evident from the figure, wafers that were plasma-activated after being stored for 48 hr showed superior bond quality as compared to those that were activated and then stored. In the case of wafers stored after plasma-activation, a thin layer of oxide was formed on the wafer surfaces. The hydrophilic wafer surfaces attracted H<sub>2</sub>O molecules from the ambient air. During bonding, these H<sub>2</sub>O molecules contributed to the increase in H<sub>2</sub> molecules at the interface, which in turn increased the density of voids at the interface. In the case of wafers stored and then plasma-activated, the absorbed H<sub>2</sub>O molecules were evaporated off in the RIE due to the vacuum pressure in the chamber. In addition, plasma-activation further increased the OH<sup>-</sup> groups at the surfaces of the wafers. The combination of reduced H<sub>2</sub>O molecules and increased reactivity of the surfaces contributed to the decrease in the density of voids at the interface. The bond strength of wafers stored before plasma-activation was found to be 19 MPa, which was significantly higher than the bond strength of 5.6 MPa for wafers that were stored after plasma-activation. It was concluded that wafers that needed to be stored for longer time periods could be plasma-activated and bonded immediately in order to obtain good bond quality between the wafers.

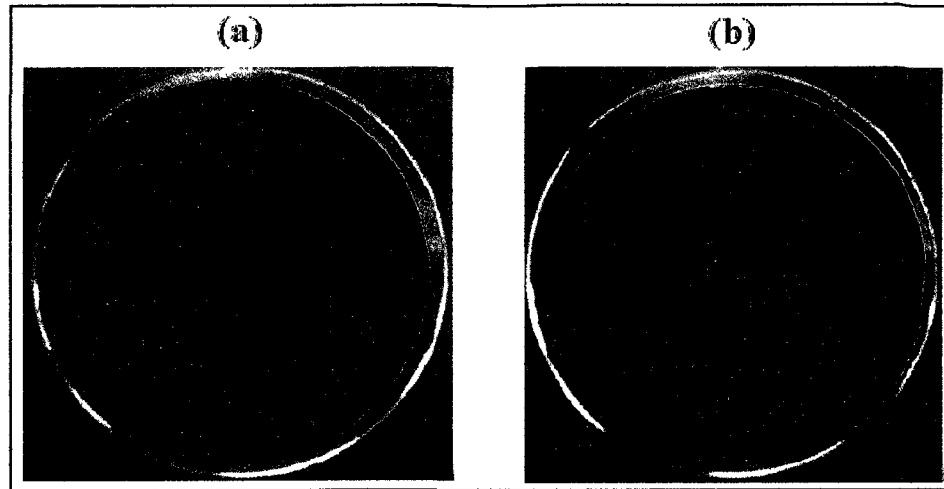


Figure 5.16. NIR images of bonded wafer-stack comparing the wafer-pairs that were plasma-activated (a) before 48 hr storage time (b) after 48 hr storage time.

### 5.9 Modified Wafer Bonding Without Final Thermal Annealing

This study was conducted in order to evaluate the bond quality of wafers that were bonded at slightly higher temperatures but without a final thermal annealing. Here, the bonding temperature was increased from 85 °C to 300 °C and the bonding time from 2 to 3 hr. The bonding recipe in the substrate bonder was changed in order to terminate the bonding process immediately following pre-bonding. The objective of this study was to analyze the effectiveness of plasma-activation on bonding wafers without a final annealing step. Following bonding, the wafer was diced and tensile tests were conducted on dies from the wafer-stack. Bond strength of 18 MPa was obtained. This was significantly less compared to the 24 MPa of bond strength of wafers that were pre-bonded and annealed. Therefore, it was concluded that a separate bonding and annealing step was required in the bond recipe in order to ensure a good bond quality and superior bond strength between the wafers.

### 5.10 Bond Integrity vs. Storage of Plasma-Activated and Bonded Wafers

In this study the wafers were stored after being bonded for extended time periods to evaluate the change in the bond quality with increase in shelf-life. The purpose of this study was to investigate the interfacial chemical changes of plasma-activated and bonded wafers. After RCA cleaning, the wafers were stored for 24 hr before being plasma-activated. Plasma-activation and wafer bonding were carried out using the conventional processes discussed in the Chapter 4. After bonding, NIR images of the wafer-stack were taken at different time intervals starting from time-zero. Figure 5.17 shows the NIR images at different time intervals of the plasma-activated and bonded wafer-stack. Time period was varied from 0-336 hr. Wafers was stored in ambient pressure and room temperature. As evident from the figure, certain improvement in the form of reduced void density was observed for wafers immediately analyzed after bonding and wafers analyzed after 336 hr of storage. This phenomenon was interesting to further investigate and, therefore, bonding and storing of wafers before dicing and tensile testing was carried out for bond strength measurements. Table 5.2 shows the results obtained from the tensile tests. The differences in bond strengths from consecutive shelf-times were calculated, as shown in Table 5.2. As evident from the table, the highest difference was observed for a shelf life of 120 hr. Although an increase in the bond strength was observed for an increase in shelf life, a point of saturation was observed after 144 hr. With the increase in shelf life, some interfacial chemical reactions take place in the form of oxidation of Si. The decrease in the density of voids was a result of the slow growth of the interfacial oxide layer.

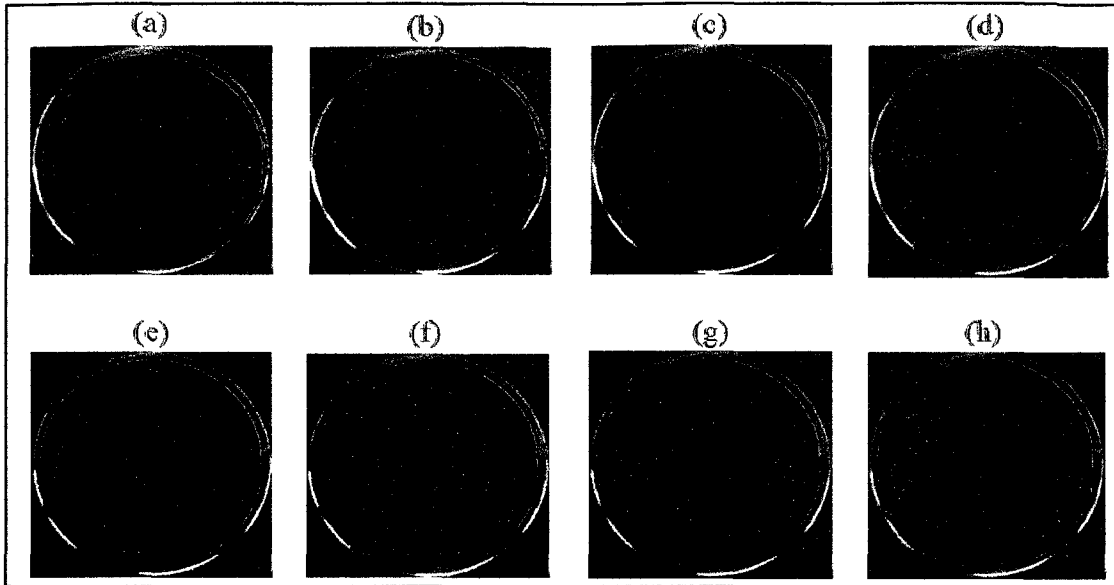


Figure 5.17. NIR images of wafer-stacks at (a) 0 hr (b) 24 hr (c) 48 hr (d) 120 hr (e) 144 hr (f) 168 hr (g) 312 hr (h) 336 hr after being plasma-activated and fusion bonded.

Table 5.2: Tensile test results obtained from 24 hr stored, plasma-activated, and bonded wafers with respect to different shelf lives.

Shelf-life	Bond strength		Difference
	(lbf)	(MPa)	
0	17.44	4.21	1.42
24	23.30	5.63	0.52
48	25.44	6.14	2.22
120	34.44	8.36	3.37
144	48.58	11.73	0.29
168	49.80	12.02	0.10
312	50.21	12.12	0.02
336	50.12	12.10	

### 5.11 Vacuum-Cavity Seal-Integrity Measurements

This section discusses the results obtained from the vacuum and seal integrity tests conducted on the encapsulated cavities within two Si wafers. The vacuum pressure in the cavity was measured using results obtained from the pressure diaphragm magnitude measurements. The deflection magnitude was compared to the finite element results obtained for the Si pressure diaphragm, and the corresponding loading pressure used for deflecting the diaphragm was considered to be the pressure inside the vacuum cavities. Measuring the volumetric change of the diaphragm-cavity enclosure over a long period of time helped to study the seal-integrity of the encapsulated cavities. Equation (5.7) for calculating the volume was derived from the volume formulae that corresponded to the fundamental geometric shapes, which made up the diaphragm-cavity enclosure. The breakdown of the diaphragm-cavity enclosure into basic geometrical shapes is illustrated in Figure 5.18. The cuboidal-shaped portion corresponds to the vacuum cavity etched into the Si substrate. The cavity resembled a cuboid. Similarly, the pressure diaphragm with zero deflection resembled a cylinder, and the deflection of the diaphragm was analogous to a spherical cap, as illustrated in the figure. The equation for the volume of the entire cavity-diaphragm enclosure was derived.

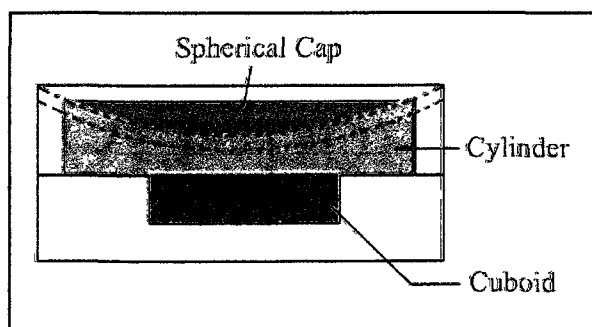


Figure 5.18. Illustration of the basic geometrical shapes that make up the diaphragm-cavity enclosure.

Consider a spherical cap as shown in Figure 5.19. Consider a segment plane parallel to the spherical segment as shown in the figure. Let  $r$  be the radius of the segment.

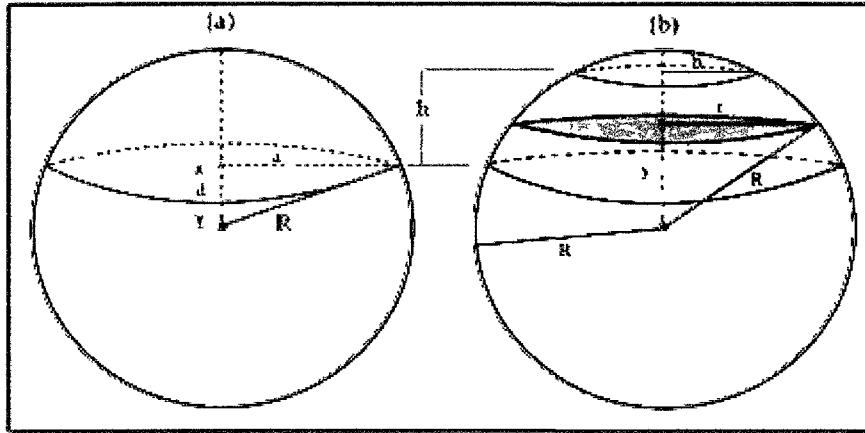


Figure 5.19. A drawing of (a) spherical cap (b) spherical cap with segment plane (in the middle) parallel to the spherical segments (top and bottom).

$$r^2 = R^2 - y^2 \quad (5.1)$$

Volume  $V$  of the spherical segment is given by the following set of equations.

$$V = \int_d^{d+h} \pi r^2 dy \quad (5.1 \text{ a})$$

$$V = \pi \int_d^{d+h} (R^2 - y^2) dy \quad (5.1 \text{ b})$$

$$V = \pi \left[ \int_d^{d+h} R^2 dy - \int_d^{d+h} y^2 dy \right] \quad (5.1 \text{ c})$$

$$V = \pi \left[ [R^2 y]_d^{d+h} - \left[ \frac{y^3}{3} \right]_d^{d+h} \right] \quad (5.1 \text{ d})$$

$$\therefore V = \pi \left[ R^2 - d^2 - dh - \frac{h^2}{3} \right] \quad (5.1 \text{ e})$$

$$a = \sqrt{R^2 - d^2} \quad (5.1 \text{ f})$$

$$b = \sqrt{R^2 - (d+h)^2} \quad (5.1 \text{ g})$$

$b$  is the radius of the upper segment in Figure 5.19 (b).

$$b^2 = R^2 - d^2 - h^2 - 2dh \quad (5.1 \text{ h})$$

$$d = \frac{a^2 - b^2 - h^2}{2h} \quad (5.1 \text{ i})$$

$$R^2 = a^2 + d^2 \quad (5.1 \text{ j})$$

Substituting Equation (5.1i) in Equation (5.1 j) and factorizing it we get Equation (5.2).

$$R = \frac{\sqrt{[(a-b)^2 + h^2][(a+b)^2 + h^2]}}{2h} \quad (5.2)$$

$$V = \pi h \left[ \frac{1}{2} (a^2 + b^2 + h^2) - \frac{1}{3} h^2 \right] \quad (5.3 \text{ a})$$

$$\therefore V = \frac{\pi h}{6} [3a^2 + 3b^2 + h^2] \quad (5.3 \text{ b})$$

For a spherical cap,  $b=0$ .

$$\therefore V_{cap} = \frac{\pi h}{6} (3a^2 + h^2) \quad (5.4)$$

Volume of a cuboid with length  $l$ , width  $w$ , and height  $h$  is given by Equation (5.5).

$$V_{cuboid} = lwh \quad (5.5)$$

Volume of a cylinder with radius  $r$  and height  $h$  is given by Equation (5.6).

$$V_{cylinder} = \pi r^2 h \quad (5.6)$$

Combining Equation (5.4), (5.5), (5.6), and renaming the variables, the equation for the total volume of the diaphragm-cavity enclosure  $V_{tot}$  is given by Equation (5.7).

$$V_{tot} = lwd + \pi r^2 h - \frac{\pi d_{cap}}{6} (3r^2 + d_{cap}^2) \quad (5.7)$$

$l, w, d$  are the length, width, and depth of the cavity in the Si substrate respectively,  $r$  is the radius of the pressure diaphragm,  $h$  is the difference in the thickness of the wafer and diaphragm, and  $d_{cap}$  is the deflection magnitude of the diaphragm.

### 5.12 Vacuum Cavities without Getter

The bonding mechanism carried out while sealing the cavities with the pressure diaphragms in vacuum was plasma-activated direct fusion bonding between Si-Si wafers. Immediately following bonding, the wafers were NIR inspected. No debonded regions were found. Prior to bonding, a photograph of the pressure diaphragm wafer was taken, and each diaphragm position and thickness was recorded. The deflection magnitudes of the diaphragms were measured and recorded against the corresponding diaphragm thicknesses. Differences in the barometric ambient air pressures, for the days the pressure diaphragm deflections were measured, were taken into consideration. Table 5.3 shows the results obtained. As evident from the table, the average pressure magnitude inside the vacuum cavities was found to be  $1 \times 10^{-3}$  mBar, which, according to literature sources, was reported to be an ideal vacuum pressure for packaging MEMS devices.

Table 5.3: Results obtained from the pressure diaphragm-vacuum cavity wafer stack with no interfacial getter.

<b>Diaphragm deflection</b>	<b>Diaphragm thickness</b>	<b>Equivalent FEA pressure</b>
<b>(<math>\mu\text{m}</math>)</b>	<b>(<math>\mu\text{m}</math>)</b>	<b>(<math>\mu\text{m}</math>)</b>
12.5	54	$1 \times 10^{-3}$
7.5	59	$1 \times 10^{-3}$
3.2	77	$1 \times 10^{-3}$
4.6	68	$1 \times 10^{-3}$
1.5	102	$1 \times 10^{-3}$

The deflection magnitudes of the diaphragms were measured over a one month period to monitor any changes in the magnitude of diaphragm deflection. Any leakage of

vacuum pressure in the cavities was observed as a change in the volume of the cavity. Figure 5.20 shows the results obtained from the investigations carried out on the change in the volume of the cavities over a one month period. As evident from the figure, the vacuum cavities failed to maintain constant vacuum pressure. The change in vacuum pressure was due to leakage of air into the cavity, thereby increasing the internal pressure of the cavities. This, in turn, led to the increase in the volume of the cavity.

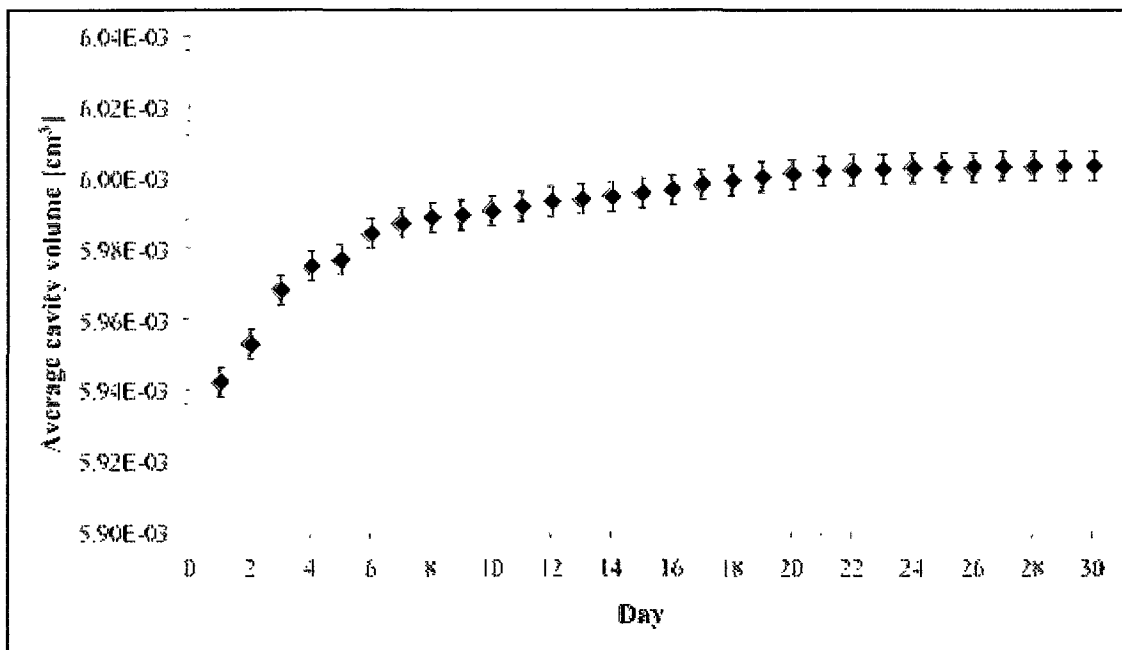


Figure 5.20. Plot showing the average change in the volume of vacuum cavities over one month period.

The plot in Figure 5.20 shows the average cavity volume that increased slightly over a one month period. A number of cavities were considered for calculating the internal vacuum pressure from measuring the pressure diaphragm deflection magnitude, and the average change in volume was calculated and recorded. The criterion for choosing the appropriate cavity-diaphragm enclosure was to choose diaphragms of approximately equal thicknesses (57  $\mu\text{m}$ ). The average initial deflection magnitude of the

diaphragm (right out of the bonder) was 10.26  $\mu\text{m}$ , with a cavity pressure of  $1 \times 10^{-3}$  mBar. This vacuum pressure was significantly reduced after a period of one month. Thus, it was necessary to employ a gettering agent inside the cavity in order to maintain the vacuum pressure at a constant level.

It was imperative to determine if the leak was real or virtual. Leakage of ambient air into the vacuum cavities was characterized as real leaks. The propagation of interfacial gaseous molecules into the vacuum cavities was characterized as virtual leaks. In order to characterize the type of leak present, first the wafer was placed in a vacuum chamber at  $1 \times 10^{-4}$  mBar for a period of 48 hr. If a change in the cavity volume was observed after 48 hr of the wafer being taken out of the vacuum chamber, then that would infer that the change in volume was caused due to a real leak. If not, the change in volume was caused due to a virtual leak. Changes in the cavity volume before and after placing the wafers in the vacuum chamber were recorded. This was repeated with several wafer-stack samples for the purpose of repeatability. Figure 5.21 shows the results obtained from this study. From the figure, it was evident that the volumes of the cavities at the edges of the wafer were lower than those in the central region. This was due to the fact that the diaphragms were thinner at the edges as compared to the center of the wafer, which was evident from Figure 5.21. Thinner diaphragms produced larger deflections, and thus the volume of the cavity-diaphragm enclosure was significantly lower. The x-axis shows the position of each cavity relative to the center of the wafer. The volume of the cavities, before the wafers were put into the vacuum chamber, was evidently larger than afterwards. The percentage difference between the volume of the cavity-diaphragm enclosure before and after re-exposure to vacuum was calculated to be 0.25%. This

inferred the presence of a real leak in the cavities, as the cavities were re-exposed to vacuum when the wafer was put back into the vacuum chamber. This was possible only if the air in the cavities could be pumped out, thus proving the existence of a real leak. The reason for the existence of a real leak in the packages was concluded to be due to the poor sealing of the packages using the plasma-activated fusion-bonding recipe. This signified the need for investigating the employment of an interfacial oxide layer as a sealant for the packages.

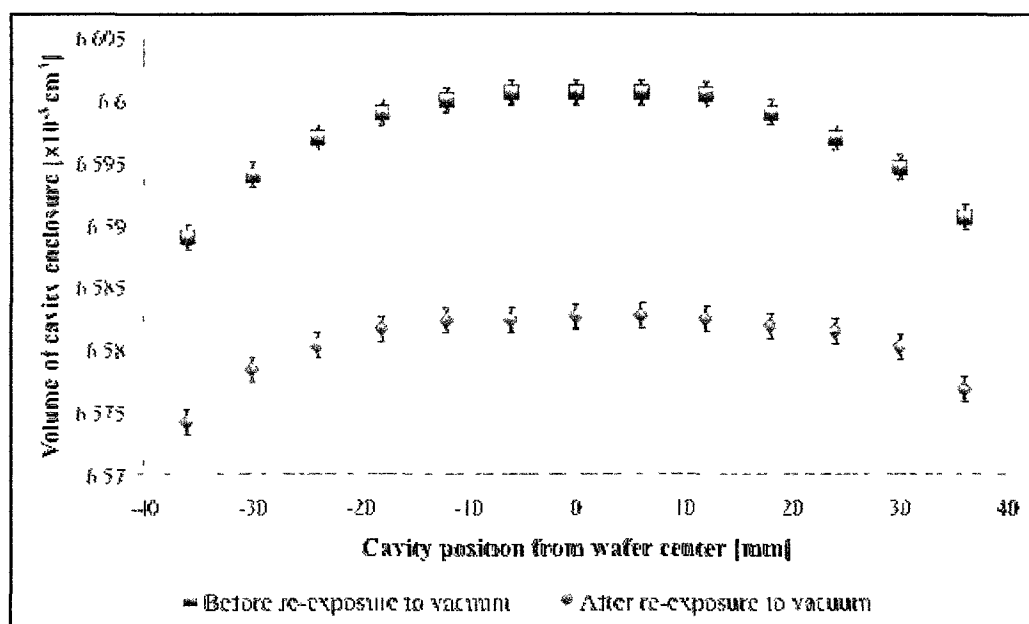


Figure 5.21. Plot showing the cavity enclosure volume, for cavities without any getter, across wafer before and after introducing wafer into vacuum chamber.

### 5.13 Vacuum Cavities with Getter Layer

The need for an interfacial or internal gettering agent was necessary in order to maintain or hermetically seal the vacuum cavities with the capping wafer. From previous studies, it was found that interfacial gaseous molecules were successfully gettered using an  $\text{SiO}_2$  layer. Superior bond quality was observed with wafers employing an interfacial

SiO<sub>2</sub> layer. This concept was applied to the vacuum cavity-pressure diaphragm wafer stack. An illustration of the oxide getter layer around the vacuum cavity is shown in Figure 5.22.

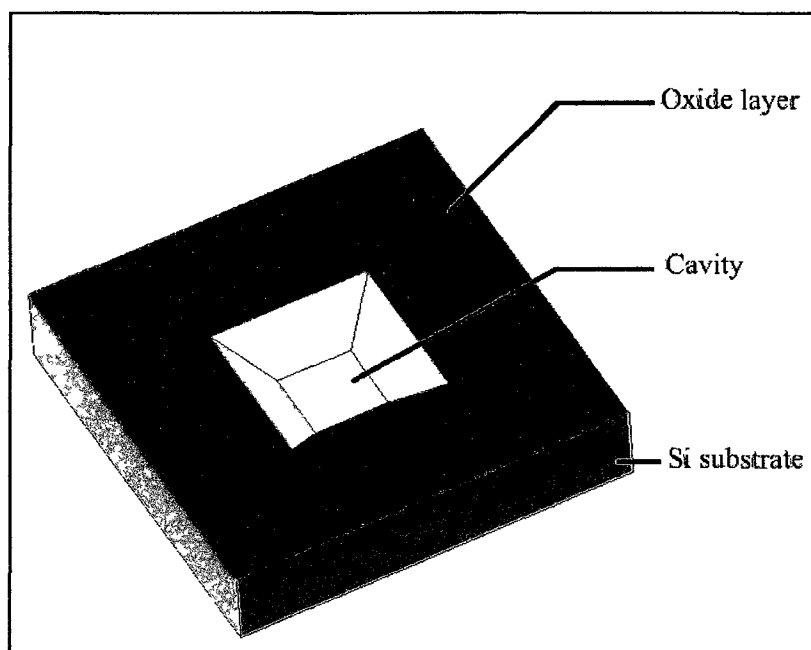


Figure 5.22. Illustration of oxide gettering layer around vacuum cavity.

The interfacial oxide gettering layer was achieved in the vacuum cavity-pressure diaphragm stack by retaining the thermal oxide layer (used as a hardmask for KOH etching), and wafer bonding the vacuum cavity and pressure diaphragm wafer substrates. As mentioned earlier, several cavity-diaphragm enclosures (across the wafer) were considered for volume measurements. The criterion for choosing the cavity-diaphragm enclosures was to choose diaphragms with approximately equal thicknesses (53  $\mu\text{m}$ ). Immediately following bonding, the vacuum pressure inside the vacuum cavities employing oxide getters was found to be  $1 \times 10^{-4}$  mBar. The average change in cavity volume was calculated from the measured diaphragm deflection magnitudes for a period of one month. Figure 5.23 shows the results obtained. As evident from the figure, no

significant change in cavity volume was observed. This inferred a superior seal integrity for the wafer stack with an interfacial oxide layer. The deflection magnitude of the diaphragms and the thickness of the corresponding diaphragms revealed an average cavity vacuum pressure of  $1 \times 10^{-4}$  mBar, which was significantly higher than the cavities without any oxide getter. It was imperative to investigate the presence of any real/virtual leaks. As mentioned in the previous section, the vacuum cavity-pressure diaphragm stack with oxide getter layers was placed inside a vacuum chamber at  $1 \times 10^{-4}$  mBar for a period of 48 hr. The change in cavity volume was investigated once the wafer was removed and left in ambient atmospheric pressure for 48 hr. Figure 5.24 shows the results obtained from this study. As evident from the figure, no significant change was observed from before and after re-exposing the wafer to vacuum. This revealed good seal integrity between the vacuum cavity and pressure diaphragm wafer with no real/virtual leaks in the vacuum cavities. This proved that an interfacial oxide layer resulted in a good seal/bond between a vacuum cavity and its capping wafer substrate.

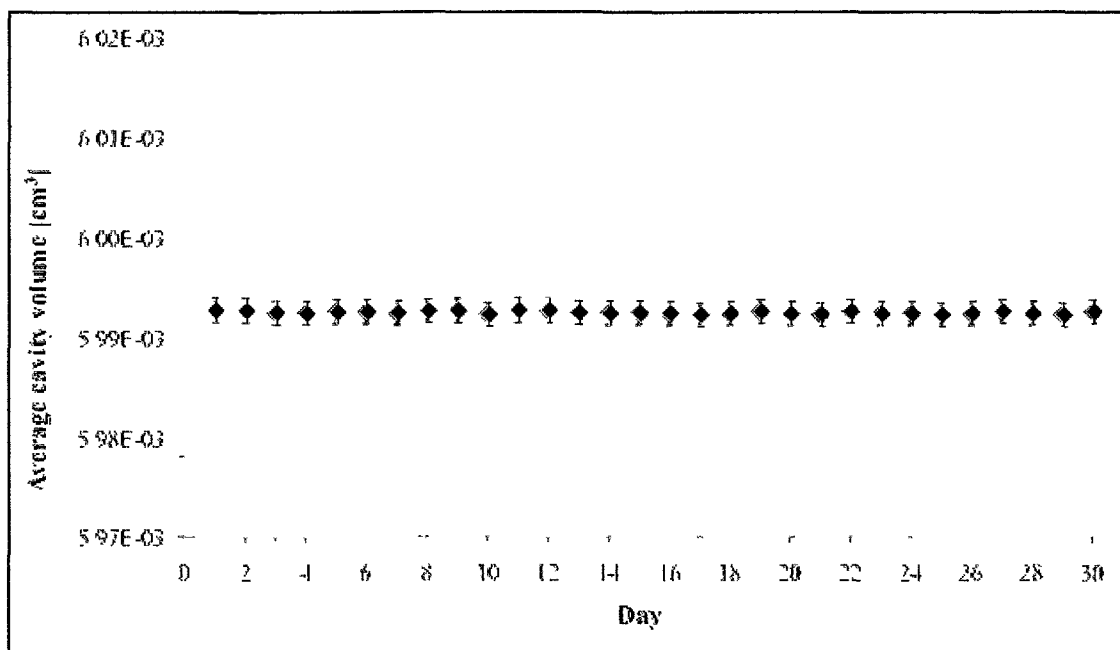


Figure 5.23. Plot showing the average change in the volume of the vacuum cavities with oxide getter over a one month period.

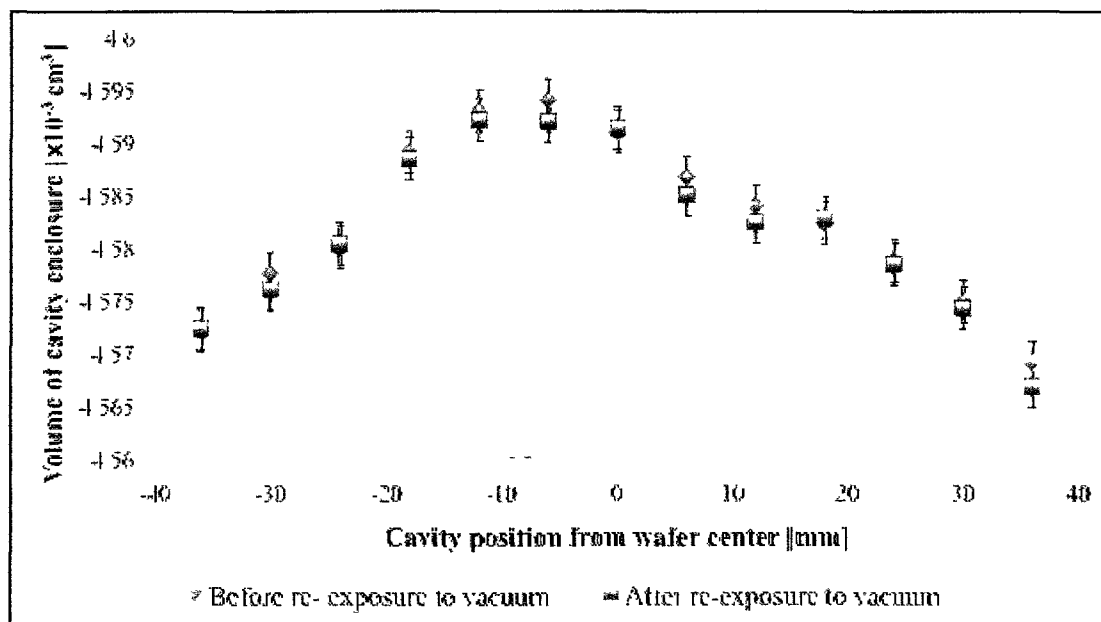


Figure 5.24. Plot showing the cavity enclosure volume, for cavities with oxide getter, across the wafer before and after introducing the wafer into the vacuum chamber.

### 5.14 Vacuum Cavities with Getter Rings

Since an interfacial oxide layer was found to be successful in gettering interfacial gaseous molecules, it was important to find out if an oxide strip would be able to maintain the internal cavity vacuum pressure for long time periods. This study was of particular importance for these instances where a gettering agent was necessary, and when the bond between the substrates needed to be purely between two Si substrates. In such a scenario, gettering ribbons/strips would have to maintain the vacuum pressure inside the cavities. Figure 5.25 shows a comparison of the pictures of the dark-field vacuum-cavity mask and the light-field oxide getter-ring mask. The square patterns on the getter-ring mask were slightly bigger than the square hole-patterns of the vacuum-cavity mask. When both these masks were used consecutively, an oxide ring was created around the vacuum cavities, as illustrated in Figure 5.26. Plasma-activation and wafer bonding of the getter-ring cavity wafer and the pressure-diaphragms wafer was carried out in the same manner as mentioned in the previous sections. Following bonding, the deflection magnitudes of the pressure diaphragms were measured, and the cavity volumes were calculated. As mentioned earlier, the criterion for choosing the right cavity-diaphragm enclosure was to choose the diaphragms with approximately equal thicknesses (54  $\mu\text{m}$ ). Cavity volume was monitored over a period of one month for any changes. The initial vacuum cavity pressure (immediately following bonding) was found to be  $5 \times 10^{-4}$  mBar. Figure 5.27 shows the results obtained from this study. As evident from the figure, only a very small change was observed in the cavity volume over a period of one month. Thus, it can be inferred that the oxide getter rings were able to maintain the vacuum level in the vacuum cavity for a long time period.

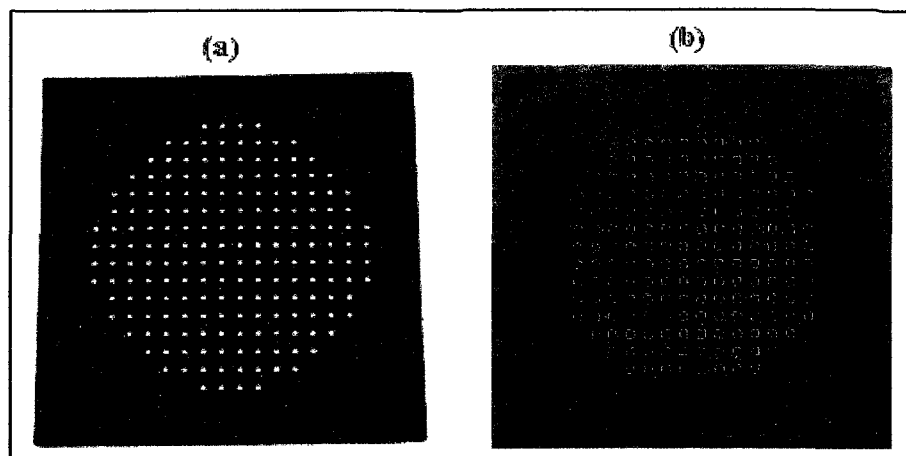


Figure 5.25. Comparison of the pictures of (a) Dark-field vacuum-cavity mask and (b) Light-field oxide getter-ring mask.

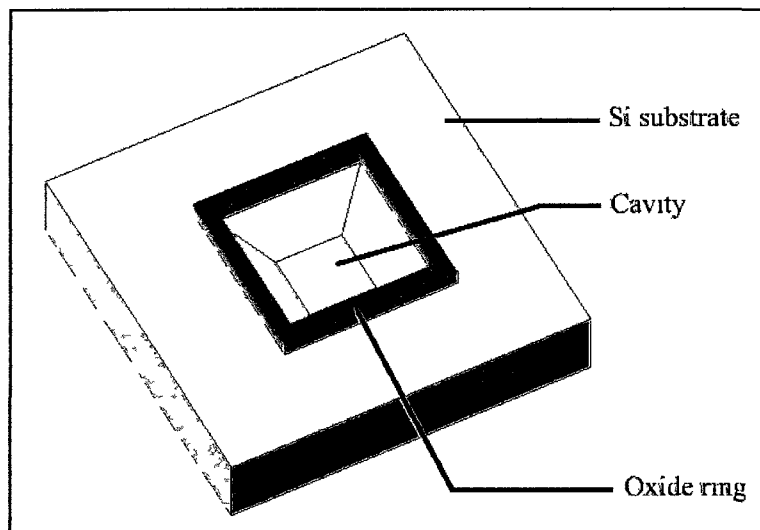


Figure 5.26. An illustration of the oxide getter rings around a vacuum cavity in a Si substrate.

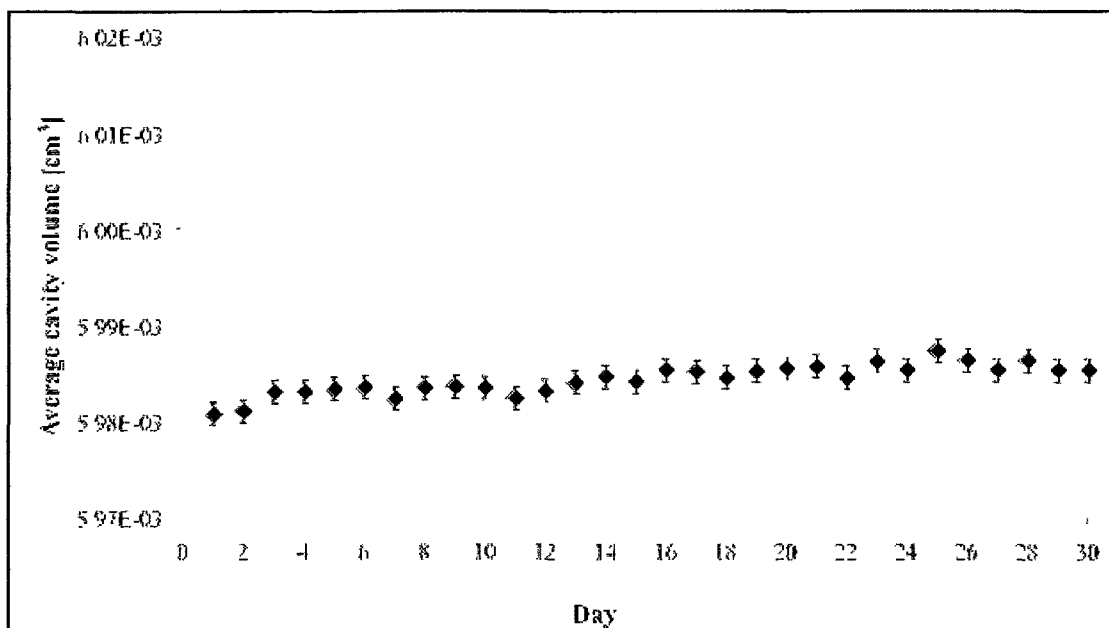


Figure 5.27. Plot showing the average change in the volume of vacuum cavities with oxide getter rings over a one month period.

Similar to the previous studies, the existence of real/virtual leaks in the system was investigated through repeated experimentation on several wafer-stacks. Measuring the deflection magnitude of the pressure diaphragm after 48 hr of bonding, carried out calculation of the change in cavity-diaphragm enclosure volume, and then placing the wafer-stack into a vacuum chamber at  $5 \times 10^{-4}$  mBar for 48 hr followed by another diaphragm deflection measurement. Figure 5.28 shows the results obtained from the real/virtual leak investigations. As evident from the figure, a small change in cavity volume was observed for cavities before and after being placed in the vacuum chamber. The percentage change in the volume of the cavity-diaphragm enclosure was calculated to be 0.09%. This revealed that there was a very small real-leak in the packages, but significantly lowers when compared to cavities without an oxide getter. The reason for this difference was attributed to the seal quality for interfaces without an initial virtual-

leakage. Immediately following the wafer bond, cavities without an oxide getter contained interfacial gas molecules that would have prevented a good seal between the surfaces in contact. In the case of cavities with getter rings, the oxide rings were able to absorb the interfacial gas molecules, which improved the seal integrity between the surfaces in contact. As a result, the seal integrity of packages with getter rings, even though not perfect when compared to packages with an entire oxide getter layer, was better than the seal integrity of packages without any oxide getters.

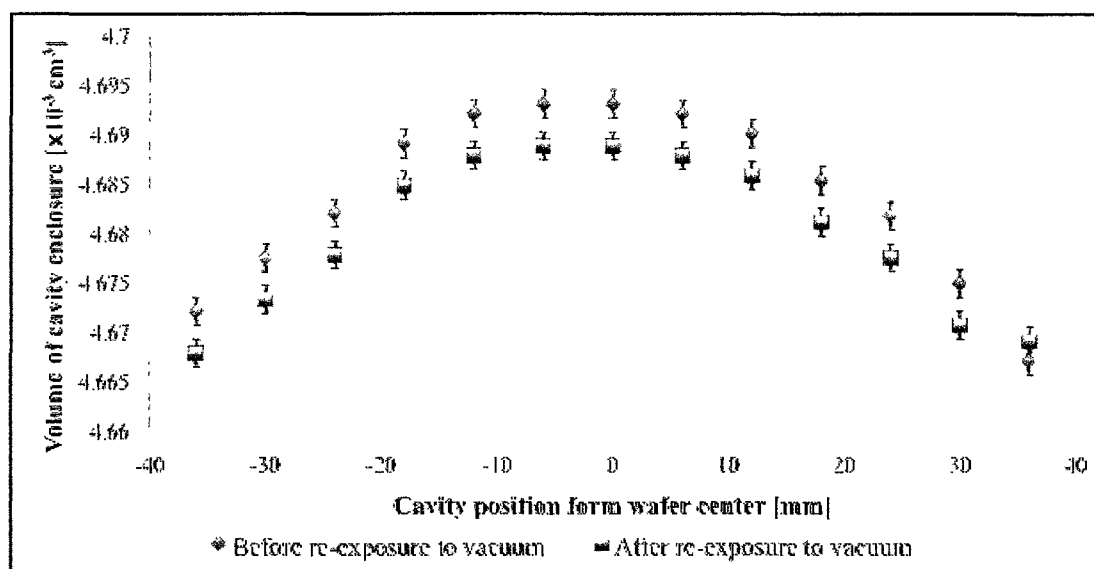


Figure 5.28. Plot showing the cavity enclosure volume of cavities, with oxide getter rings, across wafer before and after introducing wafer into vacuum chamber.

### 5.15 High Film-Stress in Released Beams

PZT cantilever beams were released through the  $\text{XeF}_2$  etching of the Si substrate. Figure 5.29 shows an SEM image of a released beam. As evident from the figure, curling of the composite beam was observed after releasing of the devices. Increased film-stress was traced back to the film deposition process. During the PZT film sol-gel deposition process, the PZT layers were not subjected to adequate annealing temperatures and times,

and hence the reason for the high stress in the crystal structure. The initial PZT deposition and annealing recipe was designed for beam widths less than 50  $\mu\text{m}$ , and beam thickness of 1  $\mu\text{m}$ . In this case, the beams were much wider (350  $\mu\text{m}$ ) and the beam thickness was 0.3  $\mu\text{m}$ . Therefore the effects of stress in the film were magnified with a less wide and thinner beam, as in the case of the beam shown in Figure 5.29.

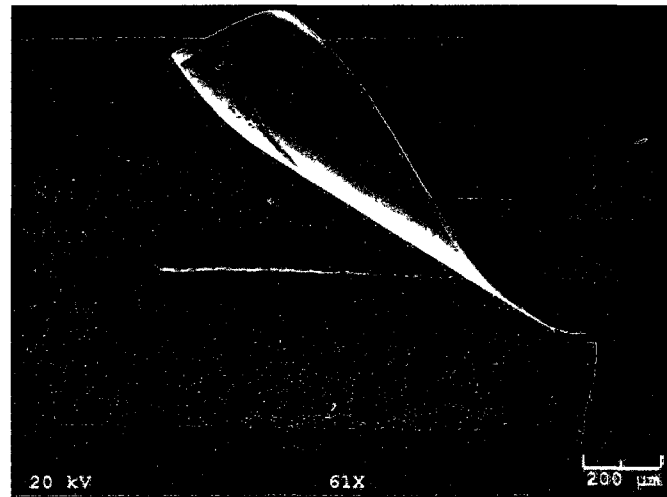


Figure 5.29. SEM micrograph of a curled PZT composite beam as a result of high film-stress.

### 5.16 Experimental Results of PZT Resonators in Vacuum and Air

In this study, PZT beam thicknesses were scaled up from 0.3  $\mu\text{m}$  to 1  $\mu\text{m}$  through additional layer depositions. In addition, additional thermal annealing at 600  $^{\circ}\text{C}$  for 8hr after the final PZT layer was laid down reduced the film-stress significantly in the final released PZT beams, as shown in Figure 5.30. The PZT beams were actuated at  $V_a = 50$  mV. The beams were swept for frequencies ranging from 1000-1150 Hz. Initial testing were carried out in ambient air. The maximum tip deflection obtained for corresponding resonant frequencies were recorded, plotted, and compared to theoretically obtained

results from the finite element modeling of the beam displacement, as shown in Figure 5.31. As evident from the figure, maximum beam deflection was observed at the resonant frequency of 1080 Hz with a maximum beam deflection magnitude of 2.9  $\mu\text{m}$ . This was slightly different from theoretical modeling results that showed a beam resonant frequency of 1082 Hz at an ambient air pressure of 1000 mBar. The reason for the slight discrepancy was attributed to additional damping factors, like material damping, electrical damping (due to resistances in electrical contacts), etc.

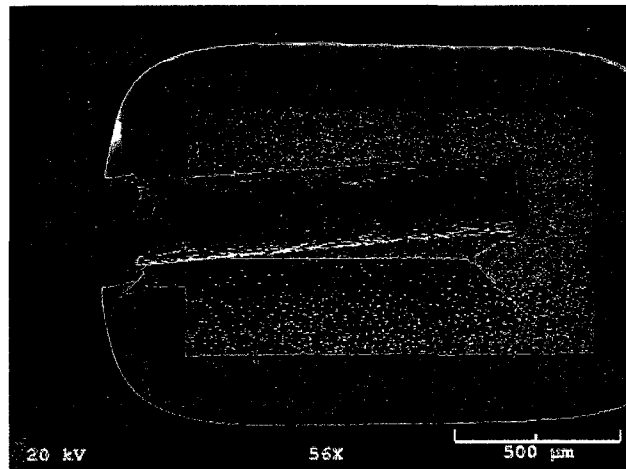


Figure 5.30. SEM micrograph showing the released PZT composite beam. No significant film stress was evident.

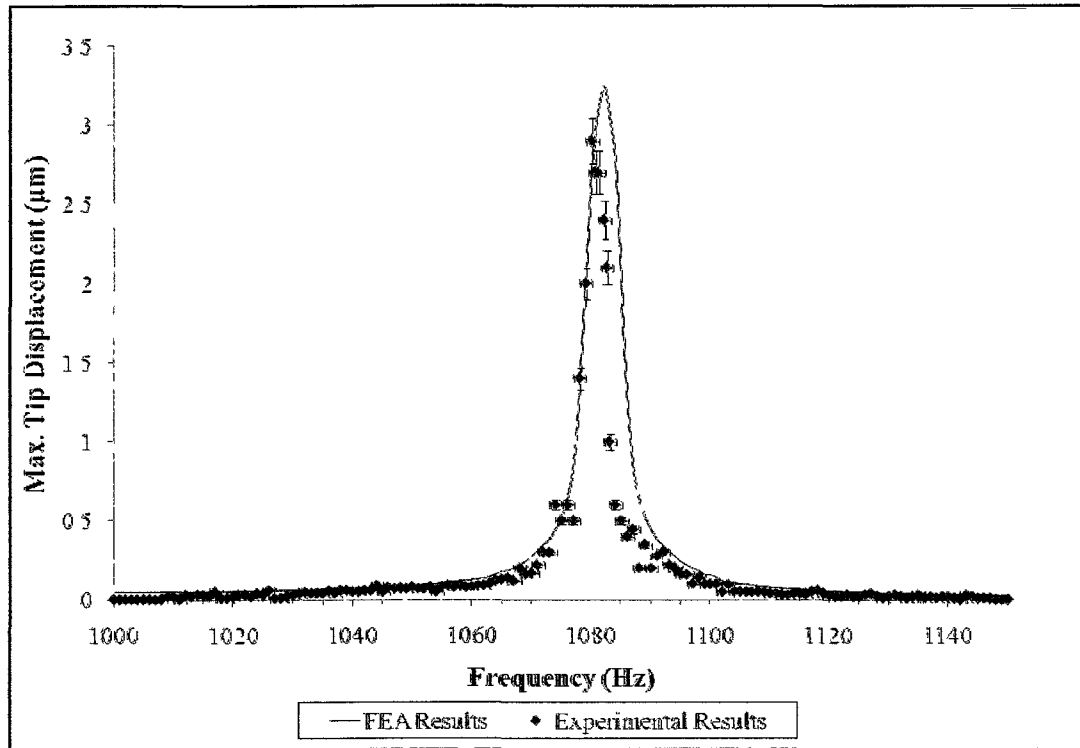


Figure 5.31. Comparison of the FEA and experimental results obtained for maximum tip deflection magnitude of the PZT beam at a resonant frequency of 1080 Hz.

Finally, the device was operated in a near vacuum environment by placing the device package in a vacuum chamber at a chamber pressure of 0.5 mBar. Figure 5.32 shows a comparison of theoretical and experimental results obtained for the beam actuated in different ambient air pressures. As evident from the figure, maximum tip-deflection was observed at near-vacuum pressure conditions due to the reduced air-damping in the system. Slight difference in the theoretically and experimentally obtained results was observed. This effect was attributed to additional damping losses of material damping, coupling losses, electrical damping, etc. that were assumed to be zero in the theoretical model. Additional discrepancies observed at 0.5 mBar vacuum pressure was attributed to the inaccurate laser spot placement on the beam tip (due to inaccurate sighting of the beam tip through the thick-walled glass lid of the vacuum chamber) and

the loss of beam intensity through refraction of the beam through the glass-air interface. Quality factor calculated for the beam at 3 dB of the deflection magnitude showed  $Q=42$  for a beam operating at 1000 mBar and  $Q=10^4$  for beam operating at 0.5 mBar. The results obtained emphasize the need for the vacuum-encapsulation of MEMS devices for the purpose of increasing the Q-factor as well as increasing the efficiency of the devices.

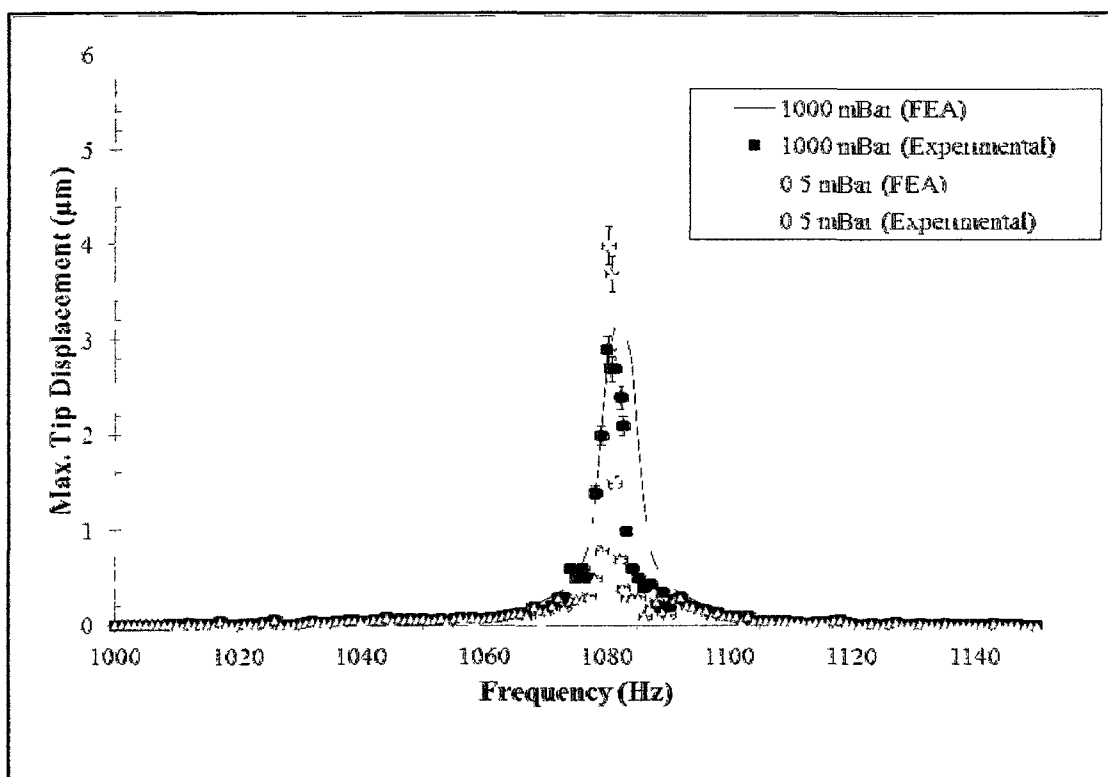


Figure 5.32. Plot showing a comparison of theoretical and experimental results obtained for an air-damped PZT beam at different ambient pressures.

## CHAPTER 6

### CONCLUSIONS AND FUTURE WORK

#### 6.1 Conclusions

Initially the mechanism of wafer fusion bonding was investigated and studied in detail. The problems of increased final annealing temperature were detailed and methods to significantly decrease the temperature were proposed. In addition to wet chemical wafer surface activation, dry surface activation techniques, like plasma-activation using  $O_2$  was investigated. An optimized plasma-activated wafer bonding recipe was designed. The bond integrity was qualitatively and quantitatively evaluated. NIR images of the plasma-activated and bonded wafer-stack showed no debonded regions at the interface. Tensile tests conducted on dies diced from the wafer-stack showed bond strength magnitudes of 22 MPa, which were close to the bulk-fracture strength of Si (24 MPa). Plasma-activated wafers were stored for varying time-intervals, before being bonded, in order to investigate the detrimental effects of storage time on the bond-quality. Interfacial chemical reactions taking place before, during, and after bonding were investigated by closely observing the interfacial layer. It was concluded that the thickness of the  $SiO_2$  layer increased with an increase in storage time. An interesting phenomenon of sudden increase in the bond-quality and bond-strength of plasma-activated wafers stored for more than 48 hr was observed. This increase in bond quality was concluded to be a result

of increased interfacial oxide layer thickness. Further investigations revealed that a thicker SiO<sub>2</sub> layer was capable of reabsorbing interfacial gas molecules like H<sub>2</sub>, which as a result decreased the density of the interfacial voids/debonded regions, thus increasing the bond-strength of the wafer-stack.

The possibility of fabricating vacuum-cavities between two Si substrates was explored. Etching cavities in a Si substrate wafer and sealing the cavities in vacuum using another Si capping wafer through plasma-activated wafer-fusion bonding carried this out. Vacuum seal-integrity was evaluated and found to be significantly low due to the evolution of interfacial gas molecules and their migration into the vacuum-cavities. In addition, the low seal-integrity resulted in the permeation of ambient air into the vacuum-cavities pressurizing them in the process. Possibilities of using the gettering capability of interfacial SiO<sub>2</sub> layer were investigated. Fabrication techniques to realize oxide getters at the interface of the wafer-stack were designed and carried out. Evaluation of the seal integrity and the maintaining of vacuum-pressure inside the cavities were investigated. Optical lid-deflection techniques employing high-aspect ratio circular pressure diaphragms were investigated. The pressure diaphragms were first finite-element modeled in order to study their characteristics with varying ambient pressure magnitudes. These diaphragms were coupled to the vacuum cavities in substrate Si by fabricating the pressure diaphragms onto the capping wafer and measuring the deflection magnitude of the diaphragm. The change in the deflection magnitude of the pressure diaphragms verified that there was a change in the internal cavity pressure, which indicated the presence of real/virtual leaks. Results showed that the interfacial SiO<sub>2</sub> layer was successful in preventing real/virtual leaks of the vacuum cavities.

Finally, PZT composite cantilever beams were fabricated on a Si substrate. Problems of high film-stress, as evident from curling of the beams, were investigated. Increasing the annealing temperature and time solved this. The cantilever beam was actuated in different ambient air pressures. Results were obtained for maximum tip-deflection for corresponding actuating voltage frequencies. Widening of the resonance-peak with an increase in air damping was obtained. The experimental results were compared to the finite element modeling results, and the reasons for the slight shift in the resonant frequency were explained.

## 6.2 Future Work

It would be interesting to integrate sensors, like pirani gage, spark-plug sensors, and resonators, in order to dynamically monitor the internal cavity pressure magnitudes. The fabricated PZT microcantilever characteristics in varying ambient pressure conditions were investigated by placing the package in a vacuum chamber. Future works could include the realization of vacuum-packaging these PZT beams using another capping Si wafer. However, running feed-through interconnects pose a fabrication challenge. Having diffusion layers as feed-through contacts for the purpose of actuating the vacuum-sealed beams could solve this. An illustration of the vacuum-sealed PZT device die with feed-through diffusion layer is shown in Figure 6.1. As illustrated in the figure, the proposed design would include metallic interconnects on the capping wafer with metal-filled through-holes for the purpose of electrically connecting the packaged bond pads of the sealed devices. This design would provide accurate seal-integrity study for vacuum-encapsulation of PZT microcantilevers using plasma-activated Si/Si fusion bonding.

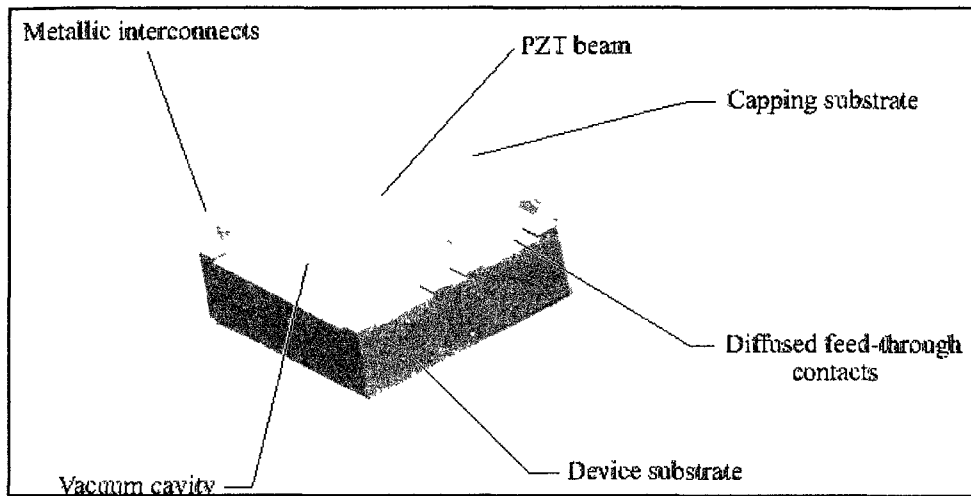


Figure 6.1. Illustration of vacuum-packaged PZT microcantilevers with buried feed-through interconnects and bond-pad interconnects.

## **APPENDIX A**

### **EQUIPMENT AND MATERIAL SPECIFICATIONS**

<b>Equipment/Material Name</b>	<b>Manufacturer</b>	<b>Model/Chemical Comp.</b>
Inductive Coupled Plasma	Alcatel	A 610E
Reactive Ion Etcher	PlasmaTherm	-
E-Beam Evaporator	CHA Industries	BEC-600-RAP
Thermal Evaporator	Denton Vacuum Inc.	DV-502A
Sputtering Station	AJA International, Inc.	ATC 2200-V
Spin Coater	Cost Effective Equipment	100
Mask Aligner	SussMicrotec	MA6/BA6
Wafer Substrate Bonder	SussMicrotec	SB6
Wafer Dicing Station	Micro Automation Inc.	M-1006
Ball Bonder	Marpet Enterprises Inc.	1024B
Epoxy Dispenser	EFD	2000XL
Scanning Electron Microscope	Hitachi	S4800
Surface Profilometer	Dektak	150
Surface Interferrometer	Veeco	NT102680
Ellipsometer	Sentech	SE850
Laser Vibrometer	Polytec	DFE – 650
Positive Photoresist	Sigma Aldrich	SPR220
Resist Developer	Rohm & Haas Elec. Mat. LLC	MF319
Epoxy	Emerson & Cuming	Tra-bond 2116 Kit
Ceramic Packages	Spectrum	CSB02482
Vulcan Box Furnace	DentsplyCeramco	3-550

## **APPENDIX B**

### **FABRICATION PROCESS RECIPES**

**B.1 HMDS & PT spin-coating**

Initial spin speed	=	500 rpm
Ramp rate	=	150 rpm/min
Initial time	=	5 s
Final spin speed	=	1000 rpm
Ramp rate	=	150 rpm/min
Final time	=	30 s

**B.2 PZT spin-coating**

Initial spin speed	=	500 rpm
Ramp rate	=	150 rpm/min
Initial time	=	5 s
Final spin speed	=	1200 rpm
Ramp rate	=	500 rpm/min
Final time	=	60 s

**B.3 SPR220 spin-coating**

Initial spin speed	=	500 rpm
Ramp rate	=	150 rpm/min
Initial time	=	5 s
Final spin speed	=	4000 rpm
Ramp rate	=	10000 rpm/min
Final time	=	90 s

#### B.4 ICP Bosch Process

Gas	Mode	Flow rate (sccm)	Priority	Time (s)
SF <sub>6</sub>	Pulsed	280	1	10
C <sub>4</sub> F <sub>8</sub>	Pulsed	40	2	3

#### B.5 RIE Dry Etch Process

Parameters	For Pt	For PZT	For SiO <sub>2</sub>
Chlorine gas flow rate (sccm)	20	7	-
Argon gas flow rate (sccm)	40	45	-
Helium gas flow rate (sccm)	-	-	50
CHF <sub>3</sub> gas flow rate (sccm)	-	-	12.5
CF <sub>4</sub> gas flow rate (sccm)	-	-	37.5
Chamber pressure (mBar)	6.67×10 <sup>-3</sup>	6.67×10 <sup>-3</sup>	0.33
Plasma power (W)	300	500	400

#### B.6 Pyrolysis recipe program for PT and PZT

Temperature 1	=	200 °C
Ramp rate	=	25 °C/min
Hold time	=	0 min
Temperature 2	=	450 °C
Ramp rate	=	2 °C/min
Hold time	=	30 min

Temperature 3 = 200 °C  
Ramp rate = 2 °C/min  
Hold time = 0 min

**END**

### **B.7 PZT final annealing recipe program**

Temperature 1 = 200 °C  
Ramp rate = 25 °C/min  
Hold time = 0 min  
Temperature 2 = 650°C  
Ramp rate = ~2 °C/min  
Hold time = 8 hr  
Temperature 3 = 200 °C  
Ramp rate = 2 °C/min  
Hold time = 0 min

**END**